PLANET FORMATION IN A DUSTY DISK: EFFECTS OF COLLISIONAL DUST GROWTH AND DYNAMICS

by

Debanjan Sengupta

A dissertation submitted to the Faculty of the University of Delaware in partial fulfillment of the requirements for the degree of Doctor of Philosophy in Physics

Winter 2019

PLANET FORMATION IN A DUSTY DISK: EFFECTS OF COLLISIONAL DUST GROWTH AND DYNAMICS

by

Debanjan Sengupta

Approved: _____

Edmund Nowak, Ph.D.
Chair of the Department of Physics & Astronomy

Approved: _____

John Pelesko, Ph.D.
Interim Dean of the College of Arts & Science

Approved: _____

Douglas J. Doren, Ph.D.
Interim Vice Provost for Graduate and Professional Education

I certify that I have read this dissertation and that in my opinion it meets the academic and professional standard required by the University as a dissertation for the degree of Doctor of Philosophy.

Signed: _____

James MacDonald, Ph.D.
Professor in charge of dissertation

I certify that I have read this dissertation and that in my opinion it meets the academic and professional standard required by the University as a dissertation for the degree of Doctor of Philosophy.

Signed: _____

Neal J. Turner, Ph.D.
Member of dissertation committee

I certify that I have read this dissertation and that in my opinion it meets the academic and professional standard required by the University as a dissertation for the degree of Doctor of Philosophy.

Signed: _____

John Gizis, Ph.D.
Member of dissertation committee

I certify that I have read this dissertation and that in my opinion it meets the academic and professional standard required by the University as a dissertation for the degree of Doctor of Philosophy.

Signed: _____

Stephen M. Barr, Ph.D.
Member of dissertation committee

ACKNOWLEDGEMENTS

I express my sincere gratitude to the citizens of the United States of America, whose hard-earned tax dollars made this research possible. I wish a meaningful, healthy and prosperous future to these exciting people of this highly spirited country.

I am grateful to my two amazing advisors, Dr. James MacDonald and Dr. Neal Turner, for their constant support, advising and teaching. Without them, I would not be writing this dissertation. They have been a constant source of inspiration for me, and their knowledge, professionalism, sincerity and dedication towards science have surely improved me both as a person and a scientist over the past years. I also thank my committee members for their time to go through this dissertation and the suggestions they provided which improved the quality of this research.

My sincere thanks go to Dr. Yasuhiro Hasegawa, Dr. Wladimir Lyra and Dr. Sarah Dodson-Robinson for their mentoring, and useful helps which made my learning more enjoyable and helped me improve the quality of this research significantly. Of them, I am specially grateful to my mentor and friend Yasuhiro for always being there whenever I needed him. His perfectionist attitude and higher expectations, although tough to cope with, have always kept me on my toes and have definitely made me work harder.

I also thank the Brew-HaHa coffee shop on the East Main Street, where most of this dissertation was written, and my special *Barista* friends Caitlin, Dave, Allison., Ryan, Molly, Amilie and Pierce for their unforgettable friendship and the excellent espresso shots they made for me with unbelievable perfection on a daily basis. Thank you all for being so nice! I also thank my fellow graduate students and friends from the department of Physics & Astronomy for all the stimulating discussions over the past few years and all the fun we have had.

I specially want to mention the gorgeous and amazing ladies of the 217 Sharp lab — Maura, Debra, Linda, Disney (Angie), Jissell and Elle, whose hard work and useful help at the right moments made my life easier as a graduate student. I do highly appreciate all the assistance they provided over the years.

Last but certainly not the least, I express my gratitude to my family, without whose unwavering support, care and benedictions, this journey would not have been possible. To my Dad, thank you for being an awesome and supportive father, and your tireless encouragement. Thanks to my mom for all the sacrifices she made for my education. A generous thank to my sister for always being very supportive and offering genuine guidance. Finally a very special thank to my wife for her constant support, love and care, without which this journey would not be so enjoyable.

The research presented in this dissertation was carried out in part at the Jet Propulsion Laboratory operated by the California Institute of Technology under contract with the National Aeronautics and Space Administration.

Dedicated to:

My Beloved Parents

&

My Lovely Wife

TABLE OF CONTENTS

LIST OF TABLES

LIST OF FIGURES

ABSTRACT

Despite making a small contribution to total protoplanetary disk mass, dust affects the disk temperature by controlling the absorption of starlight. As grains grow from their initial ISM-like size distribution, settling depletes the disks upper layers of dust and decreases the optical depth, cooling the interior. In this dissertation, we will discuss the effects of collisional growth of dust grains and their dynamics on the thermal and optical profiles of the disk, the vertical distribution of dust grains, and the possibility that cooling induced by grain growth and settling could lead to gravitational instability in an otherwise marginally stable disk. We also discuss how the critical gap-opening mass of a growing planet changes with the growth, settling and inward radial drift of solids in the course of a disk's evolution.

First, we present a new fast and numerically inexpensive Monte Carlo method with a weighting technique, which models collisional growth of dust, along with vertical settling, turbulent diffusion and radial drift. We present a comprehensive description of the structure of the massively parallel code we have developed. Next, as the first application of our dust model, we explore three disk models, the Minimum Mass Solar Nebula (MMSN), the Minimum-Mass Extra-solar Nebula (MMEN), and

a heavy disk with higher surface density than the MMEN, and perform simulations for both constant and spatially variable profiles of the turbulence efficiency, α. The variable profile is computed from the ionization fraction determined by an ionization-recombination chemical network. We then calculate wavelength-dependent opacities for the evolving disks and perform radiative transfer to calculate the temperature profile. We find that the growth of large particles in the mid-plane can make a massive disk optically thick at millimeter wavelengths, making it difficult to determine the surface density of dust available for planet formation in the inner disk. Finally, we calculate the Toomre Q parameter, a measure of the disk's stability to gravitational perturbations, for each disk model after it reaches a steady state dust-size distribution, and show that for an initially massive disk, grain growth and settling can reduce the Toomre Q parameter, making the disk unstable under its self-gravity and possibly triggering spiral instabilities.

In the second application, we apply our dust model to calculate the new hydrostatic equilibrium for vertical gas columns and show that the local gas scale heights become significantly less compared to the canonical value of $h(R)/R \sim 0.05$ for isothermal disk models, and can become as low as 0.005 in a disk with weak turbulence. We also find that the gap opening criteria is not sensitive to the mass of the disk, but basically depends on the turbulence strength. We discuss this result in the context of the minimum mass for a planet to open a gap in a settled

disk, and its possible implications for planet migration.

Chapter 1

INTRODUCTION

The field of planet formation has come to the forefront of astrophysical research since the first extrasolar planet 51 Pegasi b was discovered [Mayor and Queloz, 1995]. Following this discovery, the catalog of newly discovered planets has kept growing, thanks to several planet hunting missions, most notably, the recently decommissioned Kepler Space Telescope. The previously unknown new population of a few thousand planets in our galaxy revealed the unexpected distribution of planetary objects around their host stars and extended our outlook beyond the centuries old single sample, our own solar system. This overwhelming achievements in the observational aspects presented us with the obligations of explaining the existence and formation of these extra-solar planetary systems in a sound theoretical framework.

The process of planet formation starts with the formation of the star when a molecular cloud collapses due to its own self-gravity. Conservation of the large amount of angular momentum of the parent cloud dictates that, in most cases, the star is formed surrounded by a disk of dust and gas. These disks, also known as circumstellar or protoplanetary disks, are the birth places of the planets where the dusty components provide the necessary solid inventory for planet formation. So, it is very reasonable to assume that the observed diversity in the planetary architecture and compositions must be associated with their birth environment. To gain knowledge of how these disks evolve and how planets are formed in the course of their evolution, understanding the complex physical and chemical processes in the nascent planet forming disk is profoundly important.

As the building blocks of planetesimals and planetary size objects, solid dust grains are an important part of the planet forming disks. In the process of forming

the planets, (sub)-micron dust grains grow by several decades in mass. Although a consensus on the formation mechanism of km-size planetesimals is yet to emerge, the importance of the growth process upto few tens of cm is well appreciated and agreed by the community. As below 2000 K, dust is the major source of disk opacity, which depends on their evolving size distribution, disk opacity is basically set by the spatial and temporal abundance of solid grains. Moreover, dust grains controls disk chemistry and the abundance of volatile elements and water in the early proptoplanetary environment.

In order to understand the dust evolution, turbulence in the disk demands special care. The physics of growth and dynamics of solid bodies and disk turbulence are mutually interconnected. After the initial growth phase, where Brownian motion dictates the dust velocities and the tiny sub-micron dust grains grow upto a few tens of micron, turbulence in the disk gas starts playing the key role in setting the relative velocities of particle collisions. The effect of turbulence on the dynamics of the dust particles is generally quantified by a dimensionless Stokes number which determines the strength of coupling between the dust and the gas. Tightly coupled particles, with very low Stokes number, follow the gas motion and are the ones most susceptible to gas turbulence. Solid dust grains, on the other hand, provides an inverse feedback to the gas motion in two ways. First, the loosely coupled particles alters the gas dynamics by providing a drag force to the gas; second, the level of magnetohydrodynamic (MHD) turbulence is affected by the abundance of the charged species, which is controlled by dust. Dust particles provide the surface area for adsorption of charged species and thus assist the process of recombination. The very existence of the solid dust grains in the disk is the main source of the non-ideal MHD effects in disk turbulence. Moreover, several proposed hydrodynamic processes, such as vertical shear instability and photoelectric instability depends on the size, abundance and vertical distribution of dust particles.

Modeling grain growth, covering several decades in mass, in a global protoplanetary nebula, ranging over several tens of au, is a mammoth task. These simulations are

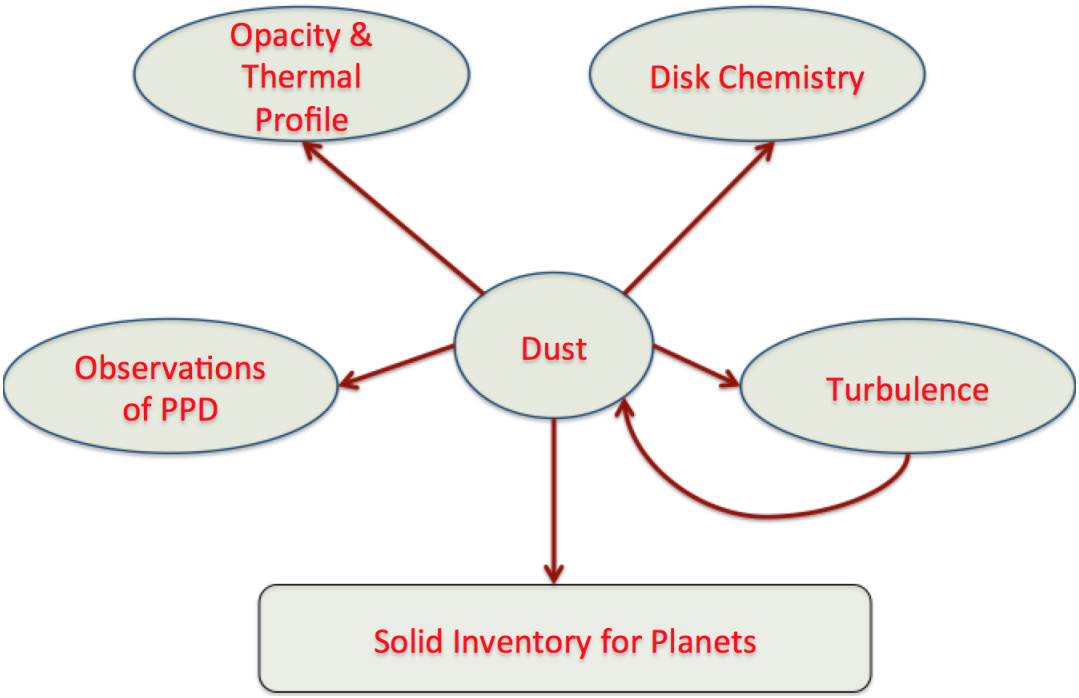

Figure 1.1: Solid dust grains are the major controller of the optical and radiative properties of the protoplanetary disks. They also controls the disk chemistry by assisting the recombination of charged species, which plays a key role in explaining the observed diversity of planetary compositions. The physics of dust growth and dynamics and disk turbulence are mutually interconnected and they influence each other. Turbulence affects the growth, whereas, the evolving size distribution of growing solids influences the MHD turbulence by setting the abundance of charged species. Most importantly, solid dust grains provide the solid inventory for planet formation.

generally performed following two different numerical techniques: (i) solving a partial differential equation (Smoluchowski's equation) by an implicit integration method or (ii) a Monte Carlo technique. Both of these modeling approaches have their merits and demerits. The implicit integration technique is numerically less expensive, although has the inherent problem of artificial diffusion in under-resolved simulations. It is also hard to include particle properties, such as charge, porosity, or different compositions without making the method prohibitively expensive. A Monte Carlo method, on the other hand, requires significantly more computer resources to simulate growth and dynamics. One inherent problem of any Monte Carlo method is that the simulation needs to follow each collision event in the course of evolution which puts a limit on the efficiency of the code. However, it is an ideal method to keep track of the individual particle properties.

The main expense of a Monte Carlo method comes from the N^2 nature of the model, where N is the number of Monte Carlo particles used in the simulation. To circumvent this problem, as the main part of this dissertation, we have developed a fast and efficient Monte Carlo method with a weighting technique which is essentially linear in nature. With the help of this method, we have developed a global numerical model for the growth and dynamics of solid dust grains in the disk. Our model implements the collisional physics with sticking and fragmentation. In order to track the dynamics of growing particles, the model also employs a Monte Carlo position-space Lagrangian technique to simulate vertical settling and turbulent stirring. The model, in its current state, implements the inward radial drift of dust as well.

Our model also computes the monochromatic opacities of the evolving dust grains and we perform dust continuum radiative transfer calculations in order to compute the thermal profile of the disks. We assume local thermodynamics equilibrium (LTE) in which the local gas and dust temperatures are equal.

1.1 Structure of this Dissertation

This primary objective of this dissertation is to develop a fast and efficient numerical model for the growth and dynamics of solid dust grains in protoplanetary nebulae, starting at an early phase, and apply it in order to understand the role of dust in some key physical disk processes. In order to present our work in a comprehensive way, we structure this dissertation as below:

Chapter 2

In this chapter we present a general overview of the theory of evolution of dust and gas in protoplanetary nebulae. We first review accretion disk theory, followed by the theory for dust growth and dynamics. We primarily focus on the theoretical aspects of the literature which are particularly important in the context of our model building and explaining the results in the later chapters.

Chapter 3

In this chapter, we first present the algorithm of our Monte Carlo dust model followed by a description of the Monte Carlo position-space Lagrangian method which implements the vertical dynamics of dust grains. The chapter also elaborates the method we employ in order to calculate monochromatic opacities of evolving dust grains following the 'utilitarian opacity model' of Cuzzi et al. [2014]. We then describe the working principles of the publicly available code RADMC and the way we have used it in our model. The implementation of the model in a computer code is also presented in detail with special focus on our parallelization algorithm.

Finally, we test our code extensively against results from existing literature where other methods have been used to simulate dust physics. We also test our code against analytical results in order to confirm its fidelity and usability.

Chapter 4

In chapter 4, we present our first application of our dust model. We present a total of 11 global simulations adopting three different disk models with a $-3/2$ power-law surface density profile: Minimum Mass Solar Nebula (MMSN), Minimum Mass Extrasolar Nebula (MMEN) and a 'heavy' disk model. We calculate the monochromatic

opacities and spectral opacities of the evolving grain size distribution as a function of radial distance and vertical height. We also present the changes in optical depth at the disk midplane and discuss the possible implications for disk observations and measurement of disk masses.

Finally, we investigate how Toomre-Q, a parameter which measures the disk's stability against self-gravity, changes with grain growth and settling. We report that in all the simulations performed, Q suffers a small but noticeable reduction which can potentially make an initially marginally stable disk unstable to gravitational perturbations.

Chapter 5

In this chapter, we present a second application of our dust model and include radial drift of dust particles as well. We present an investigation of how grain growth and settling can reduce the gap-opening mass of a growing planetary candidate. To conduct our research, we use four different disk models with a similar power-law to chapter 4 and adopt four different values for turbulence strength for each disk. The main idea follows from the fact that dust settling alters the hydrostatic equilibrium of a particular vertical column leading to a reduced pressure scale height (h_g) and a thinner gas disk. A planet with a Hill radius greater than the local scale height starts to open a gap in the disk, dividing the disk into an inner and outer part. A reduction in h_g would allow a smaller planet to open a gap. We investigate this aspect of the post-formation planetary evolution and find that the disk scale height can get reduced almost by an order of magnitude due to dust growth and settling in a disk with weak turbulence. We also find this effect insensitive to the mass of the disk. We discuss our findings in the context of the observed exoplanet populations.

Chapter 6

We finish this dissertation with concluding remarks in chapter 6. We discuss the possible avenues in which our model and code can be further extended in order to make it more realistic.

Chapter 2

DUST AND GAS IN PROTOPLANETARY DISK: A GENERAL OVERVIEW

2.1 Introduction

The process of planet formation starts with the gravitational collapse of a molecular cloud, leading to a young star, surrounded by a disk of dust and gas. The disk around the new-born star is the result of the conservation of angular momentum of the parent cloud. Although the star contains $\sim 99\%$ of the total mass of the newly formed star-disk system, the disk has almost all of the angular momentum. Taking our own solar system as an example, the orbital angular momentum of Jupiter alone is $\sim 10^2$ times higher than that of the solar rotation despite being about 300 times less massive than the sun. The molecular cloud itself, due to its large length scales, is a reservoir of a large amount of angular momentum. For example, let's consider a molecular cloud with mass $M_c \sim 1.5 M_\odot$ and 0.1 pc wide (1 pc $\sim$ 3.26 light years) with a typical angular momentum per unit mass 10^{21} cm^2 s^{-1}. The total angular momentum of the cloud can thus be estimated as $L_{MC} \sim 10^{54}$ g cm^2 s^{-1}. If the collapse of this cloud forms a 1 $M_\odot$ star with a disk, and L_{MC} is fully conserved and contained in the star-disk system, the angular momentum contained in the disk (L_{disk})

$$L_{disk} = \int_0^{R_0} dm R^2 \Omega(R), \tag{2.1}$$

gives R_0, the extent of the disk, as $\sim 10^4$ au. Star formation through cloud collapse, however, is a complex process, where a single collapse event generally forms multiple stars, and a substantial fraction of angular momentum is carried away by jets and winds. Also, magnetic fields with their ideal and non-ideal effects play an important

role in setting the collapse timescales which agrees well with the timescales calculated theoretically. If, in the above example, the disk accounts for only 30% of the total angular momentum of the parent cloud, the resulting R_0 can be calculated as $\sim 10^2$ au, which agrees reasonably well with the observations of protoplanetary disks. Thus, it can be safely asserted that, the formation of the disk is a robust process parallel to the formation of stars in most cases.

2.2 The Gaseous Disk

In this section, we describe the basic physics related to the gaseous accretion disk and its evolution through angular momentum transport. We discuss the radial and vertical structure of the gas along with its radial temperature profile. We shall also present a discussion of the diffusive timescale of the disk and the need for turbulence to match the observed disk lifetimes.

2.2.1 Radial Structure

A typical gaseous protoplanetary disk can extend upto several hundreds of au in the radial direction. If we consider the disk to be made up of a series of thin gaseous circular strips, each annulus at a particular radial distance would rotate with different orbital speeds and hence with different frequencies. Consider a parcel of gas of mass m at a distance R from the star of mass $M_\star$. The balance between the force of stellar gravity and centrifugal force gives

$$m\Omega^2 R = \frac{GM_\star m}{R^2}. \tag{2.2}$$

Here Ω is the local orbital frequency, also known as Keplerian frequency, which, from equation 2.2, is

$$\Omega = \sqrt{\frac{GM_\star}{R^3}}. \tag{2.3}$$

The velocity with which the fluid parcel rotates, also identified as the azimuthal velocity, can thus be written as $v_\phi = R\Omega = \sqrt{GM_\star/R}$. This variation of orbital velocity

with distance results in a differentially rotating disk. Also, the specific angular momentum of the fluid parcel cal be written as $l = R^2\Omega = \sqrt{GM_\star R}$. If we consider two adjacent rings of gas, the outer ring, moving slower than the inner one, would interact with the inner ring through friction or viscosity. This would accelerate the outer ring while the inner ring will be decelerated. Through this mechanism, the fluid parcels lose angular momentum and spiral into the star, while a small amount of matter moves radially outward carrying the angular momentum in order to conserve it. This is the classic picture of what is generally known as accretion disk theory. In later parts of this dissertation we shall discuss the theory of accretion and angular momentum transport in more detail.

In general, a protoplanetary disk is modeled in 1, 2, or 3 dimensions using cylindrical or spherical coordinate systems. However, it is both analytically and numerically convenient to model the disk in 1-D where the basic equations are written in terms of vertically integrated quantities. The gas surface density Σ_g is obtained by vertically integrating the gas density ρ_g as

$$\Sigma_g(R) = \int_0^\infty \rho_g(R, z)\, dz \tag{2.4}$$

The true variation of Σ_g as a function of radial distance is still a matter of active debate. However, one of the most common forms that is adopted for theoretical and numerical modeling is a power law profile

$$\Sigma_g(R) = \Sigma_0 \left(\frac{R}{1 \text{ au}}\right)^{-p}. \tag{2.5}$$

where, Σ_0 is the surface density at 1 au and p is the surface density power-law index. The most widely used power law form of surface density, following the planetary mass distribution of the solar system, is the so-called Minimum Mass Solar Nebula (MMSN) model [Hayashi, 1981] where $\Sigma_0 = 1700$ g cm^{-2} and $p = 3/2$. However,

several research predict that the MMSN model underestimates the disk mass by significant factors. From the population of extra-solar planets, assuming their *in situ* formation, a more massive model with similar power-law index is predicted by Chiang and Laughlin [2013], known as Minimum Mass Extra-solar Nebula (MMEN), for which Σ_0 is taken as 9900 g cm^{-2}. However, Raymond and Cossou [2014] has shown that, for planetary systems with 3 - 6 planets (or planetary candidates), p lies between -3.2 and 0.5. With the current population of confirmed exoplanets, and with an in situ formation approximation, the median power-law index comes around 1.7. However, it is important to note that our current ability of exoplanet detection is biased towards relatively massive planets in close-in orbits, which would definitely result into a steeper power law profile. Moreover, the addition of planet migration in the post formation phases would end up with a heavier inner disk compared to the initial stages.

Another widely used disk surface density profile comes from the similarity solution for a viscous accretion disk, described by Lynden-Bell and Pringle [1974] and further generalized by Hartmann et al. [1998]. This surface density adopts a shallower power law profile along with an exponential term:

$$\Sigma(R) = \frac{M_{disk}}{\pi R_0^2}\left(\frac{2-p}{2}\right)\left(\frac{R}{R_0}\right)^{-p} e^{-(R/R_0)^{2-p}} \tag{2.6}$$

Here M_{disk} is the disk mass and R_0 is an arbitrarily chosen radius for normalization. To characterize the plausible radial variations of the nebula the power-law is chosen such that $p \in [0, 3/2]$ [Cuzzi et al., 2003, Estrada et al., 2016]. Hartmann et al. [1998] chose $M_{disk} = 0.2M_\odot$ and $p = 1$ with $R_0 = 10$ au. Often the scale parameter R_0 is also chosen according to other criteria. For example, Cuzzi et al. [2003] chose $R_0 = 4.5$ au to match the specific angular momentum of solar nebula. In general, the nominal values adopted by several authors lie between 20 - 60 au [Ciesla and Cuzzi, 2006, Garaud, 2007, Brauer et al., 2008, Hughes and Armitage, 2012, Yang and Ciesla, 2012]. As the values adopted for the parameters above varies widely, a consensus on this issue is yet to emerge. It is important to note that, equations 2.5 and 2.6 provide only favorable

initial conditions for $\Sigma_g(R)$ which does not remain the same owing to its complex temporal evolution.

2.2.2 Radial Evolution

The most important aspect of any accretion disk is the radial evolution of the gas through the transport of angular momentum. According to the accretion disk theory developed by Lynden-Bell and Pringle [1974] and Pringle [1981], based on the conservation of mass and momentum of disk gas, the equation governing the evolution of surface density is

$$\frac{\partial \Sigma_g}{\partial t} = \frac{3}{R}\frac{\partial}{\partial R}\left[R^{1/2}\frac{\partial}{\partial R}\left(\nu \Sigma_g R^{1/2}\right)\right]. \tag{2.7}$$

Here, ν is the kinematic viscosity. Equation 2.7 is a diffusion equation for Σ_g and is linear if ν is independent of Σ_g. Also, the radial velocity of a fluid element in the disk undergoing accretion can be written as

$$v_g = -\frac{3}{R^{1/2}\Sigma_g}\frac{\partial}{\partial R}\left(R^{1/2}\nu\Sigma_g\right) \tag{2.8}$$

The corresponding mass accretion rate of the disk is $\dot{M} = -2\pi R \Sigma_g v_g$, where a positive value of $\dot{M}$ indicates accretion onto the central star. (See Appendix A for a detailed derivation of equations 2.7 and 2.8 from the Navier-Stokes equation.)

Analytic solution of equation 2.7 is possible if the viscosity ν can be expressed as a power-law in radial distance. However, by assuming a constant viscosity, it is possible to understand the basic essence of the accretion process by seeking a Green's function solution. Setting ν =constant, lets assume that we start with a system where all the disk mass M_d is contained in a thin ring at a distance R_0 from the central star. In this case the, the initial surface density can be written as

$$\Sigma(R, t=0) = \frac{M_d}{2\pi R_0}\delta(R - R_0) \tag{2.9}$$

where we have used a δ-function to denote the concentration of the total mass as $R = R_0$. The solution to equation 2.9 is (Following Armitage [2011])

$$\Sigma(x,\tau) = \frac{M_d}{\pi R_0^2}\frac{1}{\tau}x^{-1/4}e^{-(1+x^2)/\tau}I_{1/4}\left(\frac{2x}{\tau}\right). \tag{2.10}$$

Here two dimensionless variables have been used; $x = R/R_0$ and $\tau = 12\nu t/R_0^2$. $I_{1/4}$ is a modified Bessel's function of the first kind. As $t \to \infty$, the mass of the ring flows towards $R = 0$ and a small amount of mass carries away all the angular momentum to $R \to \infty$. This separation of mass from the angular momentum is the basic feature of the viscous evolution of the accretion disk.

2.2.3 Viscous Time Scale: Need for Turbulence

Starting from equation 2.7, a variable transformation $\tilde{R} = 2R^{1/2}$ and $\tilde{\Sigma}_g = (3/2)\Sigma_g\tilde{R}$ along with the assumption that ν is constant, the 1-D diffusion equation can be expressed in the form of a canonical diffusion equation,

$$\frac{\partial\tilde{\Sigma}_g}{\partial t} = K\frac{\partial^2\tilde{\Sigma}_g}{\partial\tilde{R}^2} \tag{2.11}$$

where K is the diffusion coefficient and can be written as $K = 12\nu/\tilde{R}^2$. From equation 2.11, the diffusion time scale accross a scale $\Delta\tilde{R}$ can be estimated as $\tau_\nu \sim (\Delta\tilde{R})^2/K$. Transforming back to the original variables, we get

$$\tau_\nu \sim \frac{(\Delta R)^2}{\nu}. \tag{2.12}$$

Assuming a typical value for molecular viscosity $\nu = 0.01$ cm^2 s^{-1}, the viscous timescale becomes $\sim 10^{13}$ years, which is larger than the age of the universe. The observed disk lifetime, on the other hand, is $\sim$ 3 Myr, clearly points towards some other source of viscosity. It is widely believed that the viscosity ν in equation 2.12 originates from turbulence in the disk, both hydrodynamic and magneto-hydrodynamic in nature. The typical range of values for ν in equation 2.12 required to match the viscous time scale

with the disk lifetime is $\sim 10^{10} - 10^{14}$. These large values are plausible if and only if viscosity is originated from the collisions of eddies of different length scales resulting from turbulence. This type of phenomenological viscosity is also sometimes referred to as "eddy viscosity".

In the context of viscous evolution, disks are generally modeled by the famous α prescription put forward by Shakura and Sunyaev [1973]. The viscosity in an α-disk is computed from a phenomenological turbulence model and is written as

$$\nu = \alpha c_s h_g \tag{2.13}$$

where α is a constant denoting the turbulence efficiency. This prescription assumes the local gas scale height h_g as a characteristic length scale and the local thermal speed c_s as a characteristic velocity with the sound propagation time as the characteristic time scale. In that context, α denotes the efficiency with which the free energy from the background shear is injecte into the system and cascades down to the Kolmogorov scale through the inertial range. Typical values of α lies between 10^{-6} to 10^{-1} depending on the physical mechanism responsible for the turbulence in the disk.

Apart from the radial viscous evolution, the turbulence also affects the radial and vertical mixing of dust particles. For Kolmogorov type turbulence approximation in the disk, the assumed homogeneity produces a turbulence profile essentially the same in all aspects. However, the presence of the magnetic field would would introduce an inhomogeneity in the system. This will generate eddies which are elongated in the direction perpendicular to the mean magnetic fields, producing different turbulence strengths in the radial and vertical directions. Moreover, the shear inherent to the differentially rotating disk would also introduce a shear driven anisotropy in the system. As a result, in the most realistic scenario the turbulence, responsible for angular momentum transport and radial or vertical mixing can differ by a few order of magnitudes.

2.2.4 Restating the Mass Conservation for the Disk

The general mass conservation in fluid dynamics reads as

$$\frac{\partial \rho}{\partial t} + \nabla \cdot (\rho v) = 0 \tag{2.14}$$

where, v is the fluid velocity. We now assume azimuthal symmetry for simplification and express equation 2.14 in terms of disk surface density Σ and restate the mass conservation in the context of an accretion disk. As we have seen before, Σ can be expressed as

$$\Sigma = \frac{1}{2\pi} \int_0^{2\pi} \int_{-\infty}^{+\infty} \rho \, dz \, d\phi \tag{2.15}$$

where ρ is the gas density. Due to the disk geometry, it is convenient to work on a cylindrical co-ordinate system, in which, equation 2.14 reads

$$\frac{\partial \rho}{\partial t} + \frac{1}{r}\frac{\partial}{\partial r}(r \rho v_r) + \frac{1}{r}\frac{\partial}{\partial \phi}(\rho v_\phi) + \frac{\partial}{\partial z}(\rho v_z) = 0. \tag{2.16}$$

Here, v_r, v_ϕ and v_z are the r, ϕ and z components of the gas velocity. Now we make an assumption that there is no mass loss in the vertical direction to $z = \pm\infty$. With this, integrating equation 2.16, we get

$$2\pi \frac{\partial \Sigma}{\partial t} + \frac{1}{r}\frac{\partial}{\partial r}\mathcal{F} \tag{2.17}$$

where

$$\mathcal{F} = \int_{\phi=0}^{2\pi} \int_{-\infty}^{+\infty} r \rho v_r \, d\phi \, dz \tag{2.18}$$

$$= 2\pi r \int_{-\infty}^{+\infty} \rho v_r \, dz \tag{2.19}$$

is the radial mass flux. At this point, we define a density weighted mean radial velocity $\bar{v_r}$ as

$$\bar{v_r} = \frac{1}{\Sigma} \int_{-\infty}^{+\infty} \rho v_r \, dz. \tag{2.20}$$

With this the radial mass flux $\mathcal{F}$ becomes $\mathcal{F} = 2\pi r\Sigma v_r$ and the continuity equation reads

$$\frac{\partial \Sigma}{\partial t} + \frac{1}{r}\frac{\partial}{\partial r}\left(r\Sigma \bar{v_r}\right) = 0. \tag{2.21}$$

2.2.5 Angular Momentum Conservation

In this section we discuss the conservation of the angular momentum in an accretion disk. We also state the necessity of the shearing stress and its role in driving accretion. The dynamical equation of a fluid flow, also known as the momentum conservation equation or more famously, the Navier-Stokes equation, can be stated as

$$\rho\frac{\partial \rho}{\partial t} + \rho\left(v\cdot\nabla\right)v = -\rho\nabla\Phi - \nabla P + \nabla\cdot\mathcal{T} \tag{2.22}$$

where P is the fluid pressure and Φ is the external potential. $\mathcal{T}$ is the stress tensor with diagonal elements T_{rr}, $T_{\phi\phi}$ and T_{zz}. The viscous stress $\mathcal{T}$ can be explicitly expressed as

$$\mathcal{T} = \mu\left[(\nabla v) + (\nabla v)^T\right] + \left(\mu_b - \frac{2}{3}\mu\right)(\nabla\cdot v)\,\mathcal{I} \tag{2.23}$$

where μ_b is the bulk viscosity and μ is the shear viscosity of the fluid. $\mathcal{I}$ is the identity matrix. For circular orbital motion, the only non-vanishing stress component is $T_{r\phi}$ and can be expressed as the product of the viscosity and the shear rate:

$$T_{r\phi} = T_{\phi r} = \mu r\frac{d\Omega}{dr}. \tag{2.24}$$

Converting equation 2.22 into cylindrical co-ordinate, the azimuthal component can be written as

$$\rho\left(\frac{\partial v}{\partial t} + \left(v\cdot\nabla\right)v + \frac{v_r v_\phi}{r}\right) = \frac{\rho}{r}\frac{\partial\Phi}{\partial\phi} - \frac{1}{r}\frac{\partial P}{\partial\phi} + \frac{1}{r^2}\frac{\partial}{\partial\phi}\left(r^2 T_{r\phi}\right) + \frac{1}{r}\frac{\partial}{\partial\phi}T_{\phi\phi} + \frac{\partial}{\partial z}T_{\phi z} \tag{2.25}$$

Assuming the potential Φ to be axisymmetric, the first term on the RHS of equation 2.25 vanishes. With the fact that the azimuthal velocity $v_\phi = r\Omega$ and the specific

angular momentum $h = r^2\Omega$, equation 2.25 can be recast as

$$\rho v_r \frac{dh}{dr} = \frac{1}{r}\frac{\partial}{\partial r}\left(r^2 T_{r\phi}\right) + \frac{1}{r}\frac{\partial}{\partial r}\left(-rP + rT_{\phi\phi}\right) + \frac{\partial}{\partial z}\left(rT_{\phi z}\right). \tag{2.26}$$

Multiplying equation 2.26 with r and integrating over the full extent of ϕ and z, we get

$$\mathcal{F}\frac{dh}{dr} = -\frac{\partial \mathcal{G}}{\partial r} \tag{2.27}$$

where we have used the viscous torque $\mathcal{G}$ as

$$\mathcal{G} = -\int_0^{2\pi}\int_{-\infty}^{+\infty} r^2 T_{r\phi}\, dz\, d\phi. \tag{2.28}$$

At this point we define a density weighted mean kinematic viscosity as

$$\bar{\nu} = \frac{1}{2\pi\Sigma}\int_0^{2\pi}\int_{-\infty}^{+\infty} \mu\, dz\, d\phi. \tag{2.29}$$

With this definition, the viscous torque in equation 2.28 becomes

$$\mathcal{G} = -2\pi r^3 \bar{\nu}\Sigma\frac{d\Omega}{dr}. \tag{2.30}$$

Using this equation 2.27 can be rewritten as

$$\Sigma\bar{u_r}\frac{dh}{dr} = \frac{1}{r}\frac{\partial}{\partial r}\left(\bar{\nu}\Sigma r^3\frac{d\Omega}{dr}\right). \tag{2.31}$$

Equation 2.31 is the statement of angular momentum conservation for a viscously evolving accretion disk. Note that the viscous torque in equation 2.28 is negative which is responsible for the inward mass flow in the disk.

2.2.6 Viscous Energy Dissipation, Accretion Luminosity & Temperature Profile

The luminosity of the accretion disk depends on the amount of energy viscously dissipated in the process of accretion. Understanding the combined effect of viscous dissipation and radiative cooling is profoundly important in the context of interpreting disk observations. In this section, we give a quantitative estimate of the viscous heat dissipation and the resulting accretion luminosity.

To start with, the energy dissipation can be estimated as the product of stress and strain. As we have seen earlier, the only component of the stress tensor responsible for driving accretion is the off-diagonal term $T_{r\phi}$. Also, the strain can be expressed as the velocity gradient in the radial direction and can be written as $r\, d\Omega/\, dr$. Hence, the viscous energy dissipated per unit time comes out as

$$\dot{Q}_{visc} = \nu \Sigma r^2 \left(\frac{d\Omega}{dr} \right)^2 \tag{2.32}$$

With $\Omega = \sqrt{GM/r^3}$ for a Keplerian disk, $d\Omega/\, dr = -(3/2)(\Omega/r)$. Thus, the energy dissipation rate is

$$\dot{Q}_{visc} = \frac{9}{4} \Omega^2 \nu \Sigma. \tag{2.33}$$

In case of disk observations, ν can be estimated from time dependent phenomena; e.g., in dwarf nova outburst, in which case the viscosity comes out as $\nu \sim 10^{15}$ cm^2 s^{-1}. However, from the observed luminosity of the disk, it is possible to estimate the mass accretion rate $\dot{M}$. Equation 2.33 above, in terms of $\dot{M}$ can be cast as

$$\dot{Q_{visc}} = \frac{3\dot{M}\Omega^2}{4\pi} \left[1 - \left(\frac{r_{in}}{r} \right)^{1/2} \right]. \tag{2.34}$$

where r_{in} is the inner radius of the disk. Considering that the viscously dissipated energy set the temperature of the disk, the radial temperature profile for a classical

accretion disk becomes

$$T^4 = \frac{3GM_\star \dot{M}}{8\pi\sigma r^3}\left[1 - \left(\frac{r_{in}}{r}\right)^{1/2}\right] \tag{2.35}$$

considering that the viscous heat escapes from both faces of the disk. Here σ is the Stefan-Boltzmann constant. Equation 2.35 states that at sufficiently large distances ($r >> r_{in}$), the temperature of the disk varies as $T \propto r^{-3/4}$. Interestingly, this particular variation is same for a passive disk in which the only source of heating is the radiation from the star.

2.2.7 Vertical Structure

In the vertical direction, the length scales of a protoplanetary disk can be estimated, to first order approximation, by considering vertical hydrostatic equilibrium. In general, the disk geometry can be expressed in simplest form in a cylindrical (R, ϕ, z) coordinate system. Identifying the vertical direction of the disk as the z-direction, the equation for hydrostatic equilibrium can be written as

$$\frac{\partial P}{\partial z} = -\rho g_z. \tag{2.36}$$

Here ρ is the gas density, g_z is the vertical component of the stellar gravity, and P is the thermodynamic pressure which, in the isothermal approximation, can be written as $P = \rho c_s^2$, where c_s is the isothermal sound speed. Equation 2.36 leads to Gaussian vertical stratification of gas density as

$$\rho(R, z) = \rho_0(R) e^{-z^2/h_g^2} \tag{2.37}$$

where, $\rho_0(R)$ is the midplane gas density at a distance R from the central star, and $h_g = c_s/\Omega$ is the gas scale height.

2.3 The Dust Disk & Dust Growth

Apart from gas, another major component of the disk is the dust. In spite of making a small contribution to total protoplanetary disk mass, dust affects the disk temperature by controlling absorption of starlight. For temperatures below 2000 K, the opacities of the disk material are dominated by the dust particles which play an important role in disk observations. Furthermore, dust provides the solid inventory in the disk essential for planet formation. Dust also play an active role in determining the strength of turbulence in the disk, and hence, the process of angular momentum transport, by controlling the abundances of ions and electrons. MHD turbulence is strong when there is a strong coupling between the ionized gas and the magnetic fields, which is set by the local ionization fraction. Dust play a crucial role in that context by assisting the recombination process through the adsorption of charged particles. In this section of the dissertation we give a brief overview on the physical processes governing the dynamics of dust grains in the disk and the temporal evolution of their abundance and size distributions.

2.3.1 Coupling between Dust and Gas: The Aerodynamic Drag

The dynamics of dust particles in a disk depends on the level of their coupling with the gas. Apart form the gravitational force of the central star, gas in the disk is also subjected to a force due to the radial pressure gradient. Adding this to the radial force balance equation 2.2, a more complete form can be written as,

$$\frac{v_\phi^2}{R} = \frac{GM_\star}{R^2} + \frac{1}{\rho}\frac{dP}{dR} \tag{2.38}$$

where, as before, v_ϕ is the azimuthal gas velocity and ρ is the local gas density. The last term in equation 2.38 indicates the force term originating from the radial pressure gradient. Assuming the radial profile of P has a power-law, the pressure can be expressed as

$$P = P_0 \left(\frac{R}{R_0}\right)^{-q} \tag{2.39}$$

where q is the power-law index and P_0 is the pressure at an arbitrary radius R_0. Writing $P = \rho c_s^2$, and substituting back in equation 2.38, the azimuthal velocity can be calculated as

$$v_\phi = v_K \left(1 - q\frac{c_s^2}{v_K^2}\right)^{1/2} \tag{2.40}$$

where, $v_K = \sqrt{GM_\star/R}$ is local Keplerian velocity. The term c_s^2/v_K^2 can be written in terms of the disk aspect ratio as $(h_g(R)/R)^2$ where $h_g(R)/R \sim 0.05$ is a reasonable estimate for the MMSN model with vertically isothermal assumption. Taking $\Sigma \sim R^{-1}$ and $T(R) \sim R^{-1/2}$, the value for q comes out to be -3 and equation 2.40 becomes: $v_\phi \sim 0.99 v_K$. Hence, the gas in the disk rotates with a velocity slightly smaller than the local Keplerian velocity.

Dust, on the other hand, behave mostly as a pressureless fluid and does not experience the force due to the pressure gradient. Hence, a dust particle embedded in the disk gas experiences a drag through a head wind and collides with gas molecules until it losses all of its linear momentum. One important aspect of dust dynamics in such conditions is to estimate the time scale, known as the friction time scale t_f, which is the ratio of the particle momentum to the drag force and gives an estimate of the time required to change the relative velocity between dust and gas substantially. The friction time-scale is

$$t_f = \begin{cases} \dfrac{\rho_m}{\rho_g}\dfrac{a}{c_s}, & \text{if } a \leqslant \frac{9}{4}\lambda_{mfp}, \qquad (2.41) \\ \dfrac{8}{3}\dfrac{\rho_m}{\rho_g}\dfrac{a}{C_D v_{dm}}, & \text{otherwise.} \qquad (2.42) \end{cases}$$

Here, ρ_m is the material density of dust, a is the size of the dust grain and λ_{mfp} is the mean free path of gas molecules defined as the average distance traveled by gas molecules between successive collisions and can be written as $\lambda_{mfp} = 1/(n\sigma_{H_2})$. Here σ_{H_2} is the average cross sectional area for hydrogen molecule, the main constituents of disk gas and n is the number density.

The friction time (or the stopping time) of a dust particle depends on Knudsen

number, defined by the ratio of the λ_{mfp} and the size of the dust grain a;

$$Kn = \frac{\lambda_{mfp}}{a} \tag{2.43}$$

The friction time in equation 2.41 is valid for the Epstein regime where $a \leqslant (9/4)\lambda_{mfp}$, or $Kn \geqslant (4/9)$. Equation 2.42, on the other hand, represents the friction time for the Stokes regime where $a > (9/4)\lambda_{mfp}$. In equation 2.42 v_{dm} is the relative velocity between dust and gas, and C_D is the drag coefficient which depends on the Reynolds number of dust-gas interaction Re, written as $Re = 2ac_s/\nu_{mol}$, where ν_{mol} is the gas molecular viscosity and is written as

$$\nu_{mol} = \frac{\bar{c_s}\lambda_{mfp}}{2} \tag{2.44}$$

where $\bar{c_s}$ is the mean thermal speed. From equation 2.41 and 2.42 it is clear that the friction times of dust particles depend both on the size of the particles and the gas density. If gas density increases, the required number of collisions between the dust particle and gas molecules to extract all of its momentum is achieved in a shorter time, effectively decreasing t_f. A dust particle with a larger size, on the other hand, needs more collisions with gas molecules to lose all its excess momentum and hence, t_f increases. It is also evident that t_f for particles of different sizes will differ depending on the location in the disk. Hence, for better comparison of the coupling for particles of different size and gas density, a dimensionless Stokes number is defined as

$$St = t_f\Omega. \tag{2.45}$$

Particles with $St = 1$ come to match the gas velocity in one local orbital period. For a wide range of gas densities, sub-micron dust grains have $St << 1$ and hence, come quickly to rest in the co-moving gas reference frame.

2.3.2 Relative Velocity of Collision

Starting from micron and sub-micron size, how dust particles grow through several decades in mass range by collision is a topic of special interest. The outcome of a binary collision depends on the relative velocity with which a pair of dust grains collide. Dust particles, embedded in the disk gas can have five different types of velocity contributions which depends on the size and coupling efficiency of the dust particles. For example, the tiny sub-micron and micron size particles execute random zig-zag motions in the gas and in that phase the contribution from the Brownian motion is the most important part. As the dust particles grow bigger in size and start to get decoupled from the gas, the contributions from the individual dust motions in radial, vertical and azimuthal directions and from the gas turbulence become more important. The important components of relative velocities that influence the dust growth are Brownian motion (Δv_B), radial drift (Δv_R), vertical settling (Δv_z), azimuthal drift (Δv_ϕ) and turbulent gas motion (Δv_t). The final relative velocity of collision, combining all these components, can be written as

$$v_{rel} = \{\Delta v_B^2 + \Delta v_R^2 + \Delta v_z^2 + \Delta v_\phi^2 + \Delta v_t^2\}^{1/2}. \tag{2.46}$$

Below we shall quantify the different components of the velocity acquired by the dust grains.

2.3.2.1 Brownian Motion (Δv_B)

Small dust grains, completely coupled to the gas, are constantly bombarded by the gas molecules from all directions and acquire a net systematic velocity component, often known as the Brownian motion. The differential equation expressing this motion, with the collisions with the gas molecules introduced as a random forcing, is known as Langevin's equation. The solution of Langevin's equation predicts a non-zero mean squared velocity component for the suspended dust particles. The relative velocity between two dust particles of masses m_1 and m_2 arising from Brownian motion is

given by

$$v_B = \sqrt{\frac{8k_B T(m_1 + m_2)}{\pi m_1 m_2}} \tag{2.47}$$

The Brownian motion is important for small dust grains and hence dominates in the early stages of the evolution of the dust size distribution. As can be seen from equation 2.47, for similar masses m_1 and m_2, $v_B \propto 1/m$. Hence, when the dust particles have grown to $\sim 10\mu$m, the relative velocity contribution from Brownian motion starts to fade away.

2.3.2.2 Radial Velocity (Δv_R)

As seen in section 2.3.1, due to a sub-Keplerian gas velocity, the dust particles experience a headwind and constantly get bombarded by the gas molecules. In this process, dust grains lose their angular momentum and start moving radially inward. The velocity of this inward radial drift is a function of the mass of the dust particles, and particles of different sizes acquire different drift speeds, giving rise to the radial component of relative velocity of collision. The inward drift speed of a particle with a Stokes number St has two components and can be quantified as

$$v_R = \frac{v_g}{1 + St^2} + \frac{2v_\eta}{St + \frac{1}{St}} \tag{2.48}$$

where v_g is the gas velocity given by equation 2.8. The first term in equation 2.48 is the contribution from gas velocity. Particles, which are fully coupled to the gas, would follow the gas accreting inward. This component of the velocity is always directed inward. The second term above is the contribution from the particle velocity that arises due to its movement towards the pressure maximum. The term v_η in equation 2.48 can be written as

$$v_\eta = \frac{\nabla_R P_g}{2\rho_g \Omega} \tag{2.49}$$

where P_g is the gas pressure. If two dust particles with masses m_1 and m_2 have Stokes number St_1 and St_2 respectively, then the radial component of the relative velocity

can be written as

$$\Delta v_R = |v_R(St_1) - v_R(St_2)| \tag{2.50}$$

2.3.2.3 Azimuthal Component (Δv_ϕ)

The relative velocity component arising from the differential azimuthal velocity of two dust particles can be written as

$$\Delta v_\phi = |v_\phi(St_1) - v_\phi(St_2)| \tag{2.51}$$

where,

$$v_\phi = -\frac{v_\eta}{St + \frac{1}{St}}. \tag{2.52}$$

Same as above, v_η is given by equation 2.49. Neglecting the back reaction from the gas, v_ϕ can also be stated as the deviation of the azimuthal velocity of the dust particles from the local Keplerian speed.

2.3.2.4 Vertical Component (v_z)

Dust particles, situated at the upper layers of the disk, experience a systematic movement towards the disk midplane due to the vertical component of the stellar gravitational force. The settling velocity for a particle of mass m (size a) at a height z from the midplane can be written as

$$v_z = \frac{a}{\bar{c_s}} \frac{\rho_m}{\rho_g} \Omega^2 z \tag{2.53}$$

where, ρ_m is the material density of dust grains. The differential settling speed between two particles of masses m_1 (size a_1) and m_2 (size a_2) becomes

$$\Delta v_z = |v_z(a_1) - v_z(a_2)| \tag{2.54}$$

2.3.2.5 Turbulent Velocity (Δv_t)

The last and probably the most complex component of relative velocity contribution comes from the turbulent motion of dust particles. To what extent the turbulent gas in the disk affects the dust motion depends on the friction time of the dust particle and how it compares to the eddy crossing time and eddy turnover time of the turbulent gas. Assuming a Kolmogorov type turbulence model for the disk gas, the velocity of the k^{th} mode can be written as $v(k) = \sqrt{2kE(k)}$, where $E(k)$ is the energy contained in the k^{th} mode. Also, the turnover time of an eddy of scale l and wavenumber $k = 1/l$ is $t_k = l/v(k)$. Now, if l_L is the largest length scale of the turbulence where the inertial range starts and the energy is injected, and l_K be the smallest scale (Kolmogorov scale) where the energy is dissipated, we can write, $l_K/l_L = Re^{-3/4}$, where Re is the Reynolds number. Also, the timescales t_K and t_L are related by $t_K/t_L = Re^{-1/2}$. Considering $t_L \sim 1/\Omega$, the Stokes number can be expressed as $St = t_f/t_L$.

For a dust particle with Stokes number St encountering an eddy with a turnover time t_{eddy}, if the friction time $t_f < t_{eddy}$, the dust particle will lose all of its original momentum and will align itself with the gas motion before the eddy decays or the particle leaves the eddy. If, on the other hand, the t_{eddy} is small compared to t_f, the eddy only provides a small perturbation to the motion of the dust particle. Based on this formalism, Ormel and Cuzzi [2007] have given a comprehensive closed form expression for turbulent relative velocity between two dust grains of stopping times t_1 and t_2 with $t_1 > t_2$ (and $St_1 > St_2$) in three limiting cases. For tightly coupled particles, where $t_1, t_2 < t_K$, the relative velocity can be written as

$$\Delta v_t^2 = v_g^2 \frac{St_1 - St_2}{St_1 + St_2} \left(\frac{St_1^2}{St_1 + Re^{-1/2}} - \frac{St_2^2}{St_2 + Re^{-1/2}} \right). \tag{2.55}$$

Here v_g is the fluctuation velocity of the gas and is given by $v_g = (\sqrt{3/2}) v_k Re^{1/4} = (\sqrt{3/2}) v_k (t_L/t_K)$. In the limit of very small particles where $t_1 << t_K$, Δv_t in equation 2.55 becomes

$$\Delta v_t^2 = v_g^2 \frac{t_L}{t_K} (St_1 - St_2)^2 . \tag{2.56}$$

In the intermediate regime, where $t_K < t_1 < t_L$, the relative velocity Δv_t is given by

$$\Delta v_t^2 = v_g^2 \left[2y_a - (1+\epsilon) + \frac{2}{1+\epsilon} \left(\frac{1}{1+y_a} + \frac{\epsilon^3}{y_a+\epsilon} \right) \right] St_1. \tag{2.57}$$

Here, $\epsilon = St_2/St_1$ and $y_a \approx 1.6$, a constant calculated by Ormel and Cuzzi [2007]. In the third and final case, where $t_1 > t_L$, Δv_t becomes,

$$\Delta v_t^2 = v_g^2 \left(\frac{1}{1+St_1} + \frac{1}{1+St_2} \right). \tag{2.58}$$

From equation 2.58 if both Stokes numbers are large, the relative velocity decreases as the square root of the smaller stopping time.

2.3.3 Collision Outcomes

The outcome of a modeled collision between two dust particles in a protoplanetary environment has many possibilities according to laboratory experiments. On the experimental side, Güttler et al. [2010] presented 19 possible collisional outcomes for particles with various mass ratios, speeds, and porosities. However, it is prohibitively computationally expensive to include all possibilities in a global disk model. For simplicity, in this dissertation we adopt a collisional model that includes only sticking and fragmentation for all our simulations. We treat collisions as a binary process, identifying the smaller mass as the projectile (m_p) and the bigger mass as the target (m_t). The collision outcome is determined by the relative velocity (see §2.3.2 for a description of our velocity computation). If the particles collide with a velocity less than a threshold velocity v_{frag}, they stick and form a new particle with mass $m_{final} = m_p + m_t$. When $v_{rel} > v_{frag}$, the collision results in fragmentation.

As particles grow by sticking, their eddy-crossing times drop, leading to lower coupling with the gas and higher collision speeds [Ormel and Cuzzi, 2007]. When the collision speed reaches v_{frag}, instead of sticking, both particles fragment. For such an event the combined mass of the target and the projectile is made to follow a mass distribution $f(m)\,dm \propto m^{-\xi}\,dm$ with ξ being the fragmentation distribution power law

index. Here we adopt $\xi = 11/6$ [Windmark et al., 2012b, Drążkowska et al., 2014, Krijt and Ciesla, 2016], though we note that some experiments predict a shallower fragment size distribution with $\xi = 9/8$ [Blum and Wurm, 2000, Güttler et al., 2010].

When the ratio of target to projectile mass is high and the particles collide with $v_{rel} > v_{frag}$, a possible outcome can be mass-transfer. In this case, in stead of a catastrophic disruption of the particles a certain fraction of mass is transferred from projectile to target. Drążkowska et al. [2013] have adopted a value of 20 for m_p/m_t for mass transfer event to take place and systematically transferred 10% of the projectile mass to the target. Mass transfer is generally sought as an alternative pathway for planetesimal formation [Windmark et al., 2012a, Drążkowska et al., 2013]. However, Estrada et al. [2016] have shown that in the presence of strong radial drift, the effect of mass transfer is mitigated. Hence mass-transfer is not included in our models.

Another possible outcome of a binary collision is erosion, where a certain fraction of target mass is eroded by the projectile and the projectile itself gets fragmented. Generally this process requires a velocity of collision which is substantially higher that the values adopted for v_{frag}. Birnstiel et al. [2011] have shown that in the presence of erosion in the collision model, the size distribution gets a distinct shallow dip near the largest end. However, this effect is small and does not significantly affect the nature and properties of the synthetic observations.

2.3.4 Vertical Diffusion of Dust

Vertical dust settling plays a significant role in determining the dust abundance as a function of height, which in turn affects the collision frequency, grain size distribution, and opacity. Dust particles at a certain height z above the midplane settle due to the vertical component of stellar gravity, while being diffused at the same time due to gas turbulence. The process of diffusion depends on the level of turbulence efficiency α and the coupling between the gas and the dust.

The continuity equation for vertical dust dynamics in 1D is

$$\partial_t \rho_d + \partial_z F = 0 \tag{2.59}$$

where F, the total vertical diffusive flux of dust particles, is composed of three components: vertical settling due to stellar gravity, diffusion of dust towards density maxima, and stirring of dust by gas turbulence. The diffusion equation governing all the three effects can be written as [Dubrulle et al., 1995, Takeuchi and Lin, 2002, Fromang and Papaloizou, 2006]

$$\frac{\partial \rho_d}{\partial t} = \frac{\partial}{\partial z}\left[D_d \rho_g \frac{\partial}{\partial z}\left(\frac{\rho_d}{\rho_g}\right)\right] + \frac{\partial}{\partial z}\left(\Omega^2 t_f \rho_d z\right) \tag{2.60}$$

where D_d is the dust diffusion coefficient and is given by

$$D_d = \frac{D_g}{1 + St^2}. \tag{2.61}$$

Here D_g is the gas turbulent diffusivity, $D_g = \alpha c_s h_h$. Equation 2.60 expresses the evolution of dust density ρ_d in terms of the gradient of the tracer concentration ρ_d/ρ_g. After a little algebra, it can be re-written as

$$\frac{\partial \rho_d}{\partial t} = \frac{\partial^2 D_d \rho_d}{\partial z^2} - \frac{\partial}{\partial z}\left(\rho_d D_d \frac{1}{\rho_g}\frac{\partial \rho_g}{\partial z}\right) + \frac{\partial}{\partial z}\left(\rho_d z \Omega^2 t_f\right). \tag{2.62}$$

The term $D_d/\rho_g \times \nabla\rho_g$ arises when the diffusion equation, which operates on the gradient of tracer concentration ρ_d/ρ_g, is transformed into an equation that operates on the gradient of particle density alone. Equation 2.62 can be solved by a Lagrangian random walk technique involving a 'kick' in position space in terms of a Gaussian random variable with mean μ and variance σ^2 given as

$$\mu = \Delta z_s + \left[\frac{D_d}{\rho_g}\partial_z \rho_g + \partial_z D_d(z)\right]\delta t \tag{2.63}$$

$$\sigma^2 = 2D_d(z)\delta t + \left[(\partial_z D_d)\delta t\right]^2 . \tag{2.64}$$

The terms in the square bracket in equation 2.63 capture two different physical effects on dust diffusion: the non-uniform gas density and the non-uniform diffusivity. The last term in equations 2.64 arises due to variations in the dust diffusion coefficient D_d. The first term in equation 2.64, $2D_d\delta t$, comes from turbulent diffusion and describes particle stirring.

It is important to note that the same solution can also be written in the velocity space representation. However, as can be seen from equations 2.63 and 2.64, transforming from position to velocity space brings the time δt to the denominator and hence, a convergence problem arises. Working in the position space Lagrangian approach provides the freedom of choosing any timestep for numerical implementation.

2.3.5 Dust Scale Heights

The vertical scale height for dust particles is generally calculated by equating their vertical settling time scale to the turbulent diffusion time scale for dust particles. The settling time scale can be written as

$$t_{sett} = \frac{z}{v_{sett}} = \frac{c_s}{a}\frac{\rho_g}{\rho_m}\Omega^{-2}, \tag{2.65}$$

and the vertical diffusion time scale as

$$t_{visc} = \frac{z^2}{D_d} = \frac{z^2(1+St^2)}{\alpha c_s h_g}. \tag{2.66}$$

Comparing equations 2.65 and 2.66, the dust scale height h_d becomes

$$h_d = h_g\left(1+\frac{St}{\alpha}\right)^{-1/2} . \tag{2.67}$$

For tightly coupled particles with very small St, the dust scale height becomes close to the gas scale height h_g.

We note that equation 2.67 also gives an approximation to the steady state dust scale height and has been used for our initial setup. Estrada et al. [2016] use the same prescription (equation 2.67) for dust scale height to distribute solids in the vertical direction which extends their model to $1 + 1$D from a 1D gas diffusion model. This method works perfectly fine as the vertical diffusion timescale is small compared to the inward drift timescale. However, Mulders and Dominik [2012] showed that the midplane approach of equation 2.67 from Dubrulle et al. [1995] estimates a higher dust abundance towards the disk surface compared to the abundance obtained when St is calculated locally. This occurs because, in the approach of Dubrulle et al. [1995] St for particles with a certain size is calculated using the midplane gas density and such a particular value of St is used for the whole vertical column. Hence, to compute a more realistic vertical structure in our disk models with layered accretion, parameters such as Stokes number for individual particles are calculated locally. Thus, the prescription from Charnoz et al. [2011] gives a more accurate result.

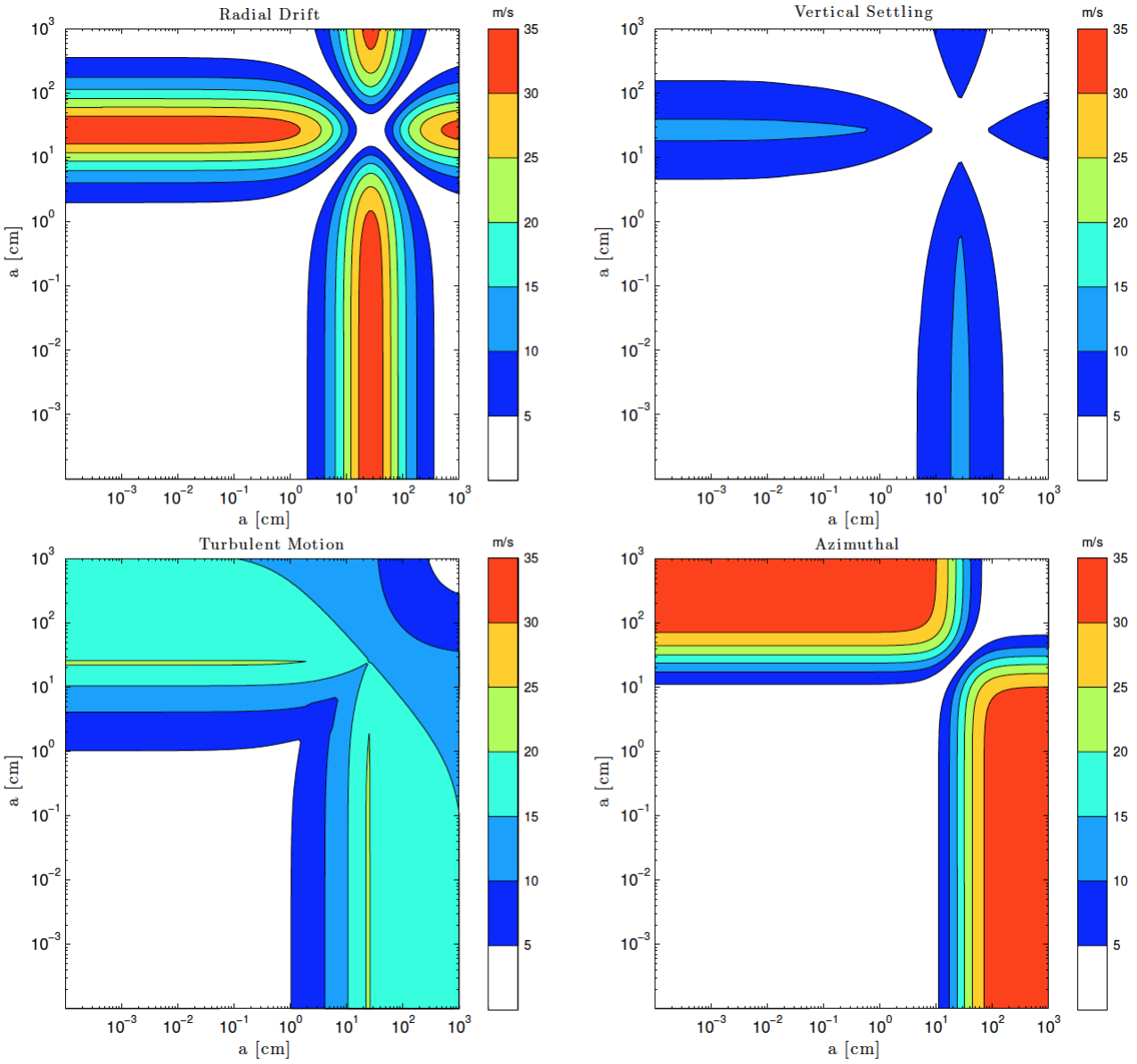

Figure 2.1: The different components for particle relative velocity of collision. Brownian motion is not shown here. The Figure is taken from Birnstiel et al. [2010] with permission.

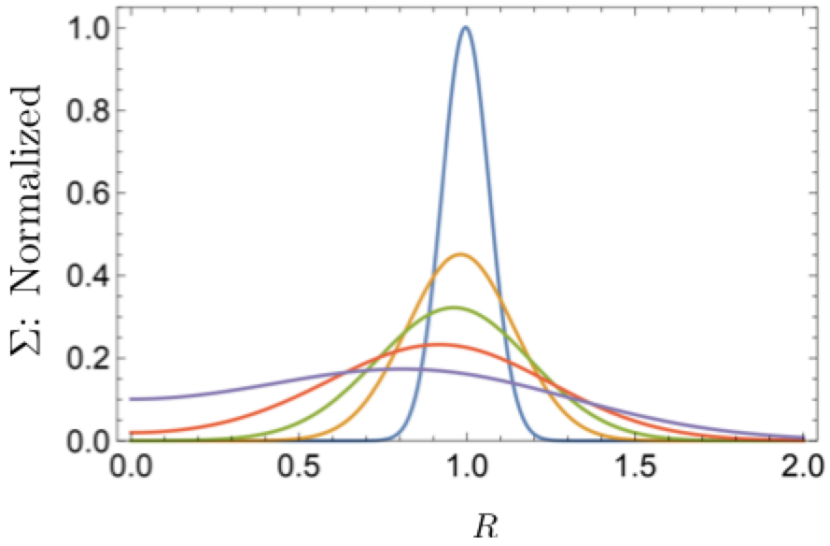

Figure 2.2: The Green's function solution for the accretion equation. While most of the matter moves inward and accretes on to the star, a small amount of matter goes radially outward, carrying most of the angular momentum away as $t \to \infty$.

Chapter 3

THE NEW WEIGHTED MONTE CARLO DUST MODEL: ALGORITHM, IMPLEMENTATION & TEST RESULTS

3.1 Introduction

Planet formation starts with (sub)-micron sized dust particles which grow through the processes of collisional sticking and fragmentation. Apart from providing the solid inventory for planets, dust grains control the key disk physical processes as well. Starting from the nature and strength of disk turbulence, the temporal evolution of the disk, the diversity of planetary composition and chemical compositions of disk materials are all directly or indirectly affected by the dynamical, thermal and radiative properties of dust. Hence, performing numerical simulations of global dust evolution with masses ranging over several decades for a few million year timescale is an important task. Collisional dust growth and dynamics in a planet forming disk are generally modeled by either solving Smoluchowski's equation [Nakagawa et al., 1981, Birnstiel et al., 2010] or with a Monte Carlo simulation [Ormel and Spaans, 2008, Zsom and Dullemond, 2008], or using moments of the dust distribution [Estrada and Cuzzi, 2008]. Although Smoluchowski's method of tracking the temporal evolution of dust size distribution is fast and computationally inexpensive even when the distribution is wide, it has its own limitations [Ohtsuki et al., 1990, Drążkowska et al., 2014]. Adding additional particle properties and tracking them through the course of dust evolution, such as porosity, charge, or compositions, makes this method extremely complex. Also, a lack of adequate resolution in the particle mass range leads to a faster, unphysical growth of dust. To avoid this systematic error, a fine resolution is required that leads to a high computation cost. More importantly, the method lacks the inherent stochasticity of a random dust growth process. The Monte Carlo method of particle growth, on the

other hand, can capture the stochasticity and more realistically simulate the system's physics. Drążkowska et al. [2014] showed in a comparative study that the result of Monte Carlo techniques are not as sensitive to the resolution of the particle size distribution. However, for simulating dust behaviors throughout the disk over 10 kyr, Monte Carlo methods can be computationally expensive. As the error in this method goes as $1/\sqrt{N}$, where N is the number of Monte Carlo particles used in the simulation, a reasonably high value of N is desired to achieve enough fidelity, making the method an expensive one. Monte Carlo methods also lack the dynamical range that can be easily achieved by Smoluchowski's method. In this thesis, we present a new Monte Carlo model that overcomes these difficulties and can achieve a larger dynamical range by using a weighting technique. The schematic plot of our Quasi-Linear Monte Carlo (QLMC) algorithm is shown in Figure 4.1, and the key quantities are listed in Table 3.1.

3.2 Brief Descriptions of Existing Models

The most common and fast way of modeling collisional dust growth through sticking and fragmentation is the method of solving Smoluchowski's equation by implicit integration technique. In this method, the coagulation and fragmentation events are generally modeled as a two-body processes and the number density distribution of dust is evolved with time using a collision kernel as

$$\frac{\partial}{\partial t} n(m) = \int_0^\infty \int_0^\infty K(m, m', m'') \times n(m') \times n(m'')\, dm'\, dm''. \tag{3.1}$$

Here $n(m)$ represents the number density of particles of mass m with $n(m)\, dm$ is the number of particles in a unit volume element with mass ranging between m and $m + dm$. $n(m)$ is related to the dust density ρ_d by

$$\rho_d = \int_0^\infty n(m)\, dm. \tag{3.2}$$

In equation 3.1, $K(m, m', m'')$ is the collision kernel that incorporates the effect of different collision outcomes, such as coagulation (sticking) and fragmentation. The kernel can be explicitly written as

$$\begin{aligned} K(m, m', m'') = \frac{1}{2} S(m', m'') \cdot \delta(m' + m'' - m) \\ - S(m', m'') \cdot \delta(m'' - m) \\ + \frac{1}{2} F(m', m'') \cdot D(m, m', m'') \\ - F(m', m'') \cdot \delta(m - m''), \end{aligned} \tag{3.3}$$

where, m' and m'' are the target and projectile masses respectively. Here S is the sticking kernel, F is the fragmentation kernel and D is the kernel representing the fragmenting size distribution. As can be seen from equation 3.3, the sticking kernel is attached to a delta function $\delta(m' + m'' - m)$ which is true for $m = m' + m''$ that signifies a sticking event. The fragmentation kernel $F(m', m'')$, on the other hand, is connected to the distribution operator $D(m, m', m'')$ that distributes the fragments of smaller masses in a size distribution with a chosen power-law index. The kernels S and F are generally written as a product of collision relative velocities $v_{rel}(m', m'')$ and geometric cross-section of collision $\sigma(a', a'') = \pi(a' + a'')^2$, where a' and a'' are the radii of dust particles of masses m' and m'' respectively. Equation 3.1 is then solved by an implicit integration method at each R and z location of the disk. Here, R is the radial distance from the central star and z is the vertical height over the disk's midplane.

Another important and well studied method for modeling dust growth through coagulation and fragmentation is the kinetic Monte Carlo method. This method has been used with different implementations in various works in the literature (ref). Here, a certain number (N) of test particles are used to track the evolution of the grain size distribution with time. First, the rates of collisions for each particle pair are calculated using the local parameters as $r_{ij} = n\sigma v_{rel}$, where r_{ij} is the collision rate between test particles i and j. Once the distribution is made from all $N(N-1)/2$ possible collision pairs, the successful collision for a particular step is randomly selected from the

distribution. The time for that step is then evolved according to the prescription from [Gillespie, 1975] (See section 3.3.5 for further details). Although it is more convenient to keep track of dust properties in this method, Monte Carlo algorithms suffer from the inherent $O(N^2)$ nature. Every step of this process involves the calculation of $\sim N^2$ rate calculations which makes the process computationally expensive. Furthermore, the error in this process is of the order $1/\sqrt{N}$, which makes the method less precise if a small value for N is chosen.

The main goal of this dissertation is to develop with a dust model which is capable of providing a realistic vertical structure in the course of global dust evolution while keeping the method within feasible computational reach. Below, we describe our model in details.

3.3 The New Monte Carlo Model: Algorithm

The algorithm of our dust model is tuned towards achieving a reasonable fidelity and minimizing the computation expense at the same time. In order to be able to perform global simulations within a few days of physical time, we have developed a Monte Carlo dust growth model that is linear in nature. Furthermore, to track the evolving particle size distribution with a lower number of Monte Carlo particles, we have implemented a weighting technique in our model. Below we discuss our algorithm in details and test our model with the results from various other models already existing in literature.

3.3.1 Selecting Collision Pairs

We start by dividing the total mass range of dust grains *in each grid zone* into N_H equally spaced logarithmic histogram bins. At any given instant t, N particles are drawn randomly from the particle mass distribution in that grid zone. We found converged results for $N = 60000$ and adopted that value for the simulations presented here. We denote the first array of Monte Carlo particles in any given grid zone by subscript 'q'. (Below we will describe the selection of a second set of Monte Carlo

particles in each grid cell to serve as potential collision partners.) If N_i is the number of particles drawn from the i^{th} bin in the particle mass distribution, we have

$$\sum_{i=1}^{N_H} N_i = N. \tag{3.4}$$

Given that $\rho_{d,i}$ is the dust mass per unit disk volume represented by bin i in the mass distribution and $\log m_i$ is the value of $\log m$ at the center of i^{th} bin the *number density of particles per* cm^3 contributed by bin i is $n_{d,i} = \rho_{d,i}/m_i$. Finally,

$$n_{d,i} = f_i n_d, \tag{3.5}$$

where n_d is the total number density of the dust grains *of all masses* in the grid cell and f_i is the fractional abundance of dust grains of mass m_i, such that

$$\sum_{i=1}^{N_H} f_i = 1. \tag{3.6}$$

In the same timestep and grid cell, another N particles, denoted by subscript 'k', are drawn randomly from the same particle mass distribution to be the possible collision partners. The dust mass distribution after a particular timestep is determined by the outcome of a collision chosen from these N particle pairs (see §2.3.3). Unlike Ormel et al. [2007] or Zsom and Dullemond [2008], we only partially trace the evolution of a specific set of particles over time (See §3.3.2).

During the random selection of sets q and k of potential colliders, the number of particles we draw from each mass bin is $f_i N$, unless particles of mass m_i are rare enough that $f_i N < 1$. Here we introduce a weighting scheme to make sure that the rare particles are not lost from the simulation, as a few large particles may dramatically alter the particle mass distribution by sweeping up smaller grains [e.g. Windmark et al., 2012a]. From the particle mass bins with $f_i N < 1$, a single particle is randomly selected from each bin's mass range and a weight $w_i = f_i N$ is assigned to that particle. For

particles drawn from bins with $f_i N > 1$, $w_i = 1$. The weight can be interpreted as a fraction of the particle that truly exists in the distribution. After picking the selected number of particles from each bin, the order of particles in the two arrays q and k is randomized.

In each grid zone, for each timestep, we allow only one collision to proceed successfully. For each particle in set q, collisions with its partner in set k proceed at a rate

$$P_k = n_k \sigma_{qk} \delta v_{qk}, \tag{3.7}$$

collisions per second, where σ_{qk} is the collision cross-section $\pi(r_q + r_k)^2$. The relative collision velocity δv_{qk} is calculated according to the prescription outlined in section 2.3.2. The number density n_k, reperesented by the k^{th} particle, is:

$$n_k = \frac{n_{d,i}}{N_i} = \frac{f_i n_d}{N_i}, \tag{3.8}$$

where i is the mass bin corresponding to particle k. At this point, we choose a single pair of particles from N possible collision pairs from the distribution of P_k obtained from equation 3.7 by using a single random number drawn from a uniform distribution between 0 and 1. At any particular step only a single collision is allowed and the corresponding time is updated by the method explained in §3.3.5.

For a sticking event between two particles of masses m_q and m_k, the final mass is set as $w_q m_q + w_k m_k$ and is transferred to the bin containing mass $m_q + m_k$. Similarly, for a fragmentation event, the total mass put into the size distribution of fragments is $w_q m_q + w_k m_k$. After the collision, a new particle mass distribution is calculated. For the next timestep, the mass distribution is again transformed into number density space using Equations 3.4-3.6 and the new sets q and k are selected to again make N particle pairs.

3.3.2 A Two-Step Random Selection

The model presented here consists of repeated sampling of the size distribution to select particles and their collision partners. In the process of collisional growth, before the fragmenting threshold velocity is reached, the bins towards the higher mass end of the distribution contribute single particles to the total population of N particles. It is not always guaranteed that the single particle will be picked during random sampling and hence the growth can be hindered artificially. To circumvent this problem, the random selection is done in a two-step process. First, the number of particles to be selected from each bin is calculated according to Equations 3.4 and 3.5 (See §3.3.1). Next, after ensuring the right number of particles are drawn from each bin, the array of particles is randomized. The same process is followed for the selection of collision partners as well.

3.3.3 Mass Conservation

One important part of our code is ensuring mass conservation locally and in each vertical column (recall that particles are not allowed to migrate radially between columns). Mass is conserved during collisions, but may be lost or gained in numerical noise when computing the particle mass histogram after each timestep. Mass loss is more likely, since the largest and rarest particles contain the bulk of the mass: at the large end of the size distribution, the difference between the maximum mass in a histogram bin and the bin center can be a significant fraction of the total particle mass in the grid zone. We conserve mass in our simulation by updating the total number density n_d in each grid zone after each timestep. The number density change is

$$n_d \leftarrow \frac{M_{total}}{\sum_i m_i f_i}, \tag{3.9}$$

ensuring that each mass histogram bin will contain the correct fraction of the grid zone's total mass. No bin m_i can then lose mass by dropping a particle near its upper mass boundary. This allows us to conserve mass to almost the machine precision.

3.3.4 Artificial Oscillation & Partial Particle Tracking

The imposed mass conservation can cause artificial oscillation in the number of particles at the smaller sizes in the dust-mass spectrum. Given that the masses of the bigger particles are not necessarily equal to the respective bin center masses, using equation 3.9 would force the total number of small particles to change to accommodate a single large particle's shift to the bin center. We remove the oscillations by retaining the same individual particles between timesteps in the low-statistics bins instead of subsuming them into the new particle mass histogram calculated at the end of each timestep. This technique helps to track the dust growth in a more accurate way. For this work, we tracked particles from any bin contributing less than 10 particles and this number is kept constant throughout the simulations.

3.3.5 Calculating the Timestep Between Collisions

After finding the successful collision in each grid zone, the next step in our simulation is to calculate the timestep δt. Codes that follow the kinetic Monte Carlo method set δt by first computing P_{total}, the total collision rate from *all* $N(N-1)/2$ possible particle pairs from sets q and k; then using a random number r selected from uniform distribution between 0 and 1, the timestep is calculated as

$$\delta t = -\frac{1}{P_{total}} \ln(r) \tag{3.10}$$

[e.g. Gillespie, 1975, Ormel et al., 2007, Zsom and Dullemond, 2008].

It is evident that in our method it is not possible to calculate the time evolution following Equation 3.10 as we do not calculate the rates for all $N(N-1)/2$ possible pairs while selecting the successful collision at any step. Instead, we implement a matrix partitioning method in which the particles are first binned in the mass histogram. We now assume that out of these N particles, the N_i ones belonging to the i^{th} histogram bin represent the same mass m_i corresponding to that particular bin center. Moreover, the original particles being drawn from the number density distribution $f(n)$, every

particle grouped into a single bin represents the same number density in the underlying population. So, instead of calculating individual rates, we assume every pair belonging to the same histogram bin contributes equally to the total rate P_{total}. Considering that we are calculating the rate between the particles in the i^{th} bin for the first array and the j^{th} bin for the collision pairs, we calculate the rate of collision for a single pair by $n_{d,j}\sigma_{ij}v_{rel,ij}$ (Note the change in index from q and k to i and j as particles are represented by their corresponding bins). Thus, the total rate for all the pairs coming from the i^{th} bin for the first array of particles and j^{th} bin for the collision partners can be written as:

$$P_{ij} = n_{d,j}\sigma_{ij}v_{rel,ij}N_iN_j \tag{3.11}$$

The total collision rate at any point in time is then obtained by summing equation 3.11 over each histogram bin and can be written as:

$$P_{total} = \sum_{i=1}^{N_H}\sum_{j=1}^{N_H} n_{d,j}\sigma_{ij}v_{rel,ij}N_iN_j. \tag{3.12}$$

For collisions between particles of exactly equal mass, the turbulent relative velocity $\delta v_t = 0$ when the particle size is very small and no random velocities are excited by the class 2 eddies for which the particle stopping time (t_{fric}) is less than the eddy turnover time at the Kolmogorov length scale [see Ormel and Cuzzi, 2007]. Hence, to accurately capture the turbulent velocity contribution to P_{total} the masses of the N_i and N_j particles in equation 3.12 are chosen randomly between the bin edges instead of the mass equal to the bin center. Also, similar to §3.3.4 above, for the particles featuring low statistics, the exact particle mass is used to calculate the rate. Finally, we use Equation 3.10 to select the timestep δt, which ranges from a few seconds to $\sim 10^3$ seconds depending on time and location in the disk. For finely spaced particle mass histograms, Equation 3.12 is an excellent match to the kinetic Monte Carlo method.

In section 3.6 we show that our method closely reproduces a range of results from the literature. We also check the masses of the largest particles produced by our code

against analytical estimates (Equation 3.16) of the maximum mass when turbulence controls the collision speed.

3.3.6 Gaining Efficiency

In general, Monte Carlo is an $O(N^2)$ method in which most of the computation time is spent on calculating the rates of collision between different particle pairs. For N number of Monte Carlo particles used in the simulation, the $O(N^2)$ method involves N^2 rate calculations and the CPU time becomes proportional to N^2. Our method, being effectively an $O(n)$ model on the other hand, calculates only $N + N_H^2$ collision rates of which the N_H^2 is for computing the time evolution. As long as $N_H \ll N$, the time saved is significant. Here we use $N_H = 80$ which provides good resolution in the mass histogram while satisfying $N_H^2 \ll N$. For example, calculating the steady-state size distribution at a single grid point takes $\sim 3-10$ hours to reach steady state depending on the model parameters with a single processor. The global model with MMEN surface density and $\alpha = 10^{-5}$ takes ~ 3 days with 48 processors. For comparison, Drążkowska et al. [2013] reported their computation time for a global model as a few weeks.

3.4 Vertical Motion of Particles

Following the model of dust growth through coagulation and fragmentation, our next job is to implement the settling and turbulent diffusion of dust particles in the vertical direction. For this, we have adopted the theoretical framework of Charnoz et al. [2011] as described in section 2.3.4, and implemented the prescription using a Monte Carlo algorithm. In figure 3.1, we have presented a schematic diagram of the algorithm. In our implementation, we track the movement of a fairly large number of particles following the steps below:

1. At each disk radius R_j, select N_s Monte Carlo particles (subscript u) of mass m_i to represent *each* bin m_i in the particle-mass histogram.(We find a smooth representation of the vertical number density distribution with $N_s = 10^5$ and adopt that value for all simulations presented here.)

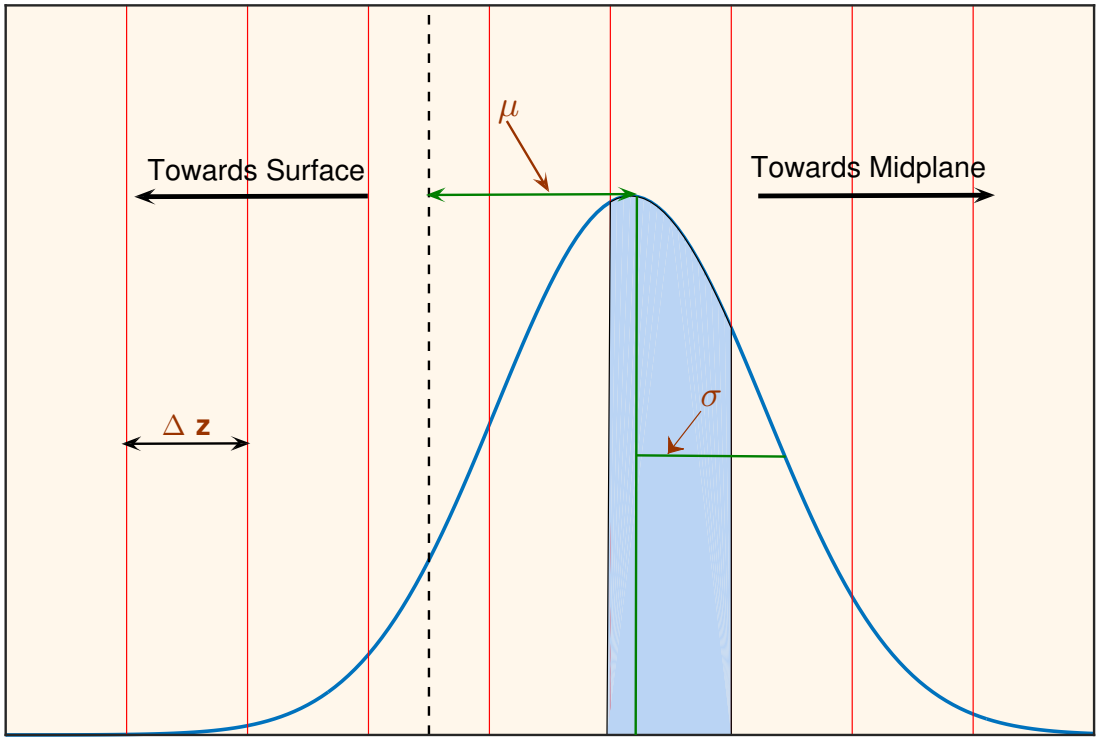

Figure 3.1: A schematic of the settling algorithm implemented in our work. The vertical dashed black line is the height of the *middle* of the cell the particle inhabits. Before each settling step, dust particles of radius a are spread from the top to the bottom of the vertical column according to the background dust distribution. A particle of size a is then redistributed according to the prescription given by Equations 2.63 and 2.64 (solid blue line). Red lines mark boundaries between cells, and the shaded region shows the probability that the particle will be moved from the original cell to that particular cell. A similar Gaussian is considered for each of the N_s dummy particle used in the settling algorithm.

2. At each disk radius R_j, for each particle mass m_i, distribute the Monte Carlo particles in height z_u above the midplane according to the vertical number-density distribution $n_{d,i}(z)$ from the previous step. At $t = 0$, the distribution is Gaussian, following the background gas density profile.

3. Calculate μ_u and σ_u for each Monte Carlo particle u according to equations 2.63 and 2.64, replacing δt (collision timestep) with $\epsilon \times \delta t_{settle}$ (vertical motion fine timestep).

4. Draw an array of random numbers r_u of size N_s from a standard normal distribution. Update the particle heights as

$$z_{u,\text{new}} = z_u + \mu_u + r_u \sigma_u. \tag{3.13}$$

   Repeat for $1/\epsilon$ iterations.

5. Update number density corresponding to mass m_i for each cell following the fraction of N_s moved out of or received by any particular cell.

6. Repeat the process for each particle size with non-zero contribution to the total mass.

7. For each vertical cell, calculate the new particle mass histogram before moving on to the subsequent collision routine.

The vertical diffusion algorithm stated above, depends on the assumed strength of turbulence in the disk. We assume that MRI, which is subsonic in most parts of the disk and transonic only near the disk surface layers, is the main source of disk turbulence. Moreover, the proposed hydrodynamic turbulence mechanisms, such as vertical shear instability [Nelson et al., 2013], zombie vortex instability [Marcus et al., 2015], convective overstability [Lyra, 2014] and gravitational instability [Kratter and Lodato, 2016] produce turbulence with low strengths. To reflect this, we apply sonic cut-off in the Gaussian distribution of Δz: no particle may move a greater vertical

Table 3.1. Variables used in numerical algorithm

Variable	Meaning
N_H	number of bins in mass histogram
N	number of Monte Carlo particles used in each grid zone
m_i	mass at the center of i^{th} bin of mass histogram
N_i	number of particles from i^{th} bin of mass histogram
$n_{d,i}$	number density of particles in i^{th} bin of mass distribution
n_d	total dust number density including particles of all masses
f_i	fractional of particles in i^{th} bin of mass histogram
M_{total}	total dust mass in a grid cell
w_i	statistical weight of i^{th} bin of mass histogram
N_s	number of Monte Carlo particles used in settling
δt	dust evolution timestep
δt_{settle}	settling timestep
Δt	radiative transfer timestep

distance than $\Delta z = c_s \delta t_{settle}$. At the disk surface we adopt an outflow boundary condition so that particles that are turbulently stirred above the top of the grid are contained in a "ghost zone" and do not re-enter the grid. Our results are not affected by this assumption as the amount of mass lost to the ghost zone is several orders of magnitude less than the total dust mass. For dust particles in grid zones along the disk midplane we use a reflecting boundary condition. If a particular dust particles crosses the midplane and ends up at some $-z$, it is assumed that a dust particle of similar mass crosses the midplane from the bottom part of the disk and end up at a height $+z$.

3.5 Implementation in Code

The Monte Carlo method, along with the settling algorithm is implemented in a computer massively parallel computer program written in FORTRAN 95/03 along with a python wrapper for code compilation and user interface. The parallelization is implemented using MPI-FORTRAN. The python script reads a configuration file where the user enters the parameters for simulation setup and chooses the particular collision physics as intended. The code, as of now, can simulate a dust growth model that includes sticking, fragmentation, erosion and mass transfer. However, for all the studies presented in this dissertation, only sticking and fragmentation have been used as the possible outcomes of a binary collision. Below we present the key features of the code and their implementation.

3.5.1 General Workflow

In our Monte Carlo model, our code performs the simulations for dust growth, vertical settling and radial drift separately by exploiting the substantial differences between the time scales associated with each process. First, the total radial range is divided into n_r vertical columns and each vertical column is divided into n_z cells, creating a total of $n_r \times n_z$ cells for the full disk. Each cell in the disk is assigned two positional indices, one for the radial direction and one for the vertical direction. For example, a cell with positional indices c and d is the d^{th} cell in the c^{th} vertical column. The cell numbering in the vertical direction (the index d) at a particular column starts from the midplane and increases towards the disk surface. Following that, a certain number of processor (N_{proc}) is assigned for the simulations. It is important to note that N_{proc} can be any number less that $n_r n_z$ and greater than $\max[n_r, N_H]$, and is not limited by any other restriction. However, for more efficient use of the computational resource, N_{proc} is chosen to be equal to $\max[n_r, N_H]$ for reasons stated below. Each processor starts running the growth model at a particular cell, with the local dust and gas parameters provided, for a previously specified time scale.

Once the growth model is simulated for all the cells in the disk, n_r processors (processors with rank 0 to $n_r - 1$) are assigned to perform the vertical settling and diffusion, one for each column. The full information of dust size distribution for a particular column is then passed to the respective processor and the vertical dynamics is performed. For a single column, this operation is performed by a single processor. Upon completion, the information regarding the size distribution is again broadcast back to each cell pending further dust growth simulation.

3.5.2 The Flagged Parallelization Algorithm

A typical protoplanetary disk in our simulations ranges from $\sim$ 0.01 au to $\sim$ 80 au in the radial direction. As a result, the parameters affecting the dust growth timescales can vary significantly depending on the distance from the central star. For example, the gas density at 1 au and 80 au differ by six orders of magnitude, resulting into a difference of four orders of magnitude in maximum dust size at those locations. As the physical computation time is loosely proportional to the number of collision steps performed, time required for the dust growth simulations at different positions in the disk vary widely. As a result, it is possible that some processors, assigned to outer cells, finish their job early and sit idle, while processors responsible for cells in the inner disk are still at work. To minimize this leak in the computation resource, processors are assigned to a particular cell following a *flagged algorithm*. In this method, apart from two positional index, each cell is also assigned a *priority index* and a binary flag. First, a quick calculation is done to compute the approximate maximum particle size achievable in each cell and based on that, each cell is given a priority index, ranging from 0 to $n_r n_z - 1$. So, a cell with a lower priority index will spend more computation resource to complete the dust growth simulation. The binary flag for each cell can assume values of 0 or 1 depending on whether the simulation in that cell has been completed or not. A temporary file is maintained for each cell where the value of the flag is stored for the processors to look at, and all these files are removed from the system at the end of the full global simulation.

Following this initial setup, a particular processor first looks for all the cells where the value of the flag is 0. It then starts the simulation for the cell with the lowest priority index number (the maximum cost). Once the simulation in a particular cell is completed, the value of the flag is changed to 1 in the corresponding file in order to prevent any other processor to repeat the simulation in the same cell. In this way, the computation load is distributed evenly among all the processors and the computation efficiency is maximized.

3.5.3 The Modular Structure of the Code

Throughout the process of developing our code, we have been specially careful to design it in a user-friendly way so that any third party user can adapt the code and run it in a minimum possible way. To serve this purpose, our code has been written in a highly modular form. For the code setup, the user first needs to specify the dust collision physics s/he intends to implement. The options are chosen by modifying the file '*physics.conf*' file. The file looks as below:

```
[tablesize=2]
## CHOOSE THE PHYSICS YOU ARE INTENDED TO SIMULATE
## 'YES' or 'NO'

STICKING 'YES'
FRAGMENTATION 'YES'
BOUNCING 'NO'
MASS-TRANSFER 'NO'
EROSION 'NO'

VERTICAL-SETTLING 'YES'
TURB-DIFFUSION 'YES'

RADIAL-DRIFT 'YES'

VARIABLE-ALPHA 'NO'
```

Once the desired dust physics is chosen, the required parameters need to be specified in a separate file named '*configure.conf*'. A typical configuration file looks as

below:

```
#       INITIAL PARAMETERS FOR SIMULATION SETUP
#
# Inner Disk Radius (AU)
0.06

# Outer Disk radius (AU)
80.0

# Number of Monte Carlo Particles for each cell
60000

# Number of radial grids (n_r)
48

# Number of cells in each vertical column (n_z)
32

# Number of bins in mass histogram (N_h)
50

# Number of processors (N_proc)
64

# Type of gas surface density profile (power-law / self-similar)
"power-law"

# Value of Sigma_0: Will be read iff Surface density is given as
# power-law
1700.0

# Disk Mass (In Solar Mass): Will be used iff surface density profile
# is given as self-similar
0.02

### INFORMATIONS TO CREATE 'fragmentation.h' HEADER FILE
# Fragmentation Threshold Velocity (cm/s)
100.0

# Fragmentation criteria (velocity-dependent/target-mass)
# velocity-dependent: For Windmark et al 2012 criteria
# target-mass: For largest fragment=target mass
"target-mass"
```

```
# fragmentation power-law
1.833

# Size of smallest fragment (in micron)
0.1

### INFORMATIONS TO CREATE 'mass_transfer.h' HEADER FILE
# These inputs will be used iff mass-transfer is chosen in
# 'physics.conf' file
# User defined ratio of target mass to projectile mass
20.0

# Percentage of projectile mass to be transferred
10.0
```

Once this file is set by the user, a python script reads the configuration file, generates the initial input files for the simulations to start, and finally, compiles the code with the files opted by the user. The collision for icy bodies is not yet implemented in our code and implementing that is our plan for immediate future.

3.6 Code Test Results

As a test of our model, we now present our results and compare them with various results, already existing in the literature. In order to examine the fidelity of our model, we have tested our results against those obtained by both implicit integration [Windmark et al., 2012b] and Monte Carlo method [Drążkowska et al., 2014]. First, we have tested our model against the results of Windmark et al. [2012b] where a local dust growth simulation is presented with the exact same collision physics implemented. Then, we have tested our model for simulations in a full vertical column and compared the results with the ones from Drążkowska et al. [2014].

3.6.1 Comparison with Windmark et al. 2012(a)

We make a comparison test with the results from Windmark et al. [2012b] where a local simulation is performed with a sticking and fragmentation (SF) model

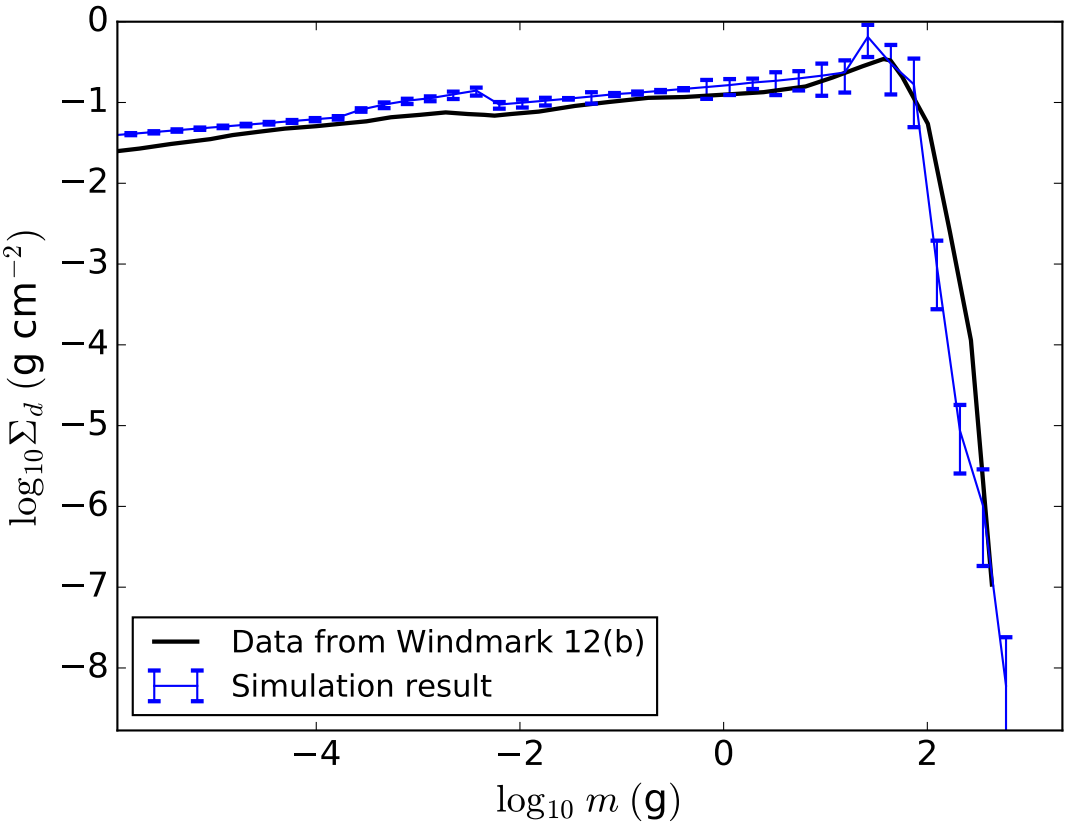

Figure 3.2: Local dust distribution steady state comparison with Windmark et al. [2012a]. Simulations are for an MMSN disk at radial position 1 au with $\Sigma = 1700$ g cm^{-2}, $\alpha = 10^{-4}$, $\rho_m = 1$ g cm^{-3}, $T = 280$K and dust to gas mass ratio 0.01. v_{frag} is taken as 100 cm s^{-1}. The solid black line shows the data electronically extracted from Windmark et al. [2012b] and the line with error bars shows the results from our simulation. The average of 10 simulations with 80000 particles each is plotted.

without any velocity distribution. The local dust growth simulation in this case has been performed at a radial distance of 1 au form the central star with an MMSN disk model. The surface density in this case is $\Sigma = 1700$ g cm^{-2} and the turbulence parameter $\alpha = 10^{-4}$. The temperature used in the simulation is 280 K with a material density of dust particles $\rho_m = 1$ g cm^{-3}. The fragmenting threshold velocity is taken as $v_{frag} = 100$ cm s-1. The data for comparison have been extracted electronically from figure 2, top panel of Windmark et al. [2012b]. As we can see from figure 3.2, our model shows an excellent match in the smaller mass range of the distribution and it deviates slightly in the higher end. In figure 3.2, the points in the extreme right miss the reference plot beyond the error bars which can be attributed to the bigger dynamical range obtained by introducing the weighing method.

3.6.2 Test for Settling and Diffusion Algorithm

Our vertical motion algorithm follows Charnoz et al. [2011]. In addition to settling and diffusion toward the density maximum, we give particles "kicks" in their z-coordinate (according to equations 2.63 and 2.64) to simulate a random walk caused by turbulent diffusion. In the absence of the settling term, the vertical motion of dust particles will be controlled only by the diffusion terms, both homogeneous and inhomogeneous. As a result, the dust distribution should follow the background gas density distribution, which is Gaussian. We have plotted our test results in figure 3.3, where the vertical dust density in plotted against the vertical height. The dashed black curve represents the vertical gas density stratification. We verify that our turbulent diffusion algorithm, with both homogeneous and inhomogeneous diffusion part, produces dust volume density $\rho_d(z)$ that matches our analytical description of $\rho_g(z)$, multiplied by a constant factor η (the abundance ratio). In Figure 3.4, we show that our results are independent of the choice of $\epsilon \times \delta t_{settle}$. As described before, we have adopted the position space approach to implement our vertical diffusion algorithm, for which the method converges well for our choice of δt_{settle}.

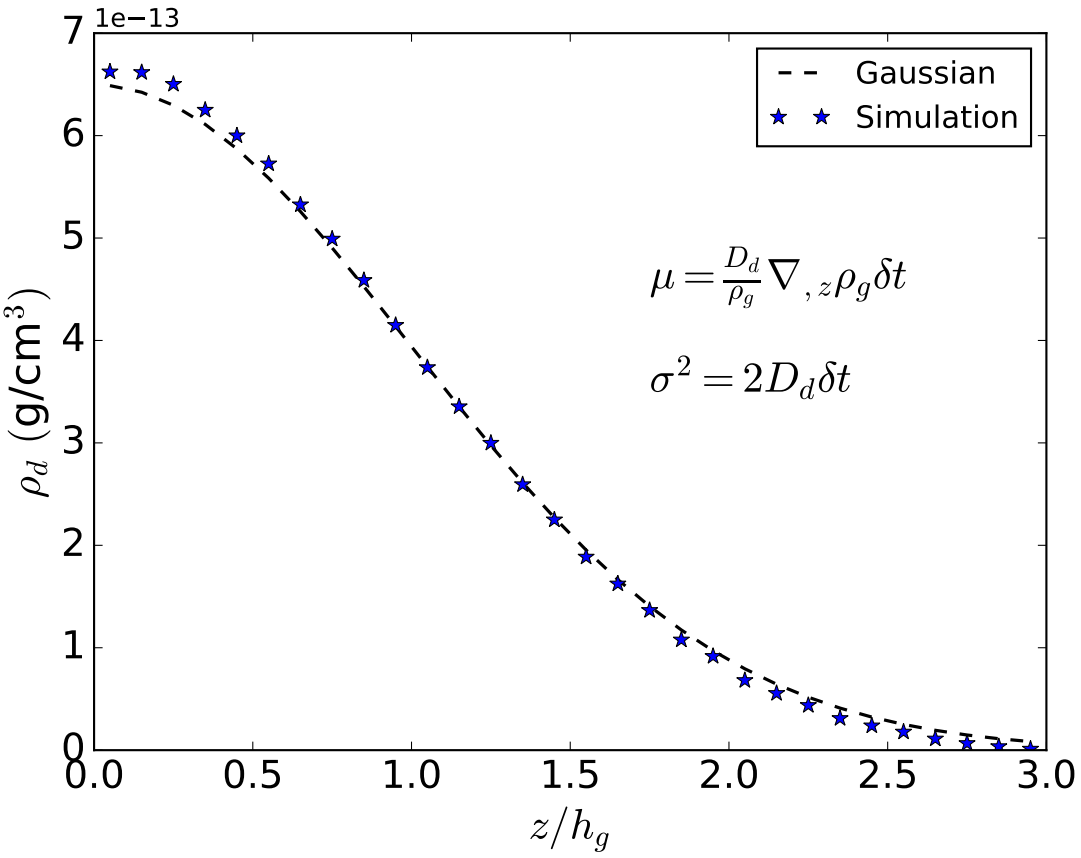

Figure 3.3: A plot of vertical density profile as a function of height expressed in terms of vertical scale height with only the turbulent diffusion terms present. The dust density distribution follows the background Gaussian gas distribution when the vertical settling term is ignored. The systematic velocity part contains only the force towards the density maximum (the inhomogeneous diffusion part) along with the stochastic turbulent stirring term (turbulent diffusion part). The solid curve is the Gaussian fit which represents the vertical stratification of background gas density. This plot ensures the proper working of our diffusion algorithm and its implementation in our code.

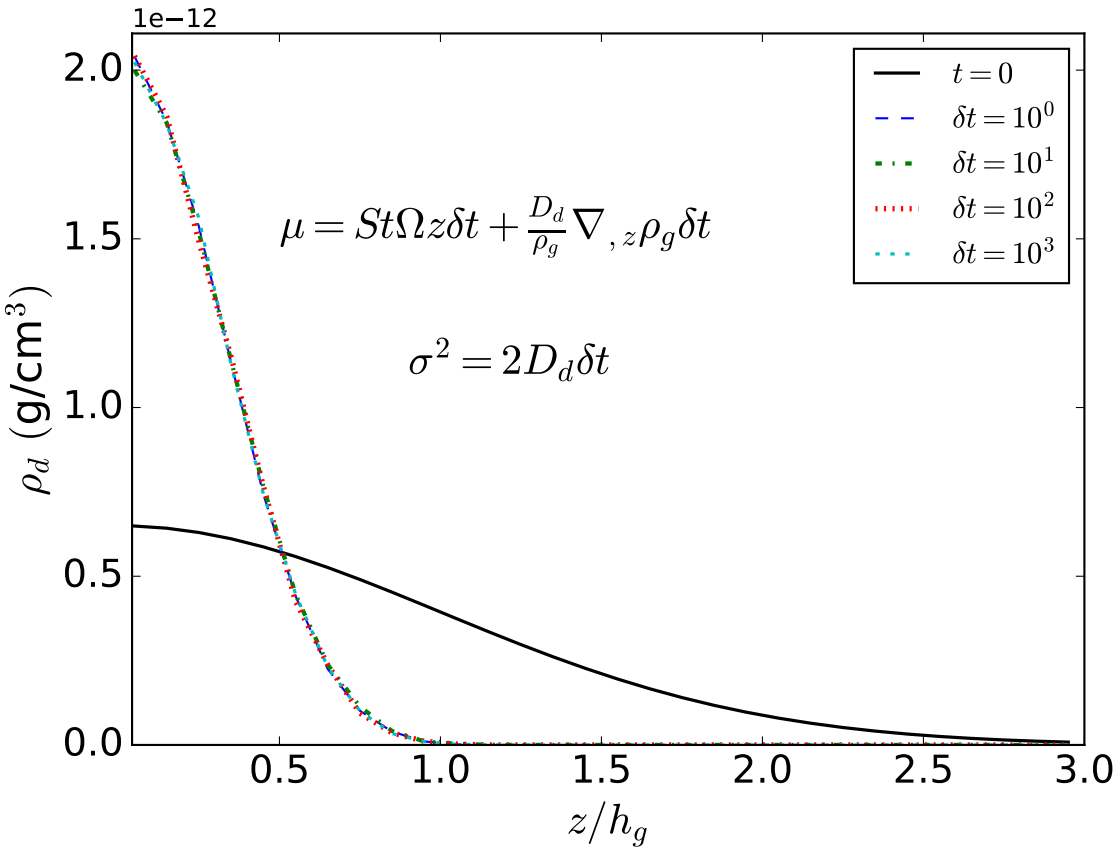

Figure 3.4: A test for convergence in vertical settling and diffusion timestep. As our model implements diffusion in position space, the results are largely independent of the time step dt_{settle} we choose for vertical dust dynamics. The black solid curve shows the initial dust distribution. The results after 10^4 years are plotted for different δt_{settle} normalized by 1 year. We find an excellent convergence in our settling and diffusion algorithm. As a result, the algorithm for vertical dust dynamics, which is otherwise computationally expensive, can be made more efficient by choosing a larger time step.

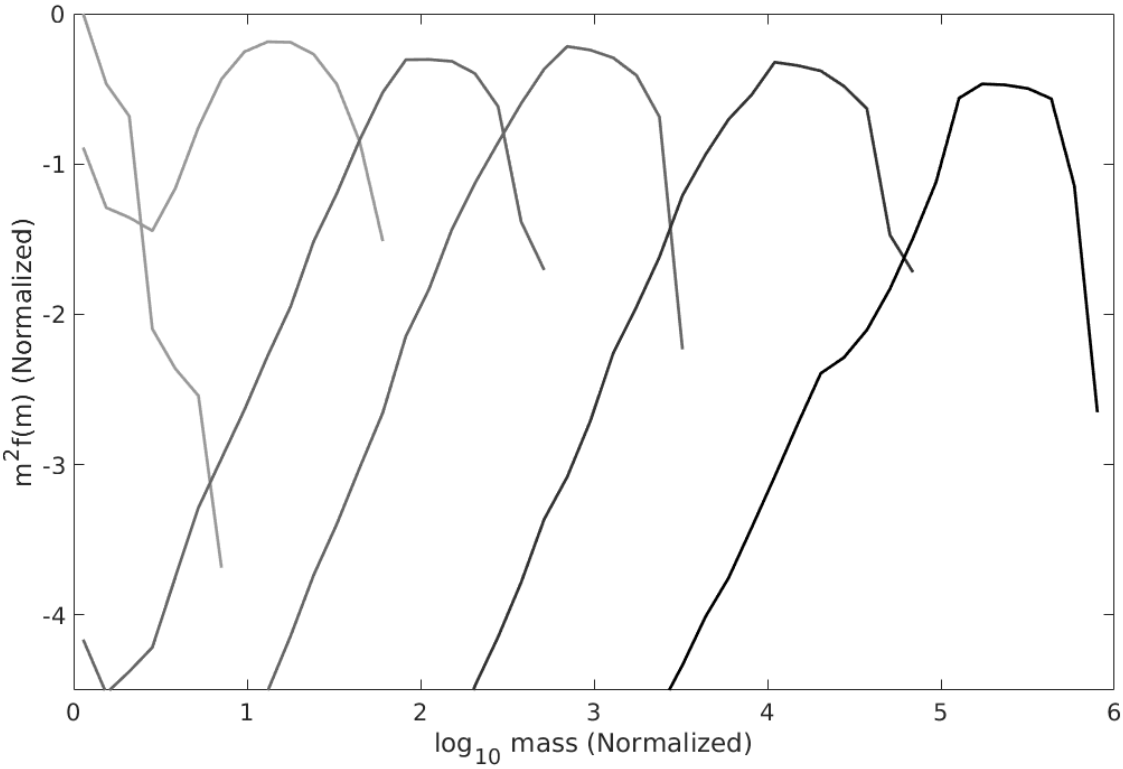

Figure 3.5: The evolution of dust distribution is tracked in a normalized mass scale. The plot shows (in gray scale) the evolution of $m^2 f(m)$ at normalized times 1, 10, 10^2, 10^3, 10^4 and 1.6×10^4. $f(m)$ here represents the dust mass distribution at any instant of time.

3.6.3 Vertical Dust Scale Height

Figure 3.6 compares our numerical calculations of the dust scale height with the analytical approximation given by Equation 2.67. The individual scale heights for dust particles, computed numerically, match perfectly well with the analytical calculation for dust size less than 1μm and greater than 1 mm. However, for size ranging from a few micron to a few hundred micron, the analytical results slightly overestimate the scale heights. The approach by Dubrulle et al. [1995] calculates the stokes number of dust particles using the midplane gas density and hence, assumes a higher coupling between dust and gas in the upper layers of the disk. This effect underestimates the efficiency of dust settling. In our numerical model, like Mulders and Dominik [2012], we find that calculating the Stokes number locally produces lower dust abundance at the disk surface. A similar effect is shown in figure 3.7 where the result from combined dust growth and settling simulation result for a vertical column at 5 au of an MMSN disk is shown. The steady state dust volume density normalized by their midplane value is plotted as a function of dust size a and vertical height. The value for α is chosen as 10^{-4}. As can be seen from the figure, the scale height for dust particles matches fairly well except for a less abundance in the upper layers of the disk.

3.6.4 Comparison with Drążkowska et al. 2014

We now present the size distributions computed by our model and compare them with models in the literature. In figure 3.8 we compare our steady state results for a 1-D vertical column with results from the paper of Drążkowska et al. [2014] for the same physical parameters. Our model includes sticking and fragmentation only, whereas the Drążkowska et al. [2014] model, in addition, includes mass transfer. However, Drążkowska et al. [2014] mentioned that panel 3 of their Figure 1 represents the vertically averaged steady state size distribution they would have achieved without mass transfer; it is this steady state that we plot in Figure 3.8. Once the distribution hits the fragmentation barrier growth is stalled unless mass transfer is included.

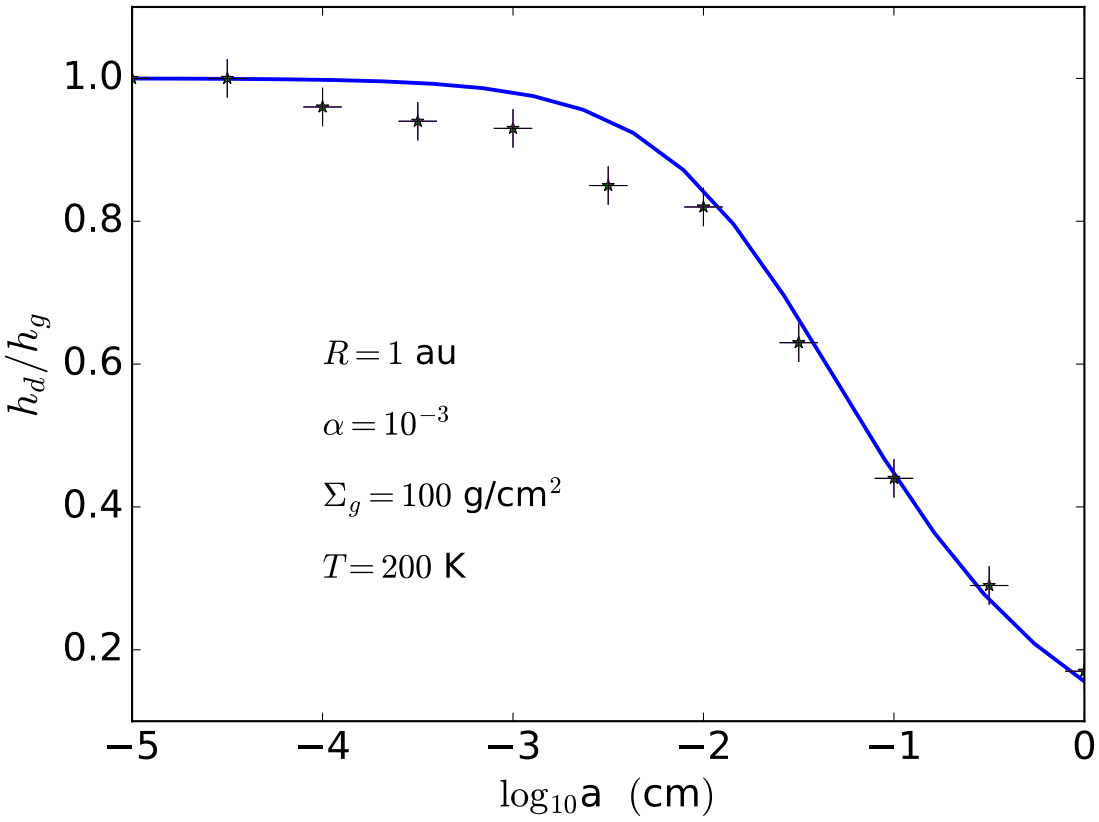

Figure 3.6: The blue solid line shows the analytical scale-height for a set of parameters listed on the figure. The scale heights for different particle sizes obtained from our settling/diffusion routine are also shown by + sign. For particles of sizes between 10 to 100μm, the scale height is slightly smaller than the ones predicted by the analytical solution, the result being consistent with the findings of Mulders and Dominik [2012].

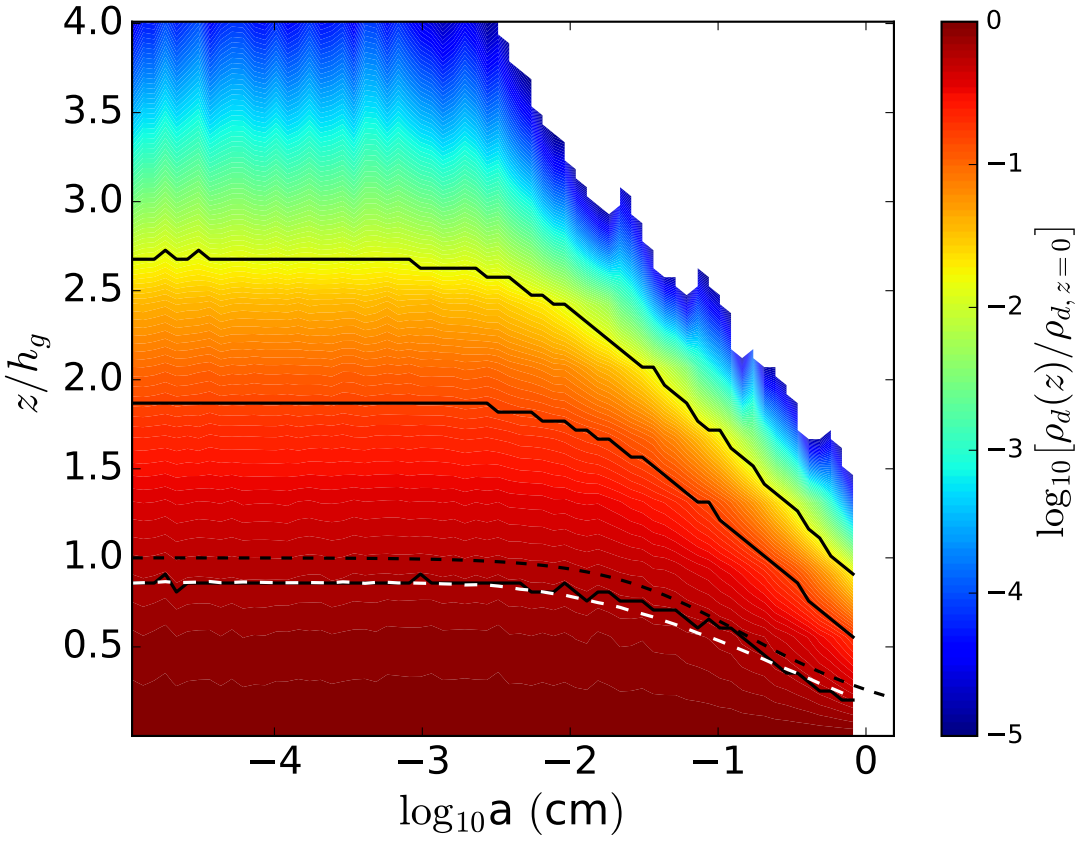

Figure 3.7: Steady state dust distribution for a vertical column at 5 au for an MMSN disk with $\alpha = 10^{-4}$, normalized by midplane value. The black dashed line shows the analytical dust scale height calculated using equation 2.67. The solid black lines, from bottom to top, show the heights where dust density becomes $1/\sqrt{e}$, $1/e^2$ and $1/e^{4.5}$ of its midplane value. The white dashed line represents the value $\sqrt{\langle z^2 \rangle}$ calculated for each dust size from the simulation data.

For this particular comparison test we have included a velocity distribution to calculate the collision velocity of dust particles. Considering the system is in collisional equilibrium, a *Maxwellian* velocity distribution is assumed as

$$f(v) = \sqrt{\frac{54}{\pi}} \frac{v^2}{v_{rms}^2} e^{-3v^2/2v_{rms}^2}. \tag{3.14}$$

[Windmark et al., 2012b], where v_{rms} is taken as the local relative velocity calculated using the formalism outlined in §2.3.2. The collision velocity is randomly drawn from this distribution using random numbers. See Appendix D for further details of the method adopted.

3.6.5 Maximum Particle Size Achieved

As a further code test, we compare the maximum particle radius a_{max} that our code produces with analytical estimates of a_{max} for the case in which relative velocities are dominated by turbulence. Initially, for tiny dust grains of micron and sub-micron sizes, the particle relative velocities are dominated by Brownian motion (figure 4.5) and collisional growth is efficient. When the particle size exceeds $\sim 100\mu$m gas turbulence becomes dominant in setting v_{rel}, until collisions between the largest particles reach the fragmenting threshold velocity, v_{frag}. Given that our collision model includes only sticking and fragmentation ("SF"), grain growth does not continue (but, see results from Drążkowska et al. [2014] on continued growth when mass transfer is included).

The largest eddy turnover time is $t_L \sim L/U_L$, where L is the largest scale of the inertial range and U_L is the characteristic velocity $\sqrt{\alpha}c_s$. Taking $L \sim \sqrt{\alpha}h_g$ [Schräpler and Henning, 2004], the largest eddy turnover time becomes $t_L \sim 1/\Omega$. Hence, for particles with stopping time of the same order as t_L the Stokes number is $St = t_L\Omega \sim 1$. On the other hand, the smallest eddy turnover time at the dissipation scale, t_η, is $t_\eta \sim Re^{-1/2}t_L$ [Kolmogorov, 1941], where Re, the Reynold's number, is the ratio of turbulent and molecular viscosity ν_T/ν_m [Ormel et al., 2007]. In all our simulations, the maximum particle size at disk midplane lies within the intermediate

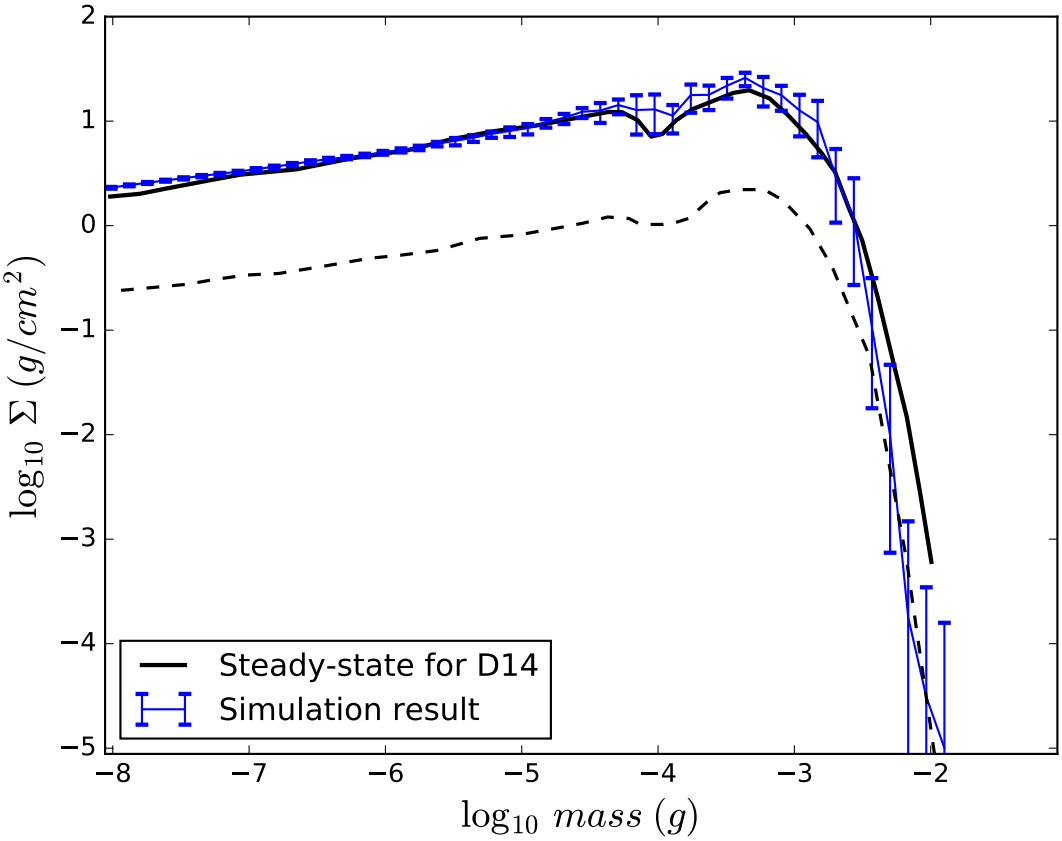

Figure 3.8: The steady state dust distribution for a MMEN model. The plot shows the vertically averaged dust surface density for a vertical column at 1 au with Σ = 9900 g cm^{-2}, α = 0.01, ρ_m = 1 g cm^{-3}, T = 280 K and a standard dust to gas mass ratio 0.01. v_{frag} is taken to be 50 cm s^{-1}. The solid black line shows the data electronically extracted from Drążkowska et al. [2014] and the line with error bars shows results from our simulations where the average from 10 runs with 80000 particles each is presented. For these simulations, the collision velocity is extracted from a Maxwellian velocity distribution where the relative velocity calculated from §2.3.2 is used as v_{rms}. The dashed black line is the same model, but with a fragmentation prescription exactly the same as [Windmark et al., 2012b] and the largest fragment is not set equal to the target (an offset by a factor of 10 is added for clarity). The proximity of this plot with the original blue plot indicates that the overall shape of the dust distribution is not sensitive to the fine details of fragmentation physics. The timescale for the steady-state, however, is $\sim$ 21 years compared to $\sim$ 16 years for the original test.

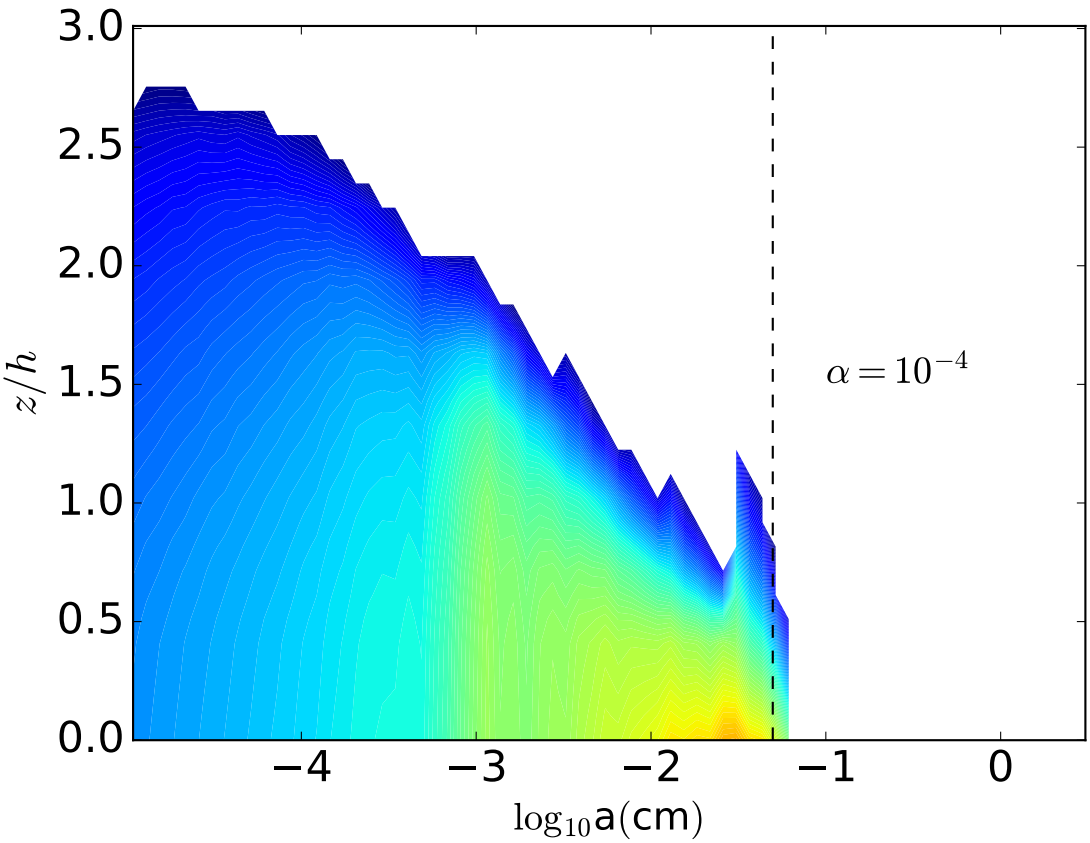

Figure 3.9: The figure shows the steady state dust size distribution for an MMSN disk model with full growth, settling and diffusion physics implemented. The vertical dashed black line corresponds to the maximum particle size estimated analytically by equation 3.16. Our simulation is in excellent agreement with the theoretically predicted value.

turbulent regime of Ormel and Cuzzi [2007, equation 28] where $t_\eta < t_{fric} < t_L$. Thus, following Birnstiel et al. [2011], the Stokes number for the largest particle is

$$St_{max} = \frac{v_{frag}^2}{2\alpha c_s^2}, \tag{3.15}$$

which corresponds to a maximum particle radius

$$a_{max} = \frac{v_{frag}^2 \rho_g}{2\alpha c_s \Omega \rho_m}. \tag{3.16}$$

Chapter 4

APPLICATION OF DUST MODEL I: OPACITY, THERMAL PROFILE AND GRAVITATIONAL INSTABILITY

4.1 Introduction

While most planets form "bottom-up" from dust particles accumulating into pebbles, planetesimals, and then solid cores [Lissauer and Stewart, 1993, Pollack et al., 1996, Morbidelli et al., 2012], some massive giant planets and brown dwarfs may form by top-down collapse in fragmenting protostellar disks [Kratter and Lodato, 2016, Boss, 1997]. Despite inferred low disk masses [Andrews et al., 2013, Ansdell et al., 2016, Pascucci et al., 2016] and stringent cooling requirements for fragmentation [Gammie, 2001, Boley et al., 2006, Stamatellos and Whitworth, 2008, 2009] observational evidence has been emerging that suggests some disks are gravitationally unstable [Kwon et al., 2011, Jin et al., 2016, Pérez et al., 2016, Tobin et al., 2016]. Furthermore, disk masses may be substantially underestimated due to the assumed value of the gas-to-dust ratio [Bergin et al., 2013, McClure et al., 2016, Miotello et al., 2017, Tsukamoto et al., 2017, Yu et al., 2017], and the companion mass-ratio distribution for B- and A-type primaries is separation-dependent, suggesting that close companions may originate in circumprimary disks rather than cloud core fragments [Gullikson et al., 2016]. Evidence that instability and fragmentation are taking place in at least a few astrophysical systems gives theorists a mandate to identify plausible ways to trigger them, at least in disks with high gas masses.

Disk cooling, which must occur on dynamical timescales for fragments to form [Gammie, 2001], is regulated by dust opacity [Cai et al., 2006, Boley et al., 2010, Cossins et al., 2010, Podolak et al., 2011, Lin and Kratter, 2016]. The odds of fragmentation increase when the disk becomes optically thin to its own thermal radiation,

allowing it to cool quickly [Meru and Bate, 2010]. Grain growth, which significantly lowers disk opacity, proceeds rapidly: even some Class 0 YSOs, which have ages under 200,000 years [Enoch et al., 2009], show some degree of dust growth via the core-shine effect [Steinacker et al., 2010, 2015], or have non-ISM spectral indices [Jørgensen et al., 2007, Ricci et al., 2010, Chiang et al., 2012]. As disks evolve, the largest observed (or inferred) grain sizes increase from millimeter in the Class-I phase [Miotello et al., 2014] to centimeter in the T-Tauri phase [Pérez et al., 2012, 2015, Tazzari et al., 2016]. Here we examine the extent to which grain growth alone—with no other triggers such as infall—can alter a disk's gravitational stability to axisymmetric perturbations. The effect of self-gravity in a protoplanetary disk is multifaceted. Apart from implications for planet formation, gravitational instability (GI) can contribute to angular momentum transport by producing turbulent stresses [Gammie, 2001, Baehr et al., 2017]. Our work thus also helps address the broader question of how dust can affect gas dynamics in disks. Also, we make a detailed study on how the disk opacity and temperature profile evolve as the grains grow and settle towards the midplane. It is expected that the monochromatic opacities in the longer wavelengths would increase as the total dust mass get transferred towards the bigger particles, while opacities for shorter wavelengths would decrease. So, it is important to know how these changes in opacities would affect the general disk physics and how they are affected by the choice of parameters in the dust growth model. In this chapter, we address these questions through a series of global simulations performed using our dust model described in chapter 3.

4.2 Global Simulations: Initial Conditions

In Figure 4.1, we present a schematic diagram of the general work-flow of our global simulations. Also, Figure 4.2 shows the general components of the full model that will be used for our science simulations. We now proceed to describe our disk models that are used for dust growth and settling calculations. All key quantities are summarized in Table 4.1. The central star is assumed to be a pre-main-sequence

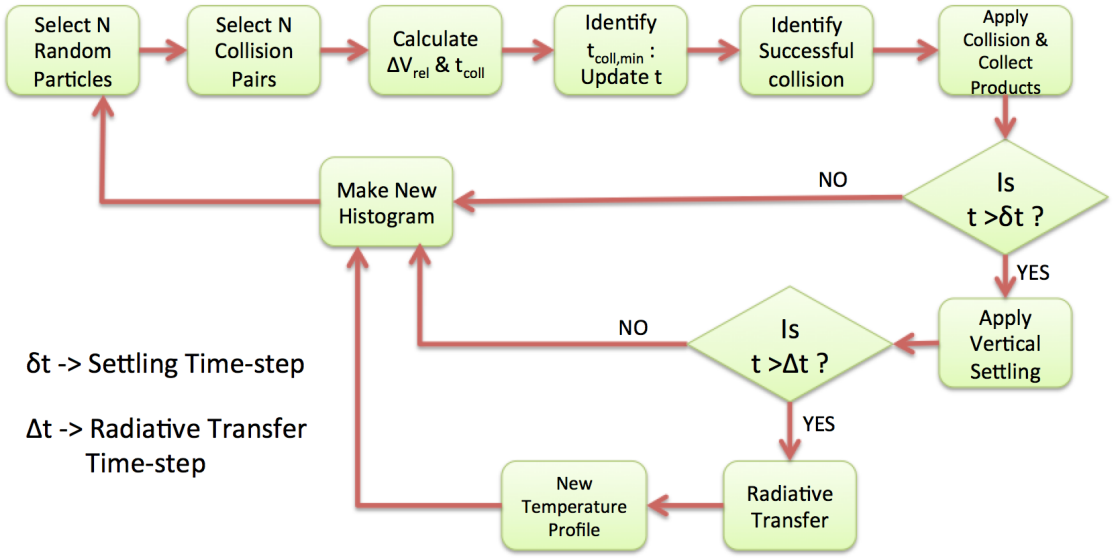

Figure 4.1: A pictorial depiction of the numerical algorithm implemented in this work. In this work, the gas density is held constant and we do not update the gas scale height of the disk through the course of our simulations.

Collisional Dust Growth	Turbulence Profile	Opacity	Radiative Transfer	Dynamics
1: Sticking 2: Fragmentation 3: Mass Transfer 4: Erosion	1: α Profile 2: Variable: (Ionization-Recombination Chemistry)	Utilitarian Opacity Model (Estrada et al 16) Wavelength Dependent Monochromatic Opacity	RADMC-3D Dust Continuum Radiative Transfer	1: Vertical Settling 2: Turbulent Diffusion 3: Radial Drift

Figure 4.2: A detailed structure of our code and its different components. The physics of erosion and mass-transfer are printed in red as these effects are not included in our science simulations. Also, radial drift is not included in the simulations presented in this chapter.

classical T-Tauri star with a mass $M_\star = 0.95 M_\odot$. In all our simulations, the disk is represented in a cylindrical coordinate system (R, ϕ, z) with R being the distance from the central star and z the height above the midplane. We assume that the disk is axisymmetric and vertically symmetric with respect to its midplane. We make a $1+1D$ disk model in (R, z) by decoupling the radial and vertical dimensions and simulating every vertical column independently. Here we do not perform gas evolution; the dust evolves against the background of a fixed gas disk with turbulent speeds specified analytically (§4.2.2). We assume that the gas and dust temperatures are equal, with the dust opacity regulating the thermal structure of the disk.

We are focused primarily on an accurate temperature structure, which plays a significant role in determining the Toomre-Q parameter, a measure of stability against self-gravity [Toomre, 1964]:

$$Q = \frac{c_s \Omega}{\pi G \Sigma_g}. \tag{4.1}$$

As we have already defined in chapter 2, in Equation 4.1, c_s is the local sound speed, Ω is the local angular frequency, and Σ_g is the gas surface density. The parameter Q is the measure of stability of the disk under self-gravity against thermal and shear effects. Theoretically $Q = 1$ is the exact threshold in the linear stability analysis for axisymmetric perturbations. However, for non-axisymmetric perturbations the critical value for Q is slightly higher than 1 and the instability gives rise to spiral modes instead of ring-like structure [e.g. Papaloizou and Savonije, 1991, Nelson, 1998, Mayer et al., 2002, Johnson and Gammie, 2003, Pickett et al., 2003]. Nelson [1998] reported the value of $Q = 1.5$ for the onset of spiral instabilities, while isothermal simulations by Johnson and Gammie [2003] achieved fragmentation at $Q = 1.4$. Similarly the SPH simulations by Mayer et al. [2002] find the growth of a two-armed mode until fragmentation takes place at $Q = 1.4$. In this paper we shall use the value 1.4 as the critical value of Q for which instability sets in. However, we caution that the disk's vertical thickness, which mimics a pressure term, may also provide support against self-gravity, lowering the threshold value to Q ~ 0.7 [Kratter and Lodato, 2016, Baehr

et al., 2017].

Two important assumptions of our model are:

1. Although the disk is turbulent and the turbulent speeds help determine the particle collision speeds, we do not include viscous heating: we assume that stellar illumination is the dominant heat source [e.g. Yu et al., 2016].

2. We assume no radial drift for dust particles. For the parameters we consider here, the radial drift timescale is long compared to the growth and settling timescales of dust grains.

4.2.1 The Gas Disk at $t = 0$

To construct our disk models at $t = 0$, we assume a power law temperature profile in the radial direction as

$$T(R) = 280 \times \left(\frac{R}{1 \text{ au}}\right)^{-1/2}. \tag{4.2}$$

We also assume that each vertical column is isothermal at $t = 0$. The isothermal assumption is used only to generate the initial setup; after the simulation is initiated, the temperature profile of the disk is governed by the evolving dust opacity. Assuming vertical hydrostatic equilibrium, the initial gas density profile is written as

$$\rho_g(R, z) = \rho_0(R)\, e^{-\left(z^2/2h_g^2\right)} \tag{4.3}$$

where $\rho_0(R) = \Sigma_g/\sqrt{2\pi}h$ is the midplane density and h_g is the local gas scale height, given by

$$h_g = c_s/\Omega, \tag{4.4}$$

where Ω is the Keplerian angular speed and $c_s = (k_b T/\mu m_p)^{1/2}$ is the local isothermal sound speed with k_b the Boltzmann constant, μ the mean molecular weight, taken as 2.33, and m_p the proton mass.

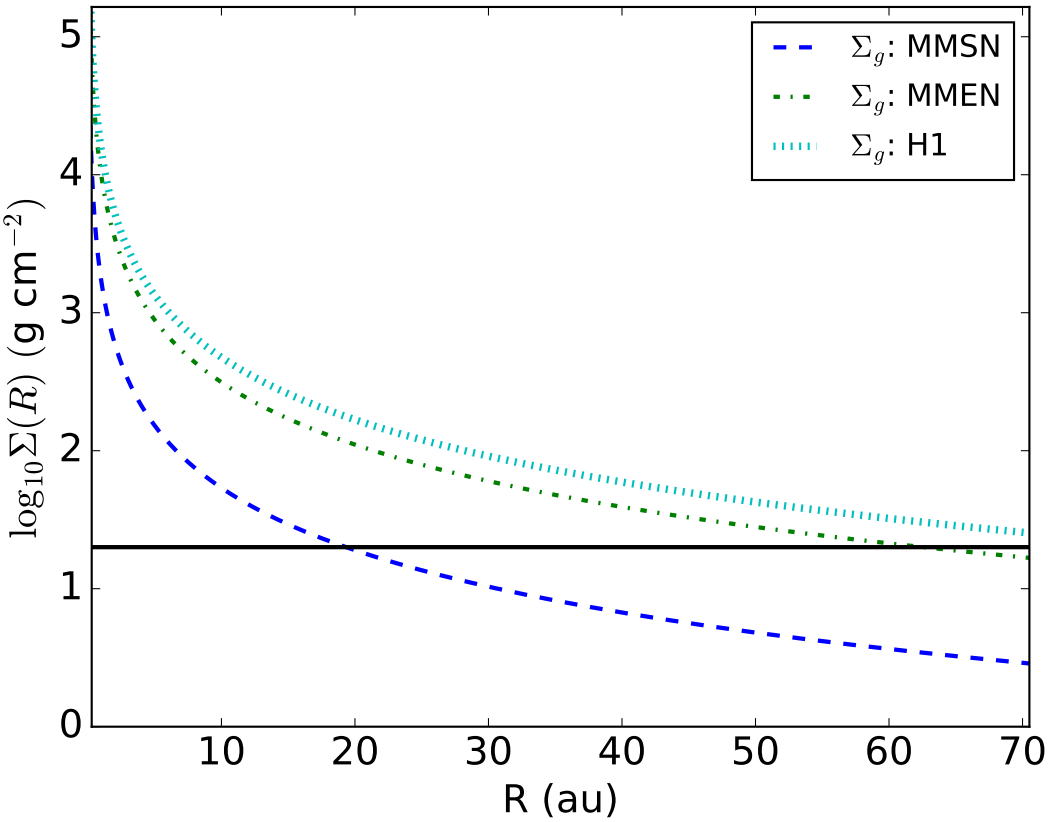

Figure 4.3: Surface density profile for the disk models: MMSN, MMEN and H1. The black horizontal line corresponds to $\Sigma_g = 20$ g cm^{-2} which is the surface density threshold at the outer edge of the dead-zone. As can be seen from the plot, the surface density is more than 20 g cm^{-2} out to ~ 65 au for the MMEN model. For H1 model the surface density is more than the threshold for the full radial extent of our simulations.

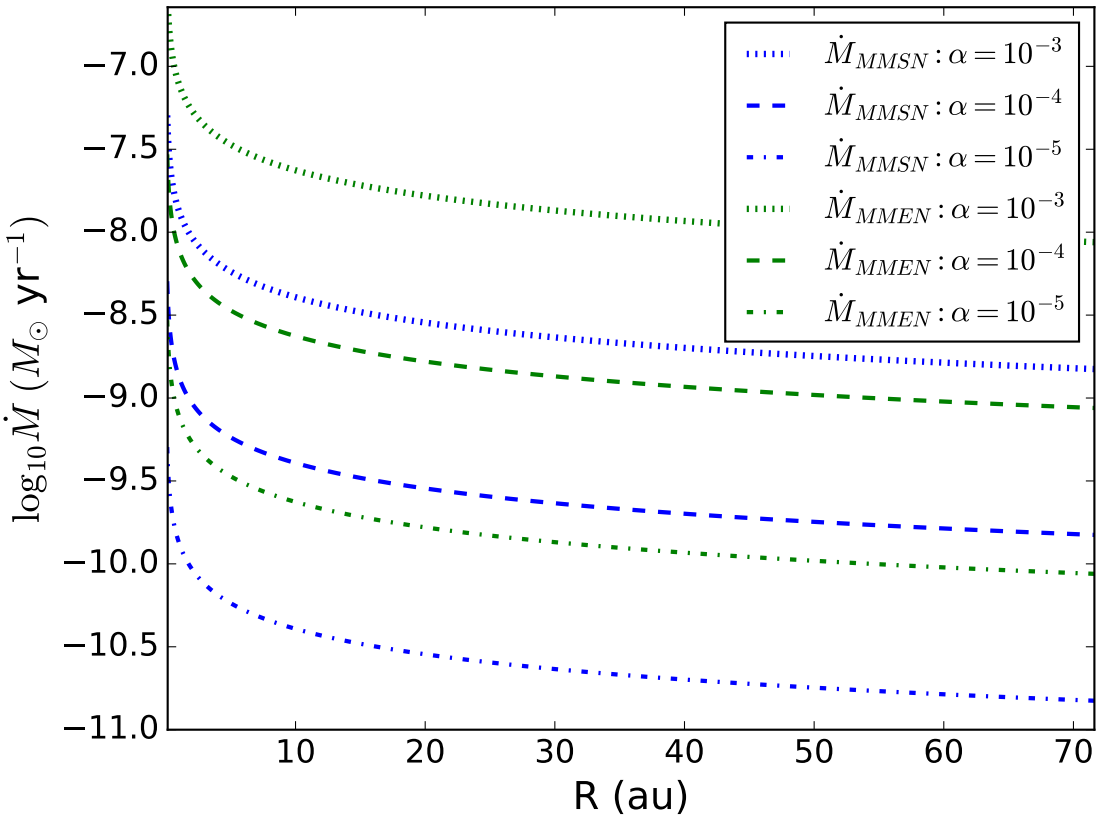

Figure 4.4: The mass accretion rates with constant $\alpha = 10^{-3}$, 10^{-4}, and 10^{-5} respectively for the MMSN (blue) and MMEN (green) disk models. The mass accretion rates, $\dot{M}$, with constant $\alpha = 10^{-3}$, 10^{-4}, and 10^{-5} respectively for MMSN (blue) and MMEN (green) disk models. $\dot{M}$ is calculated from the classical accretion theory.

We investigate the gravitational stability of two different disk models and use an additional model for code tests. The minimum-mass solar nebula [MMSN; Hayashi, 1981] is our test laboratory; we conducted simulations to compare with literature results, but mention *a priori* that grain growth and settling cannot trigger instability in the low-mass MMSN. For science simulations we adopt the minimum-mass extrasolar nebula [MMEN; Chiang and Laughlin, 2013], which is substantially heavier than the MMSN but has the same surface density power law index. The model surface densities are as follow:

$$\begin{aligned} \Sigma_g(R) &= 1.7 \times 10^3 \left(\tfrac{R}{1\text{au}}\right)^{-3/2} \text{g cm}^{-2} \quad \text{(MMSN)} \\ \Sigma_g(R) &= 10^4 \left(\tfrac{R}{1\text{au}}\right)^{-3/2} \text{g cm}^{-2} \quad \text{(MMEN)}, \end{aligned}$$

where $\Sigma_g(R)$ is the surface density at radius R (see Table 4.1 for variable definitions). Finally, we consider a heavy disk model which is only marginally stable at $t = 0$ with the surface density profile

$$\Sigma_g(R) \sim 1.5 \times 10^4 \left(\frac{R}{1\text{au}}\right)^{-3/2} \text{g cm}^{-2}. \tag{4.5}$$

In the following, test simulations of the MMSN are identified by 'T' and those of the MMEN by 'F' (see Table 4.1, which lists the simulations performed in this paper). The heavy disk model is named H1. The surface density profiles ($\Sigma_g(R)$) for all disk models are shown in the figure 4.3. We simulate a radial range of $R_{min} = 0.1$ au to $R_{max} = 75$ au. With such radial extent, the disk masses are approximately 0.018, 0.12 and 0.18 $M_\odot$ for MMSN, MMEN and H1 respectively. In the vertical direction, we extend the grid to $4h_g$ above the midplane in each radial grid zone; we ignore regions with $z > 4h_g$ as dust density above that height is less than 0.1% of that in the midplane even at $t = 0$. The 40 radial zones are equispaced in $\log(R)$, and function independently: particles do not move between vertical columns due to the omission of radial drift. We divide each column into 32 cells equispaced in z, 8 cells

Table 4.1. Simulations Performed

Simulation Name	$\Sigma(R)$ profile	α	v_{frag} cm s^{-2}	$M_{disk}/M_{\star}$	α_{min}
T1[a]	MMSN	10^{-3}	100	0.018	···
T2[a]	MMSN	10^{-4}	100	0.018	···
T3[a]	MMSN	10^{-5}	100	0.018	···
T4[a]	MMSN	variable	100	0.018	10^{-5}
F1	MMEN	10^{-3}	50	0.12	···
F2	MMEN	10^{-4}	50	0.12	···
F3	MMEN	10^{-5}	50	0.12	···
F4	MMEN	10^{-3}	100	0.12	···
F5	MMEN	10^{-4}	100	0.12	···
F6	MMEN	10^{-5}	100	0.12	···
F7	MMEN	variable	100	0.12	10^{-5}
F8	MMEN	variable	100	0.12	10^{-4}
H1	equation 4.5	variable	100	0.18	10^{-5}

Note. — Science simulation set: Two different disk surface density profiles with $\alpha = 10^{-3}$, 10^{-4}, 10^{-5} and variable.

[a]Code test

per scale height. The typical mass accretion rates ($\dot{M}$) for MMSN and MMEN models, calculated according to the classical accretion theory [Hartmann et al., 1998], are also shown in figure 4.4.

4.2.2 Turbulence Profile (α): Ionization-Recombination Chemistry

It is believed that a protoplanetary nebula is turbulent due to several proposed hydrodynamic [Lovelace et al., 1999, Lyra, 2014, Nelson et al., 2013, Marcus et al., 2015] and magneto-hydrodynamic [Balbus and Hawley, 1991, Turner et al., 2014] instabilities. However, we assume that the magnetorotational instability (MRI) is the source of turbulence in all our disk models. For our first set of simulations (T1, T2, T3, and F1 - F6) we adopt the spatially uniform α viscosity prescription [Shakura and Sunyaev,

1973]

$$\nu = \alpha c_s h_g, \tag{4.6}$$

where ν is the turbulent viscosity. For simulations with variable $\alpha(R, z)$ (T4, F7, F8 and H1), we simulate a disk with layered accretion [e.g. Gammie, 1996]. MHD turbulence depends on how the gas is coupled to the magnetic field, which strongly depends on the degree of ionization. For simulations with variable α, we adopt the ionization prescription of Landry et al. [2013], who consider cosmic rays, stellar X-rays and radionuclides as the ionization sources. The model first calculates the equilibrium abundances of charged species by solving a simplified set of chemical reactions, including grain surface reactions and the metal atoms' adsorption and desorption on the grains, adopted from Ilgner and Nelson [2006]. In the regime where recombination mostly occurs on the grain surface, the simplified model gives similar results to a detailed chemical model. Subsequently, the Ohmic (η_O) and ambipolar (η_A) diffusivities are calculated and $\alpha(R, z)$ is computed. The minimum turbulent efficiency, α_{min}, due to large scale fields in the dead zone, is taken as 10^{-5} [Turner et al., 2007]. For details of how we compute the spatially non-uniform α profile see appendix E. We note that hydrodynamic instabilities can provide viscosity even in magnetically inactive regions [Lyra, 2014, Nelson et al., 2013]. These instabilities can maintain a higher value of α which will affect the global dust evolution in the disk. To test how higher $\alpha_{\rm min}$ affects the size distribution, we have chosen one model (F8) with a minimum value for $\alpha = 10^{-4}$ at the midplane.

Table 4.2. Variables used in theoretical modeling

Variable	Meaning
c_s	local isothermal sound speed
Σ_g	gas surface density
κ	epicyclic frequency
Ω	Keplerian frequency
R	orbital distance from central star
α	turbulence strength
$M_\star$	stellar mass (mass of central star)
ρ_g	gas volume density
ρ_d	dust volume density
ρ_m	material density of dust
n_0	Dust number density at midplane at $t = 0$
h_g	local gas pressure scale height
h_d	dust scale height
a	radius of dust particles
η	dust to gas mass ratio
t_{fric}	friction/stopping time
v_{rel}	relative velocity of collision
v_{frag}	fragmentation threshold velocity
v_{dm}	relative speed of dust grains and gas molecules
V_g	gas dispersion velocity

Table 4.2 (cont'd)

Variable	Meaning
λ_{mfp}	mean free path
St	Stokes number
ξ	fragmentation power law index
D_g	gas diffusion coefficient
D_d	dust diffusion coefficient
κ_λ	monochromatic opacity
$\langle\kappa\rangle_{\rho_d}$	density weighted opacity
t_η	smallest eddy turnover time
t_L	largest eddy turnover time
Re	Reynolds number
λ	wavelength of photon radiation

After the initial calculation of turbulence efficiencies, we do not evolve the $\alpha(R, z)$ profile with time in the course of our simulations. The initial prescription from Landry et al. [2013] assumes a nominal 1µm grain size. Due to grain growth and settling, the gas-to-solid ratio decreases at the midplane by almost an order of magnitude from its initial value. This evolving gas-to-solid ratio would alter the height of the dead-zone above the midplane as the disk evolves. Okuzumi and Hirose [2012] confirmed this trend with their grain evolution model in which the dead-zone initially shrinks, with its upper boundary contracting towards the midplane, and then extends vertically again. We note that for a self-consistent treatment, varying $\alpha(R, z)$ and hence the thickness of the dead-zone would be necessary. We leave the improved $\alpha(R, z)$ prescription for future work.

4.2.3 Dust Disk at $t = 0$

To model the dust size distribution at $t = 0$, we adopt a grain-size distribution with an MRN [Mathis et al., 1977] power-law index, $N(a) \propto a^{-3.5}$ where $N(a)\,da$ is the number of dust particles of radii between $[a, a + da]$. We consider that dust grains

already grow beyond the ISM size in the molecular cloud phase [Suttner and Yorke, 2001] and adopt the maximum and minimum sizes of the dust size distribution at $t = 0$ as $a_{max} = 1.0\mu$m and $a_{min} = 0.1\mu$m. To begin our grain growth and settling simulation, we make two assumptions:

1. Gas and dust of all sizes are dynamically coupled and well mixed at $t = 0$, with $St_{t=0} \ll 1$ (this will not be true at later times);

2. The dust-to-gas mass ratio is $\eta = 0.01$, similar to the interstellar medium (ISM).

In the strongly coupled dust assumption, the initial dust scale height can be well approximated by the gas scale height (equation 2.67). Also, we can assume that the dust will follow the exact same Gaussian stratification as the background gas. We estimate the total dust mass and vertical dust density stratification in a particular column from the knowledge of surface density as $M_{dust} = \eta\ \Sigma(R)$. Also,

$$M_{dust} = \int_{a_{min}}^{a_{max}} \frac{4}{3}\pi a^3 \rho_m \frac{dN}{da}\, da = \eta\Sigma(R) \tag{4.7}$$

and the total number of particles N in the vertical column can be written as,

$$N = \int_{a_{min}}^{a_{max}} \frac{dN}{da}\, da = A \int_{a_{min}}^{a_{max}} a^{-3.5}\, da \tag{4.8}$$

$$= \frac{2}{5} A \left[(a_{min})^{-5/2} - (a_{max})^{-5/2} \right] \tag{4.9}$$

where A is the pre-factor of MRN particle size distribution and can be obtained from equation 4.7,

$$A = \frac{M_{dust}}{\frac{8}{3}\pi\rho_m(\sqrt{a_{max}} - \sqrt{a_{min}})} \tag{4.10}$$

The assumed Gaussian profile of dust number density in the z direction gives

$$N = \int n(z)\, dz = n_0 \int_0^\infty e^{-z^2/h_d^2}\, dz = n_0 \int_0^\infty e^{-z^2/h_g^2}\, dz \tag{4.11}$$

where $n(z)$ is dust number density with n_0 being that in the midplane. Equation 4.11 gives

$$n_0 = \frac{N}{\sqrt{2\pi} h_g} \tag{4.12}$$

After the calculation of n_0, the initial dust size distribution is then computed, following a Gaussian, for the full vertical column.

4.2.4 Relative velocity of Collision

We consider five different contributions to the particle relative velocity (see figure 4.5): Brownian motion (δv_B), turbulent motion (δv_t), vertical settling (δv_z), radial drift (δv_r) and azimuthal motion (δv_ϕ). Our simulations are azimuthally symmetric and we do not allow particles to move between radial grid zones. However, we include δv_r and δv_ϕ contributions to v_{rel} to improve the accuracy of our collision outcomes. Although it may seem physically inconsistent to include δv_r in the velocity calculation while forbidding radial motion in our grid, δv_r and δv_ϕ contribute significantly to collision velocities only for $a \geqslant 10$ cm as demonstrated by Estrada et al. [2016]. The presence of such large dust particles is rare in our simulations, and radial drift is important over a timescale much larger than a time when we obtain steady states for the dust size distribution. The relative velocity of collision is calculated as

$$v_{rel} = \sqrt{\sum \delta v_i^2}, \tag{4.13}$$

where i represents each of the five velocity contributions mentioned above.

For the smallest particles, Brownian motion is the dominant contribution to v_{rel}, giving $\delta v_B = \sqrt{[8kT(m_p + m_t)/(\pi m_p m_t)]}$ (where k is the Boltzmann constant). The collision velocities of dust particles with radii greater than a few μm are dominated by the gas turbulence. To calculate δv_t, we follow the closed-form velocity prescription of Ormel and Cuzzi [2007] (their equations 26, 28 and 29). §3.4 describes our algorithm for computing δv_z. We compute δv_r and δv_ϕ using equations 6, 7, and 18 of Okuzumi and Hirose [2012].

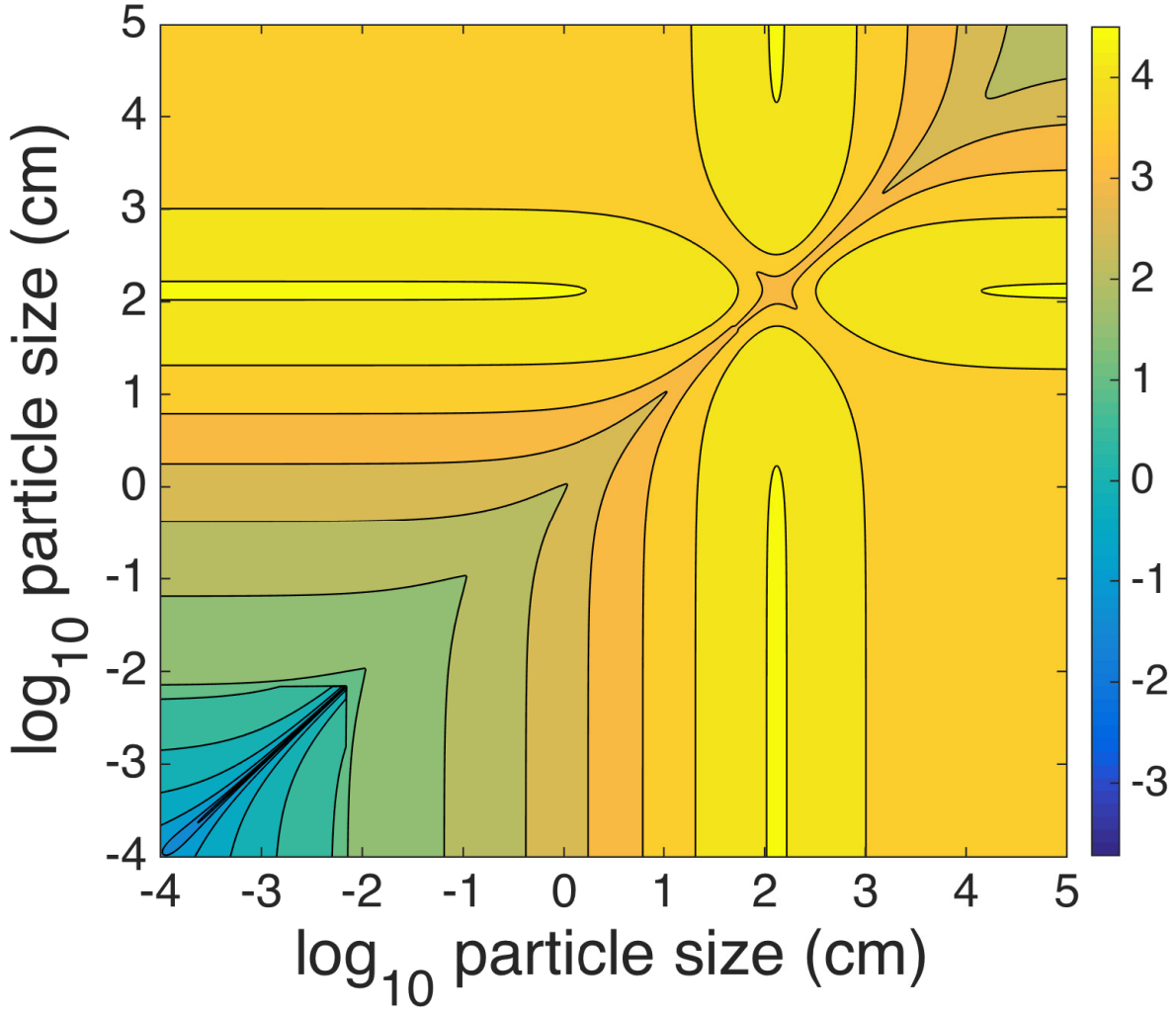

Figure 4.5: The relative velocity between different particle sizes in log scale in the unit of cm s^{-1} (equation 4.13) with contributions from Brownian motion, turbulence, settling, radial and azimuthal drift as mentioned in section 2.3.2. The velocity profile is plotted for $\Sigma_g = 330$ g cm^{-2}, $\eta = 0.01$, $T = 115$K, and $\alpha = 10^{-3}$ at a distance of 3 au from the central star. Parameters listed above are directly taken from Windmark et al. [2012a]; see their Figure 6.

4.2.5 Collision Outcomes: Sticking & Fragmentation

We treat dust collisions as a binary process, identifying the smaller mass as the projectile (m_p) and the bigger mass as the target (m_t). The collision outcome is determined by the relative velocity (see §2.3.2 for a description of our velocity computation). For all our science simulations, we have restricted our collision model to sticking and fragmentation (SF) only. If the particles collide with a velocity less than a threshold velocity v_{frag}, they stick and form a new particle with mass $m_{final} = m_p + m_t$. When $v_{rel} > v_{frag}$, the collision results in fragmentation. For such an event the combined mass of the target and the projectile is made to follow a mass distribution $f(m)\,dm \propto m^{-\xi}\,dm$ with ξ being the fragmentation distribution power law index. Here we adopt $\xi = 11/6$ [Windmark et al., 2012b, Drążkowska et al., 2014, Krijt and Ciesla, 2016], though we note that some experiments predict a shallower fragment size distribution with $\xi = 9/8$ [Blum and Wurm, 2000, Güttler et al., 2010]. The smallest fragments are monomers of 0.1µm. The largest body in the fragment mass distribution is set equal to the target mass as in Drążkowska et al. [2014] (personal communication).

We note that setting the mass of the largest particle of the fragmenting distribution equal to that of the target is equivalent to assuming that the target is immune to fragmentation. Laboratory experiments, in fact, show that the mass of the largest fragment is dependent on the collision velocity [Güttler et al., 2010]. We, however, have found that the overall shape of the steady state size distribution is not very sensitive to the fine details of the fragmentation prescription. The abundance of the small grains, originating from the fragmentation of bigger dust particles, is rather dependent more on the power-law index of the fragment's size distribution, in agreement with the analytical treatment of Birnstiel et al. [2011]. In Figure 3.8, we have presented the test results with two different fragmentation prescriptions and the results are very similar. However, the timescale for reaching the steady state differs by a few years between these two results.

Regarding other collisional outcomes, which we have neglected for our science simulations, inclusion of bouncing in the model slows down the growth process and

the growth timescale may even become comparable to the timescale for radial drift [Estrada et al., 2016], which is not included in our model yet. Furthermore, bouncing effect restricts the growth of particles [Windmark et al., 2012a] limiting the maximum *Stokes* number of the evolving size distribution [See figure 2 of Estrada et al., 2016]. Inclusion of mass transfer helps dust particles to grow indefinitely and is considered a possible pathway to planetesimal formation [Drążkowska et al., 2013] if drift is neglected. Estrada et al. [2016], on the other hand, have shown that under more realistic conditions where radial drift is included, the effect of mass-transfer is limited. The primary objective of this work is to examine how the disk's temperature profile responds to grain growth and settling. Given that grains of size similar to the peak wavelengths of star and disk emission control the temperature structure, we do not include the mass transfer/planetesimal formation pathway in this paper. Furthermore, although target erosion is the most likely outcome of high-speed collisions between particles of significantly different masses [e.g. Windmark et al., 2012a], we neglect erosion due to computational constraints. Instead, we assume that all collisions with $v_{rel} > v_{frag}$ lead to fragmentation, as in the "SF" simulations of Windmark et al. [2012b]. We also assume that the dust particles remain compact spheres throughout their growth and fragmentation.

4.3 Opacity Model

After computing the dust number density $n(a, R, z)$, we require an opacity prescription to find the disk temperature $T(r, z)$. For the majority of the disk mass, which lies near the midplane, it is reasonable to assume that the gas and dust temperatures are equal. For temperatures less than $\sim$ 2000 K, dust is the dominant opacity source [e.g. Kama et al., 2009], so we neglect the opacity of gas to opacities. We adopt the "Utilitarian opacity model" from Cuzzi et al. [2014] (See section F for a brief description of the model) to calculate the extinction efficiencies $Q(\lambda, a)$ as a function of wavelength and dust size. Following the calculation of extinction efficiency, the opacity per gram

of dust is calculated as

$$\kappa_\lambda(a) = \frac{3}{4} Q(\lambda, a) \frac{1}{a\rho_m}. \tag{4.14}$$

We assume that the composition of dust particles is 100% astronomical silicate, $[Fe_xMg_{1-x}]SiO_3$ with $x = 0.3$, and has a material density $\rho_m = 3.4$ g cm^{-3}. The real and imaginary refractive indices are taken directly from the MPIA website[1]. The reader is advised to look into Cuzzi et al. [2014] for further details of the model. See figure 4.6 for the dust opacities calculated using C14 and adopted in radiative transfer calculations.

4.4 Temperature Calculation: Radiative Transfer

We compute the temperature profile of the disk using RADMC-2D [Dullemond and Dominik, 2004]. The code performs Monte-Carlo dust continuum radiative transfer based on the method of Bjorkman and Wood [2001] with modifications to produce smoother results with a reasonable number of photons. The working principle of this code involves dividing the luminosity of the source into a finite but large enough number of photon packets, each with the same amount of energy. However, the number of physical photons, actually contained by each packet, depends on the frequency. After a photon packet is injected into the disk with an assigned random frequency chosen from the spectral energy distribution of the central star, the code follows the packet through absorption and scattering by dust grains. The photons once absorbed by the dust get re-emitted immediately with frequencies randomly chosen from the difference between the thermal spectra before and after the packet is absorbed. This process continues until the photon escapes from the disk through its physical boundary. The increase in temperature of the cell, where absorption/re-emission or scattering takes place, is computed after each event. The frequency of the incident photon and the dust opacity at that frequency are used for temperature re-calculation.

[1] https://www2.mpia-hd.mpg.de/home/henning/Dust_opacities/Opacities/opacities.html

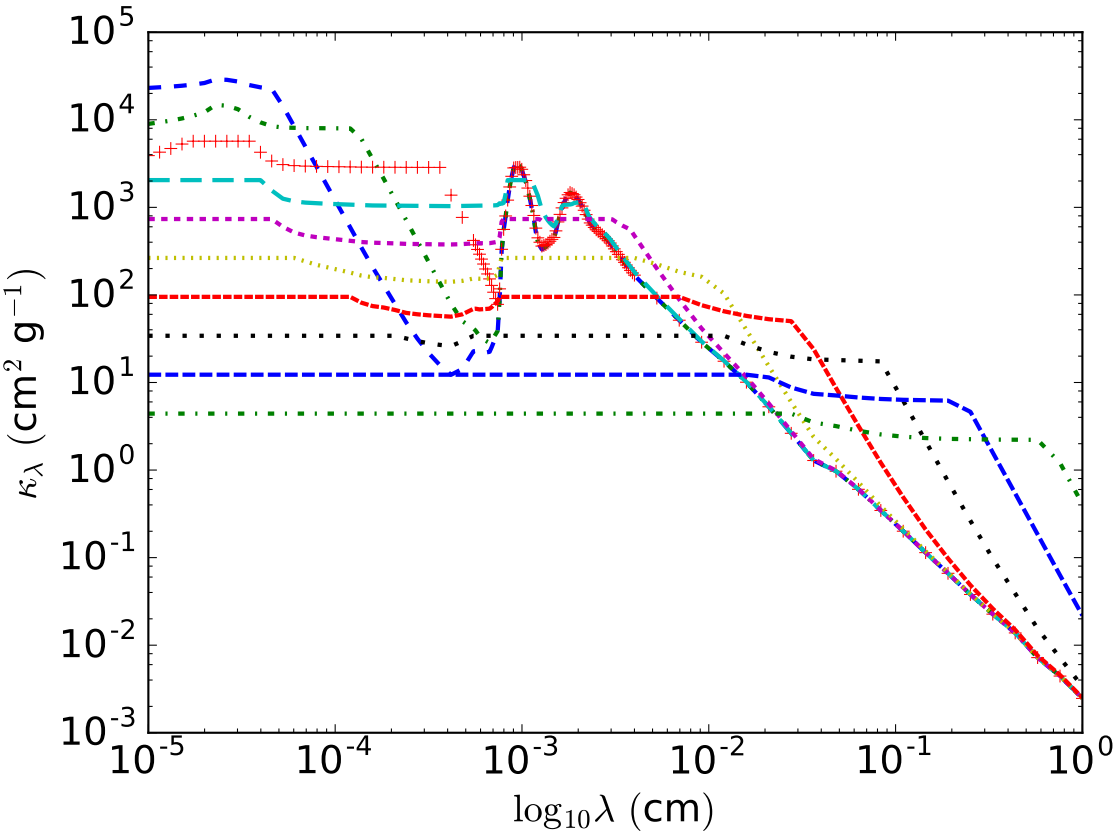

Figure 4.6: Opacity as a function of wavelength for 100% silicate grains. The opacities shown are for dust sizes between 0.1 μm to 1 mm, from top to bottom, equi-spaced in log scale. The ratio of the particle diameters between any two successive lines in the figure is 2.78.

To use the code, we treat dust of each size of our histogram as separate species and provide RADMC the monochromatic absorption and scattering opacity *per gram of dust* calculated using equation 4.14. Based on convergence tests, we find that we achieve an accurate temperature profile using 10^6 photon packets.

Note that the vertical temperature structure at a particular column at $t = 0$ obtained from RADMC is different than the canonical power-law temperature profile given by Equation 4.2, which assumes the vertical column to be isothermal. We have used the isothermal prescription to define the initial gas scale height h_g which remains the same throughout the simulation as the dust physics is implemented on a fixed gas background.This implies that our steady state solutions are not in hydrostatic equilibrium. The disk interior is cooler than the initial stage, so restoring vertical force balance would make the disk even thinner.

4.5 RESULTS

We now move on to present the results of our dust growth, settling, and turbulent diffusion simulations in this section. We first report the steady state timescales of our simulations in §4.5.1 followed by general results for evolving dust size distribution as a function of disk parameters in Sections 4.5.2 to 4.5.5. In section 4.5.6, we present our results for evolving disk opacity, temperature profile and gravitational stability under axisymmetric perturbations.

4.5.1 Steady State Timescales

For a given disk mass, the time to reach a steady state increases with v_{frag} and decreases as the value of α increases. In all simulations the final steady state is reached within $\sim 3 \times 10^4$ years. For example, for the MMEN model, the timescales of the results shown for disk with $\alpha = 10^{-3}$, 10^{-4} and 10^{-5}, and $v_{frag} = 50$ cm s^{-1} are $\sim 23,000$, $27,000$ and $29,000$ years, respectively. However, the growth and vertical diffusion timescales are shorter than the timescales through which the simulations are run. For example, the maximum particle size is achieved in the MMSN model at 10 au

with $\alpha = 10^{-5}$ within $\sim$ 2500 years. When α is increased, the growth process is affected in two ways. First, the relative velocity of collisions increases due to increased turbulence strength, reaching v_{frag} faster and restricting the growth. Secondly, the collision timescale decreases due to increased collision velocity ($\tau_c \sim 1/n\sigma v_{rel}$). Both these effects reduce the time required to reach the maximum grain size. As an example, the growth timescale for the same MMSN model at 10 au is $\sim$ 2200 years for $\alpha = 10^{-4}$, and $\sim$ 1600 years for $\alpha = 10^{-3}$. For MMEN disk models the growth timescales for $\alpha = 10^{-4}$ and 10^{-5} at 10 au are $\sim$ 2300 and $\sim$ 2900 years, respectively.

The vertical diffusion timescales generally vary between $\sim 10^3 - 10^6$ years, with the longer timescales being relevant only for strongly coupled (sub)μm particles in the inner disk. However, using local dust-gas coupling by calculating local Stokes numbers results in a shorter diffusion timescale compared to the Stokes number calculated using the midplane values [Mulders and Dominik, 2012]. The enhanced dust abundances in regions near the midplane generate particles slightly bigger than those estimated theoretically using equation 3.16 (see Figure 4.13). Hence, although the results do not change significantly beyond $\sim$ 15000 years, we run our simulations until $t \sim$ 30000 years to be absolutely sure that the size distributions we present here are the true steady state results.

4.5.2 Maximum Particle Size Variation with α

As the maximum particle size achieved through collisional dust growth varies inversely with α, the largest size of the particle decreases as the disk becomes more turbulent. In simulations including radial drift and coagulation, but not fragmentation, Brauer et al. [2008] find a similar trend for the most common particle size (which we also see in our results) but note that the effect is modest: only a factor of two increase in predominant particle size with a 10^2 decrease in α. We find that a factor-of-10 *decrease* in α yields nearly a factor-of-10 *increase* in maximum particle size at a given radius—true for both our test simulations of the MMSN (not pictured) and our science simulations of the MMEN (See Figure 4.8). Note that this difference originates

from the adopted value of the fragmentation velocity as well (see Section 4.6 for more discussion). Brauer et al. [2008] suggested that turbulent stirring at higher values of α keeps number densities $n_d(R, z)$ lower, leading to less frequent collisions and frustrated growth. Our simulations have the added effect of more vigorous fragmentation at high α due to the higher relative velocities from stronger turbulence [Weidenschilling, 1984].

4.5.3 Maximum Particle Size Variation with Radial Distance

Particles reach larger sizes in the inner disk than in the outer disk, as seen in figures 4.8 for MMEN and Figures 4.10, 4.11 and 4.12 for MMSN disk models. Figure 4.9 shows Stokes number as a function of z/h_g at 5, 10, and 30 AU for three different grain sizes in the MMSN and MMEN models. Particles in the outer disk have higher Stokes number at a given grain size and value of z/h_g than particles in the inner disk, and so decouple from the gas more easily. Small particles in the outer disk can then attain high values of v_{rel} [e.g. Ormel and Cuzzi, 2007] and hit the fragmentation threshold velocity, while the same particles in the inner disk would keep growing [Birnstiel et al., 2009, Estrada et al., 2016].

4.5.4 Presence of Small Grains in Upper Atmosphere

Even weak turbulence can keep particles as large as 0.1 mm stirred into the disk's upper layers [e.g. Dubrulle et al., 1995]. Figure 4.13 shows $\rho_d(a)$ at the midplane and $3h_g$ at 5 AU for model T2 (MMSN, $\alpha = 10^{-4}$). Although $\alpha = 10^{-4}$ is near the lower limit of expected turbulent efficiency due to the likely onset of hydrodynamic instabilities where MRI is inactive [e.g. Nelson et al., 2013], it is still possible to find 0.1-mm particles at $3h_g$. Local, single-cell simulations without any vertical motion (solid lines) show that the maximum particle size that can grow at $3h_g$ is only $\sim$ 30 μm; turbulent diffusion introduces particles with five times larger radii that grew near the midplane.

In all our simulations, we have used an outflow boundary condition where particles leaving the surface of the disk are not tracked. However, as can be seen from

Figures 4.8, the dust density in the upper layers of the disk at $\sim 3h_g$ is already several orders of magnitude less than that of the midplane. The same trend can be observed in our test simulations T1-T4 as well in Figures 4.10 to 4.12. As a result, an insignificant grain mass is lost over the course of the simulation ($\Delta m/m \lesssim 10^{-6}$). Also, the vertical temperature profile becomes flat at the upper layers of the disk as can be seen in Figure 4.14. Furthermore, in Figure 4.15 we have plotted the vertical optical depth integrated from disk surface to the midplane. The optical depth falls several orders of magnitude below unity within one scale height above the midplane in both short (150μm) and long (1 mm) wavelengths. This suggests that our choice of the particular boundary condition at the disk's surface does not affect the vertical temperature stratification.

4.5.5 Vertical Dust Distribution for Variable α

We now turn to disk models with variable $\alpha(R, z)$. Figures 4.16, 4.17 and 4.18 show steady-state dust density distributions $\rho_d(a, z)$ at 50 au for simulations T4 (MMSN), F7 (MMEN) and H1 respectively. The black dashed lines show $\alpha(R, z)$ as calculated using the methods of Landry et al. [2013]. In each disk, at 50 au we can see the existence of a dead-zone: the midplane is quiescent, with $\alpha(z = 0) = 10^{-5}$ due to suppression of MRI turbulence (a value that might be low enough to trigger hydrodynamical instabilities, which is the case for F8); and the surface layers have strong turbulence [e.g. Gammie, 1996] (though the turbulence may be confined to heights above the upper z-axis limit in Figures 4.16 to 4.18). Unsurprisingly, there is a strong vertical stratification in dust density that mirrors the rapid change in $\alpha(z)$. Any particle that dips below $z/h_g = 1.5$–2 is unlikely to be kicked upward again due to the weak turbulence, so grains stay sequestered near the midplane. Also, we can see a local accumulation of small dust grains with $a \lesssim 10$μm at a height where α suffers a sharp transition. While disks with constant $\alpha(R, z)$ have dust density profiles that are vertically Gaussian, disks with variable $\alpha(R, z)$ have vertical dust density profiles that are strongly non-Gaussian, having a sharp cutoff at some height z.

The fact that different disk models used in this paper have different size distributions $\rho_d(a, R, z)$ means that they will have different vertical optical depths, angles at which starlight is absorbed, and temperature structures. We explore the opacity, optical depth, and gravitational stability of our model disks in the next section.

4.5.6 Opacity, Thermal Profile & Gravitational Stability

In this subsection, we present our results of the opacity calculations and temperature profile of the evolving disk. In Figures 4.19 and 4.20, we show opacity as a function of wavelength for $t = 0$ and steady-state size distributions at 10 au in the MMSN (T2-T4) and MMEN (F5-F7) models, all with $v_{frag} = 100$ cm s^{-1}. Figures 4.21 and 4.22 show the same for 30 au. We define the mean opacity of a grain size distribution $\langle\kappa\rangle_{\rho_d}$ as

$$\langle\kappa(\lambda)\rangle_{\rho_d} = \frac{\int \rho_d(a)\kappa_\lambda(a)\, da}{\int \rho_d(a)\, da}. \tag{4.15}$$

Grains absorb and emit light most efficiently at wavelengths shorter than $2\pi a$ at which point the profile of opacity of dust starts to drop. We see that in steady state, the opacity contribution from small grains at the disk midplane has decreased by 2–3 orders of magnitude from $t = 0$ due to grain growth. Meanwhile, the opacity contribution from particles with $a \gtrsim 30\mu$m has increased. At height $3h_g$, the mean opacity across the size distribution does not evolve as much between $t = 0$ and steady state, though an opacity deficit develops from 1–5 μm as the 0.1 μm monomers are left behind due to selective grain settling. This reduction in opacity is also prominent in the top-most curve of figure 4.6. The silicate resonance features at 10–20 μm, which are produced by warm grains of $1 \lesssim a \lesssim 10\mu$m, also weaken in the midplane, nearly disappearing for the disks with $\alpha = 10^{-5}$. The decrease in opacity at short wavelengths can be attributed to the collisional growth of dust which reduces the abundance of particles with sizes $2\pi a \lesssim \lambda$, for which the opacity curve is wavelength independent. Larger dust particles, due to their sizes exceeding short wavelengths, gain no extinction efficiency but decrease in physical area per unit mass by a factor of the radius. This is also the

reason why the opacity increases at longer wavelengths as dust particles reach those sizes due to collisional growth.

The optical depth, defined by

$$\tau = \int_0^\infty \kappa\rho \, dz \tag{4.16}$$

is also affected by the growth and settling of dust grains. Figure 4.24 shows the optical depth from surface to midplane of models F4-F6 [MMEN, constant $\alpha(R, z)$] plus $t = 0$ at four different wavelengths. Grain growth depletes the small grains and causes the optical depth at $\lambda = 3\mu$m and $\lambda = 10\mu$m to decrease as the disk reaches steady state. At $\lambda = 100\mu$m, all disks with steady-state size distributions are still more optically thin than the $t = 0$ disk. Finally, at $\lambda = 1$ mm, the steady-state disks with $\alpha(R, z) = 10^{-5}$ and 10^{-4} have *increased* their optical depth since $t = 0$ (at least within 35 AU of the star). For $\alpha(R, z) = 10^{-4}$, the disk becomes optically thick at 1 mm inside 10 AU. Figure 4.24 provides a caution that calculating the surface density of grains available for planet formation in the inner disk from (sub)millimeter observations [e.g. Andrews et al., 2013] might not work, as the disk emission may be optically thick as has already been suggested by ALMA observations (e.g., HL Tau disk).

In Figure 4.25 we show the optical depth (τ) for simulations F7 and F8 at $\lambda = 150\mu$m with variable α profile and $\alpha_{min} = 10^{-4}$ and 10^{-5}, respectively. The optical depths at the outer radii are much lower for $\alpha_{min} = 10^{-5}$ than for $\alpha_{min} = 10^{-4}$. However, Nelson et al. [2013], Klahr and Hubbard [2014], Lyra [2014], Marcus et al. [2015] have suggested that hydrodynamic instabilities capable of sustaining angular momentum transport can operate in magnetically dead zones, making $\alpha_{min} = 10^{-4}$ a more physically realistic value.

The opacities in our models can be directly compared to those of Estrada et al. [2016]. The solid red line in Figure 4.25 is the optical depth $\tau = \kappa_R \Sigma/2$ based on the Rosseland mean opacity κ_R. The data have been electronically extracted from two separate subfigures of Figures 3 and 4 of Estrada et al. [2016] (κ from the top row

of Figure 3 and Σ from top row of Figure 4) and interpolated onto the same radial gridpoints as in our models. The Rosseland mean optical depth is roughly equivalent to optical depth at the wavelength where the Planck function peaks, which is $\sim 150\mu$m in the typical temperature ranges in the Estrada et al. [2016]. The optical depth from Estrada et al. [2016] is an order of magnitude more that our values at ~ 30 au, followed by a sharp decrease in the outer nebula.

The optical depth differences between our model and E16 are likely due to advection by gas: the E16 disk has a maximum *outward* gas mass flux at 20 au (see their Figure 4), with outward gas motion everywhere outside 7 au. We believe the gas flow is carrying grains outward so that they pile up at 30 au, causing the large bump in optical depth. The E16 grain pileup is probably also sourced by inward radial drift from the outer edges of the disk, correlated with the sharp drop in optical depth beyond 60 au. Other differences between our model and E16 are grain composition (they use ice opacities where $T < 160$ K where we assume silicates throughout the disk for consistency with our collision model), $\alpha = 4 \times 10^{-4}$ throughout the disk (Figure 4.25 is from our models with variable α), and surface density (bottom of Figure 4.25). The comparison with E16 highlights the importance of gas velocity: in our work, we treat the gas only as a fixed background against which particles evolve. We justify this assumption by the short timescale over which the grain size distribution reaches steady state, but note that even if the gas mass distribution does not significantly evolve over the course of a simulation, the gas velocities may be important when computing the radial distribution of solids.

We expect the changes in mean thermal opacity as a function of wavelength to affect the temperature of the disk interior. Stellar photons are absorbed at a high latitude in the disk where they are re-emitted towards the midplane, heating the disk interior. This energy is then re-radiated and escapes vertically to space resulting into cooling. A vertical column with higher optical depth will absorb more photons only to re-emit them towards the midplane and disk surface, making it harder for the photons to escape the disk vertically at the same time. Moreover, the grazing angle at which

starlight penetrates the disk becomes smaller as dust settling proceeds [Chiang and Goldreich, 1997, Hasegawa and Pudritz, 2011] due to the lack of dust particles high up in the disk, which decreases the photon absorption efficiency as well. Clearly, as the optical depth decreases through the process of grain growth and settling, passive heating becomes less efficient and the interior disk temperature decreases, ultimately lowering the value of Q parameter.

In figure 4.26 we plot the Q (Equation 4.1; left axis, solid lines) and midplane temperature (right axis, dashed lines) as a function of R for MMEN models F2-F4 (left) and disk H1. Both disks show that the midplane temperature decrease and corresponding drop in Q as the disk evolves from $t = 0$ to steady state. The disk with the least efficient turbulence at the midplane [$\alpha(R, z) = 10^{-5}$] becomes the coldest and least stable to axisymmetric perturbations. For model H1 (variable α), the drop in $Q(R)$ caused by grain growth pulls the disk below the $Q = 1.4$ threshold [e.g. Papaloizou and Savonije, 1991, Nelson, 1998, Mayer et al., 2002, Johnson and Gammie, 2003, Pickett et al., 2003]—at which non-axisymmetric modes may begin to grow exponentially beyond ~ 20 au. In Figure 4.27, we present a similar plot for the models F7 and F8 where v_{frag} is taken as 100 cm s^{-1}. Two different values for α_{min} are used for the variable α profile: 10^{-4} and 10^{-5} for the midplane. As expected, the temperature at the midplane is higher for $\alpha_{min} = 10^{-4}$ compared to $\alpha_{min} = 10^{-5}$ by ~ 5 K inside 20 au. Beyond 20 au the temperature difference is $\sim 2-3$ K. Overall, the radial midplane temperature profile is not very sensitive to the choice of α_{min}, specially at the outer radii. However, the inclusion of viscous heating may result in a bigger temperature difference in the inner part of the disk.

4.6 DISCUSSIONS & MODEL LIMITATIONS

Here we have presented a proof-of-concept experiment showing that grain growth alone, with no triggers such as infall or vortices, may be able to drive a massive protoplanetary disk to gravitational instability. Yet instability does not necessarily lead to

the formation of sub-stellar companion, and only if our adopted assumptions are fulfilled, our conclusions become fully applicable to observed protoplanetary disks. Here we discuss the limitations of our model and the robustness of our conclusions.

4.6.1 Only Sticking and Fragmentation (SF) collision outcomes

Out of many collision outcomes—up to nine possible collision outcomes presented by Güttler et al. [2010] but notably erosion, mass transfer, and bouncing [Windmark et al., 2012a]—we have restricted our simulations to just sticking and fragmentation. Any outcome that tends to keep particles small, such as bouncing or erosion, would work against grain settling and disk instability. Also, we have not included planetesimal formation or planet growth, though large bodies increase the velocity distributions of nearby objects, leading to more destructive collisions [e.g. Dobinson et al., 2016]. Our simulations only apply to young disks at the very beginning of disk evolution. However, it is important to remark that larger grains may already be present in young stellar objects [Jørgensen et al., 2007, Steinacker et al., 2010, Ricci et al., 2010, Cox et al., 2015].

4.6.2 Viscous Heating

Although we assume that our disks are MRI-turbulent, we do not include viscous heating but assume that the disk is heated only by stellar photons. The importance of accretion heating depends on the disk accretion rate. For disks with a higher accretion rate, the region where accretion heating dominates expands towards the outer disk. For a classical T-Tauri star with an accretion rate of $\dot{M} \sim 10^{-8} M_{\odot}$ yr^{-1}, the iceline is located around 2 AU [Hasegawa and Pudritz, 2011, Min et al., 2011]. The heating due to the central star varies as $R^{-1/2}$ while the heating due to the accretion process is much steeper with an $R^{-3/4}$ variation [see Dullemond et al., 2007, for a detailed review]. Hence, for classical T-Tauri stars, with an $\dot{M} \sim 10^{-8} M_{\odot}$ year^{-1} the viscous heating dominates only within $1 - 2$AU [Jang-Condell and Sasselov, 2004, Yu et al., 2016] (Also see our figure 4.3). Landry et al. [2013] argue that outside the disk region

where $\Sigma \sim 20$ g cm^{-2} the disk can be assumed to be fully MRI-active. Our MMEN and H1 disk models are substantially heavier that those used in Landry et al. [2013] (See table 4.1), which extends the dead zone to beyond 65 au for heavy disk models. In figure 4.3, we have shown the surface density profile for our MMEN and H1 disk models, where the surface density is more than the 20 g cm^{-2} threshold throughout the radial range of our simulations. However, we expect that the disks with $\alpha(R, z) = 10^{-3}$ might be significantly warmer than what our RADMC simulations of passive heating predict, and so do not include these disks in Figure 4.26 or make predictions about their gravitational stability.

Apart from the viscous accretion, the disk angular momentum can be removed by magnetically induced disk winds if the vertical magnetic flux is relatively strong. For such cases, accretion heating can be neglected even in the inner part of the disk since the value of α due to disk turbulence should be relatively small [Bai, 2016, 2017, Simon et al., 2018]. The existence of a disk wind and its fractional contribution in angular momentum transport is a matter under debate [Hasegawa et al., 2017]. In our model, a disk wind would add an additional advection term for small, fully coupled dust particles. Disk winds are outside the scope of this work and merit separate investigation. However, although not consistent in the upper layers of the disk, our models with low α can mimic the disk wind effect at the midplane.

4.6.3 Grain Composition: Silicate Particles

The literature on collision outcomes is far more extensive for silicates than for any other protoplanetary disk constituent, which led us to restrict our study to silicate particles. However, our model disks are cold enough that particles almost everywhere should be ice-coated, which would change both their opacity and their sticking efficiency. Estrada et al. [2016] and Krijt et al. [2016] have already explored collisions of icy grains. Modeling volatiles also demands the addition of evaporation fronts where solid growth is enhanced. In certain cases the dust-to-gas abundance ratio can be increased by an order of magnitude [see figure 20 of Estrada et al., 2016]. In the context

of disk opacities, porous icy grains would allow particles to grow further due to a higher fragmenting threshold velocity, reducing the abundance of small particles. This effect will lower the opacities at the shorter wavelengths while increasing the opacities at longer wavelengths. Once experimental data on collisions of icy bodies [e.g. Shimaki and Arakawa, 2012, Yasui et al., 2014, Deckers and Teiser, 2016] becomes more complete, it would be worth repeating our experiment with collision outcomes, velocity thresholds, and opacities appropriate to porous ice.

4.6.4 Radial Drift

For this initial experiment we have not included radial drift in our simulations, though we plan to add it in future work. According to Birnstiel et al. [2010, 2011], Drążkowska et al. [2013], Estrada et al. [2016], the outer disk beyond 20–25 au should be drift-dominated, with the particle size spectrum significantly altered. Consequentially, radial drift might result in a cooler outer disk than what is predicted in this work due to the reduction in the efficiency of passive heating, by lowering its opacity to (sub)-mm radiation, while increasing the (sub)-mm opacity in the inner disk. However, the drift timescale is longer than the vertical settling/diffusion timescale for dust particles [Birnstiel et al., 2010].

With our disk setup, the width of the annuli at 40 and 70 au are 7.5 and 14 au respectively, whereas the particles of maximum sizes at those positions travel ~ 6.5 and 12 au respectively in a timescale of $\sim 10^4$ years for an MMEN disk model. Similarly in the inner disk, the width of the column at 5 au is ~ 1.2 au with the maximum drift in the same timescale is ~ 0.9 au. These comparisons suggest that inward radial drift is an important but not dominant effect over the simulation period.

Also, Estrada et al. [2016] showed that radial drift becomes important in the outer disk in limiting the particle size corresponding to $St \sim 0.1$. So, inclusion of radial drift might have some effect on our growth model as well even in somewhat shorter timescales. However, we note that Estrada et al. [2016] also included bouncing

in their model, which slows the growth process, possibly making the growth timescale comparable to the radial drift timescale.

4.6.5 Choice of v_{frag}

For this work we set $v_{frag} = 100$ cm s^{-1} for all our disk models except F1 - F3, for which $v_{frag} = 50$ cm s^{-1}, allowing us to explore our results' sensitivity to fragmenting threshold velocity. Literature values for v_{frag} include 100 cm s^{-1} [experiment F1 by Güttler et al., 2010], 80 cm s^{-1} [Monte Carlo models of Drążkowska et al., 2013], and 50 cm s^{-1} [further work by Drążkowska et al., 2014]. Though there is uncertainty on the appropriate value of v_{frag} for silicate particles, especially when considering variations such as porosity or aggregate type, our choice of relatively low v_{frag} helps keep our maximum particle sizes low, thereby minimizing Stokes numbers and keeping our neglect of radial drift appropriate. Our conclusion that grain growth and settling can trigger non-axisymmetric instability might not apply to disks with stronger particles that better resist fragmentation, where drift can alter the size spectrum.

The dependence of disk opacity on the choice of v_{frag} can be estimated from figure 4.23 where the spectral opacities for simulations F1 - F3 and F4 - F6 are plotted for both the mid-plane and at 3 scale-heights at 30 au. For $\lambda \lesssim 100\mu$m, the opacity is higher for $v_{frag} = 50$ cm s^{-1} compared to 100 cm s^{-1}. This difference is amplified for lower value of α. A higher v_{frag} with a lower turbulence efficiency for a similar surface density puts more mass in the larger particles leaving a small fraction of the total mass for the smaller grains, which are mostly responsible for photon absorption. This effect lowers the opacity of the disk and changes the temperature profile. This trend, however, reverses for $\lambda \gtrsim 100\mu$m and larger, due to the smaller maximum size attained in lower v_{frag} case. Increasing v_{frag} could also intensify the tendency of dust evolution to trigger gravitational instability: Figure 4.7 shows the particle size spectrum (solid lines, solid axes) and wavelength-dependent opacity (dashed lines, dashed axes) for the same region of the disk but with two different values of v_{frag}. Higher v_{frag} decreases the opacity at $\lambda \lesssim 1$ mm but increases it for longer wavelengths, the very effect that

helps decrease Q (§4.5.6, Figures 4.19 to 4.22 and 4.24). The experiments presented here do not cover a wide enough parameter space in collision outcomes for us to be sure that there is a *general* tendency for grain growth to reduce a disk's gravitational stability.

4.6.6 Power-Law Index

In our simulations with different disk models, the disk masses are controlled by varying the value of Σ_0, keeping the power law index of surface density profile $p = 3/2$. As we have discussed in chapter 2 (Section 2.2.1), another widely used power law index for the surface density profile is $p = 1$. $p = 1$ makes the inner disk less heavy due to a shallower radial profile of surface density. How these two different profiles would result into different final states of the disk is still not clear as no direct comparison tests have yet to exist in the literature. Most likely, in the presence of an inward radial drift, the mass flux due to viscous accretion would be different in two cases. However, in our simulations presented in this chapter, radial drift is not included and each vertical column evolves independently. The evolution of dust density stratification, optical depths and changes in opacities thus depend solely by knowing the column density at a particular distance from the central star. Hence, $p = 1$ would only shift the results of our simulations radially outward keeping the basic nature of our findings the same.

It is also important to note that the recent SMA and ALMA observations in the dust continuum in the millimeter wavelengths reveals a surface density power law more consistent with $p = 1$ [Andrews et al., 2013]. These observations are made for disk which already underwent a significant evolution. It is thus not very reasonable to assume that the same power law holds good at $t = 0$, given our current understanding of the micro-physics of a protostellar disk.

4.7 CONCLUSION

In this chapter, we have applied our global dust model, developed in chapter 3, to perform a series of global simulations to track dust evolution in a planet forming

disk. We have used three disk models with different surface densities and have employed both spatially constant and variable turbulence efficiency (α) prescriptions. Our main findings are:

- The collisional growth of dust grains through sticking and fragmentation transfers most of the solid mass to larger particles, leaving a small portion of the total dust mass in the μm and sub-μm dust grains which provide most of the surface area for photon absorption. This results in a reduction in midplane opacities at smaller wavelengths by $3-4$ orders of magnitude compared to the initial values. At the disk surface, however, the opacities decrease mainly due to depletion of dust grains by settling and inefficient growth of the dust particles due to weak coupling between dust and gas.

- Grain growth and settling tend to decrease the optical depths (τ) from disk's surface to its midplane at short wavelengths ($\lambda \lesssim 10\mu$m) by a couple of orders of magnitude, while increasing τ at mm and sub-mm wavelengths. For a typical value of $\alpha = 10^{-4}$, the optical depths at 1 mm inside 30 au exceed unity, which may be problematical for disk mass calculations from (sub)millimeter observations.

- In spite of the depletion of solids in the upper layers of the disk, grains of (sub)micron sizes are stirred high up in the inner disk even when the turbulence strength is small. This effect becomes more prominent when strong turbulence in the disk surface is considered. Because of strong coupling, these dust particles would follow the gas motion in the presence of a disk wind is present, altering the opacities in the disk atmosphere, an essential physical process requiring an in-depth investigation.

- The optical and thermal profiles of the disk are sensitive to the fragmenting threshold velocity (v_{frag}) chosen for modeling the collisional dust growth. We found the opacities at short wavelengths to be $5-10$ times smaller for $v_{frag} =$

100 cm s^{-1} compared to 50 cm s^{-1}. An even higher value of v_{frag}, traditionally chosen for porous icy aggregates would alter the outcomes significantly.

- Grain growth and settling can bring an initially marginally stable protoplanetary disk down below a Toomre $Q = 1.4$ threshold at which non-axisymmetric gravitational instabilities may grow. We find that the disk interior cools as the disk's surface layers are heavily depleted of small grains once the size distribution reaches a steady state, decreasing its stability to gravitational perturbations. As disks with low turbulent efficiency $\alpha(R, z)$ have lower collision speeds, and allow grains to grow and settle more efficiently than disks with active turbulence, we expect to find grain-triggered instability primarily in weakly turbulent disks. The model in which we find $Q < 1.4$ throughout most of the disk is extremely massive, with almost ten times the surface density of the minimum-mass solar nebula. Interestingly, this massive disk is consistent with what theorists propose is necessary for giant planet formation [e.g. Lissauer et al., 2009], but is much larger than typical values inferred from disk observations [Andrews et al., 2013, Ansdell et al., 2016, Pascucci et al., 2016, e.g.]. However, given the evidence that disk masses are systematically underestimated [McClure et al., 2016, Yu et al., 2017, e.g.], our model H1 "heavy" disk mass may be physically plausible.

- Finally, we note that disk instability may not necessarily lead to brown dwarf or star formation, though companions can form in overdense spiral arms [e.g. Kratter and Lodato, 2016]. Disks that become gravitationally unstable may transport angular momentum by gravitoturbulence [Gammie, 2001, Shi and Chiang, 2014, e.g.], or growing spiral modes may saturate [Cossins et al., 2009], keeping the disk marginally stable. Further work would be necessary to track the eventual dynamical outcome of the grain growth and settling studied here.

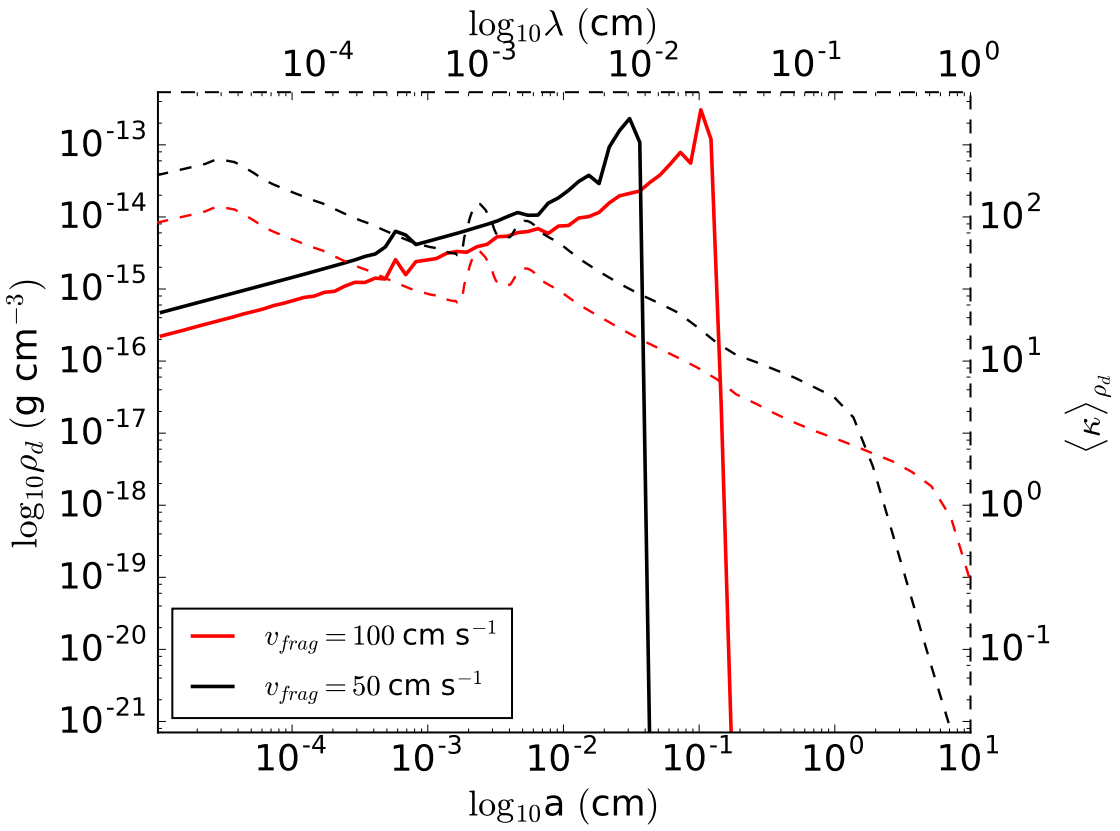

Figure 4.7: The effect of fragmenting threshold velocity on grain size and opacity. The solid curves represent the steady-state dust distributions for $v_{frag} = 100$ cm s^{-1} (solid red) and 50 cm s^{-1} (solid black) for the same location in the disk. The dashed curves show the corresponding mean opacity with the axes placed on right and top. $\langle\kappa\rangle_{\rho_d}$ differs by a factor of ~ 2 between the models.

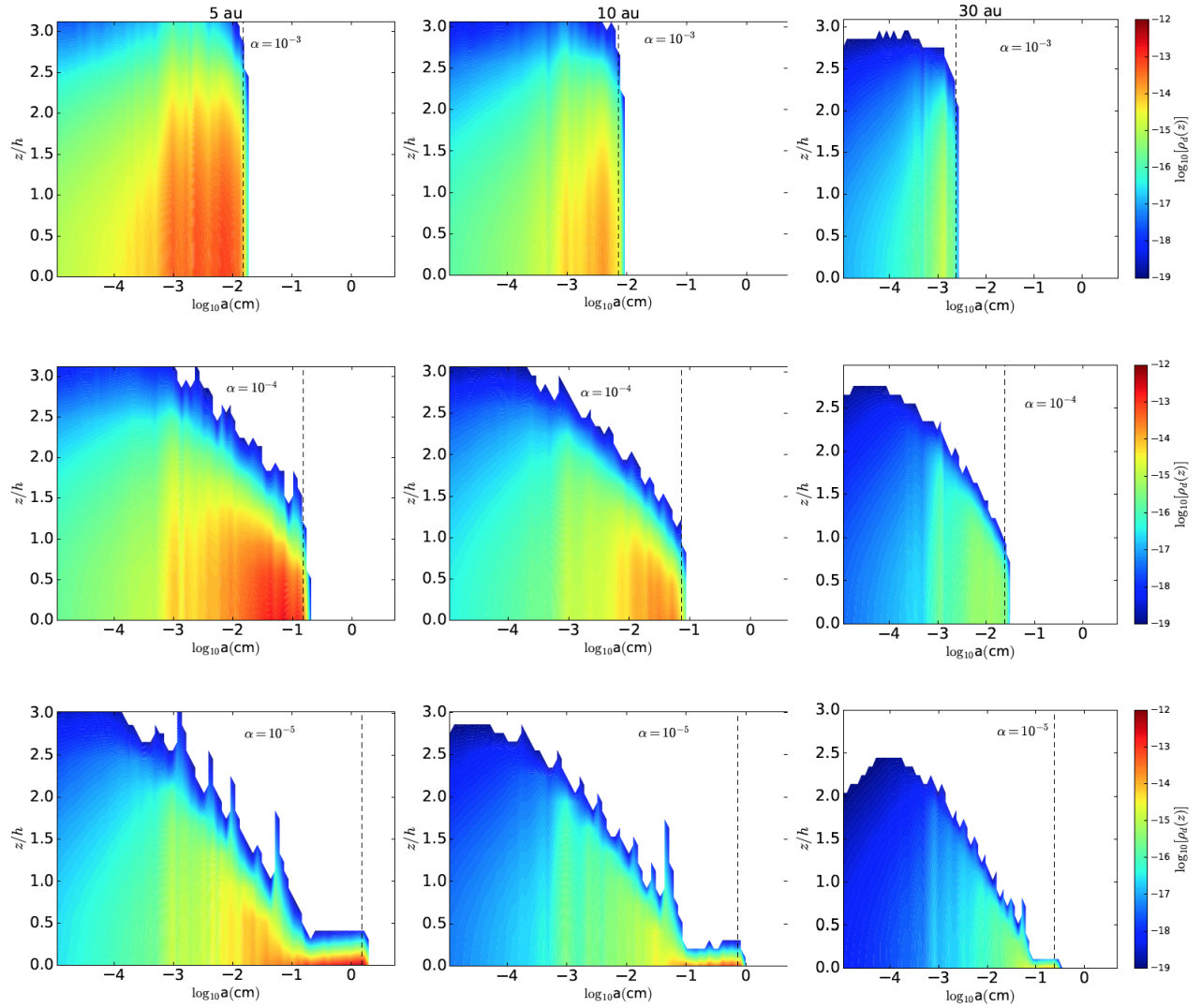

Figure 4.8: Steady state dust distribution for MMEN disk model with $\alpha = 10^{-3}$ (F1), 10^{-4} (F2), and 10^{-5} (F3) from top to bottom for vertical columns at 5, 10 and 30 au (from left to right). The colorbar in each case represents dust density (g cm^{-3} of disk volume) in log scale. The dotted vertical lines show the maximum dust size permissible according to equation 3.16. Grain growth and settling as a function of α can be seen by comparing figures from different rows. Also, the growth becomes less effective as we move towards the outer disk regions due to the lower gas density and higher Stokes number of dust particles. Similar sized grains attain v_{frag} faster in the outer disk because of the low dust-gas coupling. The spikes in the figures are due to Monte Carlo noise.

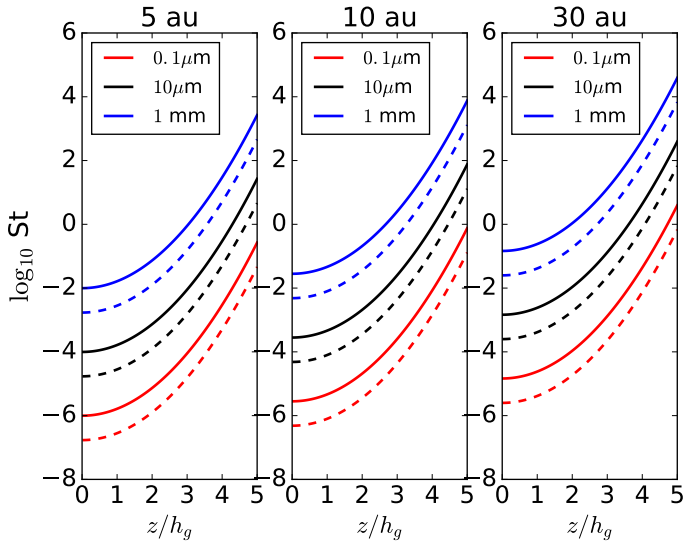

Figure 4.9: Stokes number as a function of height for particles of different size. The solid lines show the MMSN model and the dashed lines represent the MMEN (model F2).

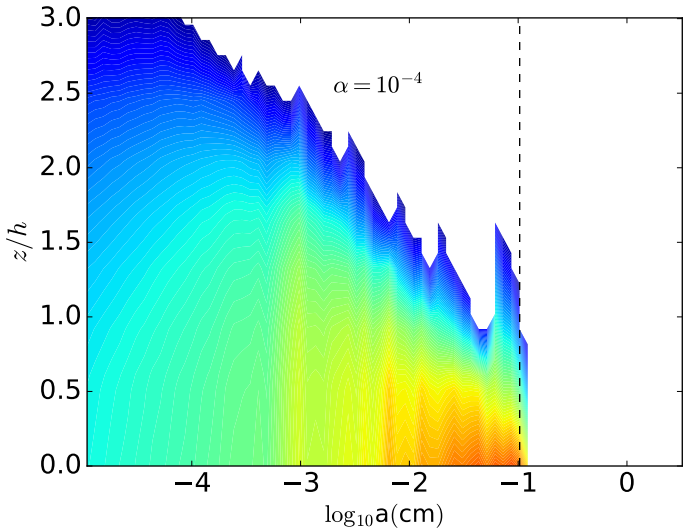

Figure 4.10: Steady-state dust density distribution $\rho_d(a, z)$ for our T2 test model (MMSN; $\alpha = 10^{-4}$) at 5 au. The colorbar is the same as Figure 4.12 and represents the dust density in log scale. The visible spikes in the surface plots originate from the Monte Carlo noise in the simulations. The vertical dashed line denotes the maximum particle size allowed according to equation 3.16. Our simulations agree well with analytical results.

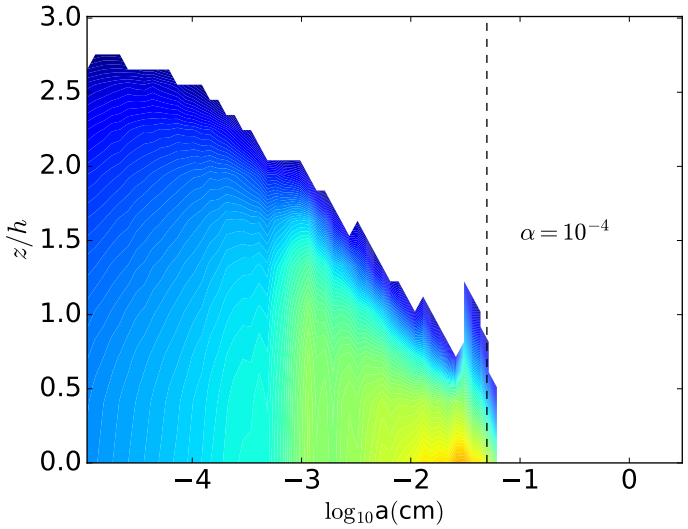

Figure 4.11: Steady-state dust density distribution $\rho_d(a, z)$ for our T2 test model (MMSN; $\alpha = 10^{-4}$) at 10 au. The colorbar is same as Figure 4.12 and represents the log of dust volume density in g cm^{-3}.

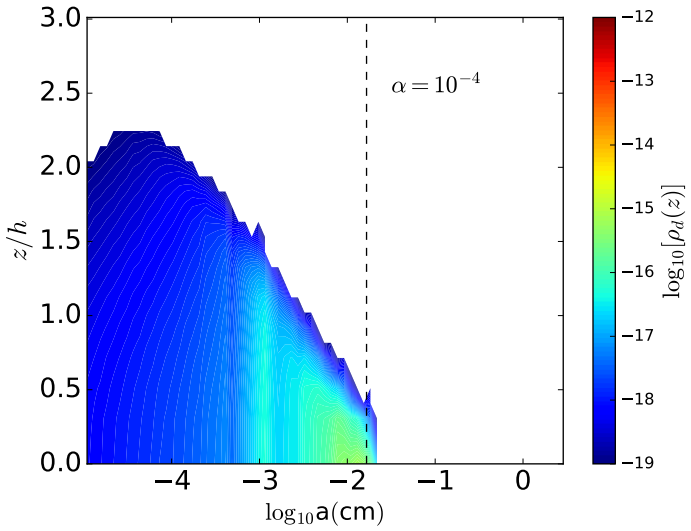

Figure 4.12: Steady-state dust density distribution $\rho_d(a, z)$ for our T2 test model (MMSN; $\alpha = 10^{-4}$) at 30 au.

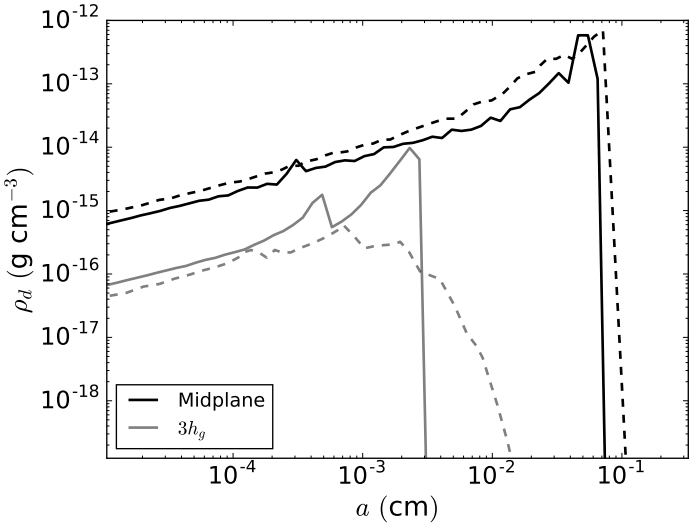

Figure 4.13: The steady state dust abundance at midplane and 3 scale-heights above midplane for an MMSN disk with $\alpha = 10^{-4}$ at 5 au. The solid lines show the dust distributions that we would have achieved from a local simulation and the dotted curves show the distributions obtained from simulation with full dust dynamics in the vertical direction implemented. The extra growth at the midplane takes place due to enhanced dust abundance from vertical settling. The abundance of dust grains of sizes $\sim$ a few tens of micron at 3 scale heights is not due to the local collisional growth, but rather can be attributed to the vertical turbulent stirring.

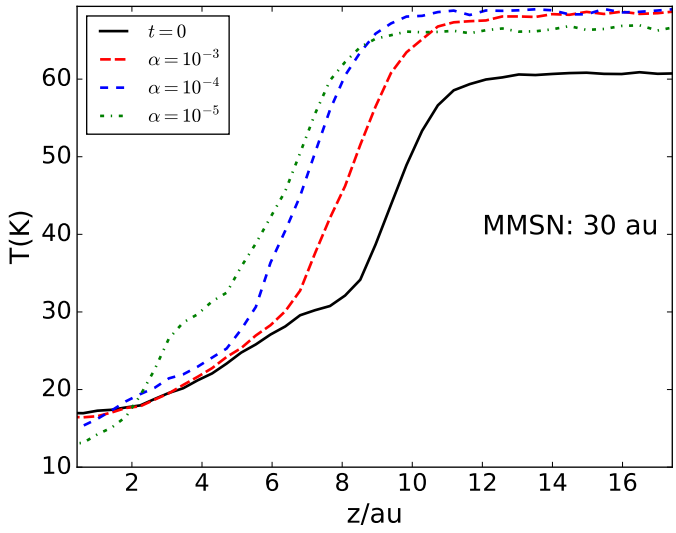

Figure 4.14: The vertical temperature stratification for MMSN disk model, as a part of our code test. The temperature stratification is shown for a column at 30 au. A stratification in the dust population is expected to result in a temperature stratification in which the midplane gets cooler while the surface of the disk becomes warmer.

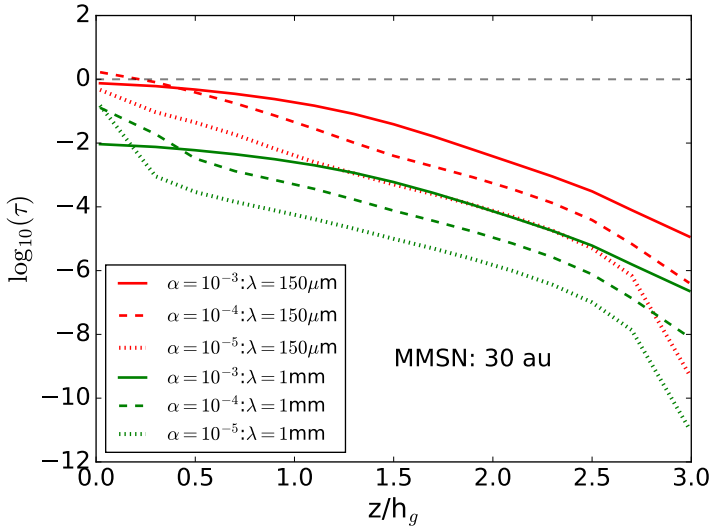

Figure 4.15: The vertical optical depth from the disk's surface to the midplane for the same column at $\lambda = 150\mu$m and 1 mm. The optical depths in all cases at $z = 3h_g$ are several orders of magnitude below unity. This also suggests that the small amount of dust particles which leave the simulations due to the boundary condition at the disk's surface do not affect the temperature structure. The horizontal dashed line represents $\tau = 1$.

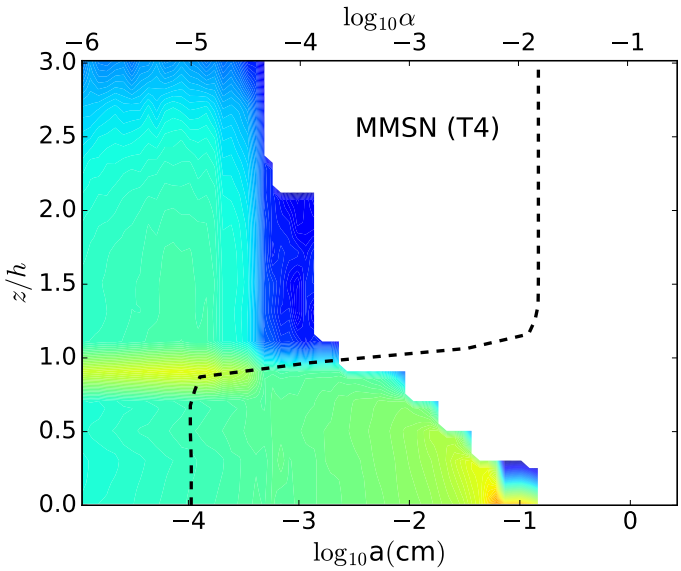

Figure 4.16: Steady-state dust density distribution with variable $\alpha(R, z)$ profile for MMSN disk model at 50 au. The colorbar is same as Figure 4.18 and represents dust density (mass per unit disk volume) in log scale. The values of $\alpha(R, z)$, obtained from the ionization-recombination chemistry model of Landry et al. [2013], are shown with black dashed line with the axis on the top of each plot. The pattern of the steady-state distributions is markedly different from that for constant α profile shown in Figure 4.8. Dust becomes sequestered in the midplane dead zone, where weak turbulence prevents grains from getting kicked upward. In all the simulations, a slightly higher concentration of smaller dust grains is obtained at heights above where $\alpha(z)$ makes a sharp transition. However, this feature may not be present for an $\alpha(R, z)$ profile evolving in time with the evolution of gas-to-solid ratio.

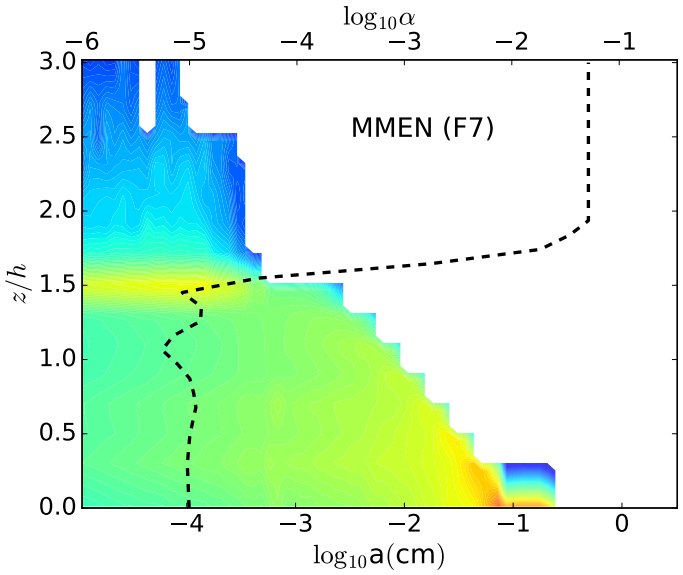

Figure 4.17: Steady-state dust density distribution with variable $\alpha(R, z)$ profile for MMEN disk model at 50 au with $v_{frag} = 100$ cm s^{-1}. The explanation of this plot is similar to Figures 4.16. The colorbar is same as Figure 4.18.

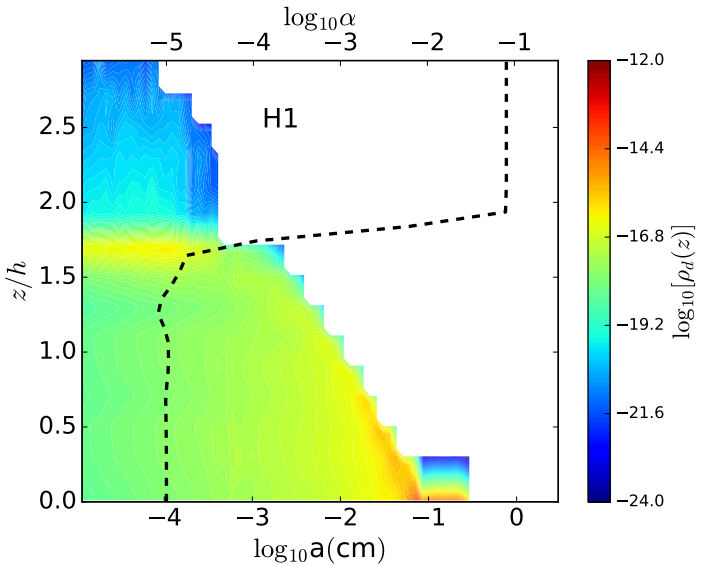

Figure 4.18: Steady-state dust density distribution with variable $\alpha(R, z)$ profile for H1 disk model at 50 au with $v_{frag} = 100$ cm s^{-1}. The explanation of this plot is similar to Figure 4.16 and 4.17.

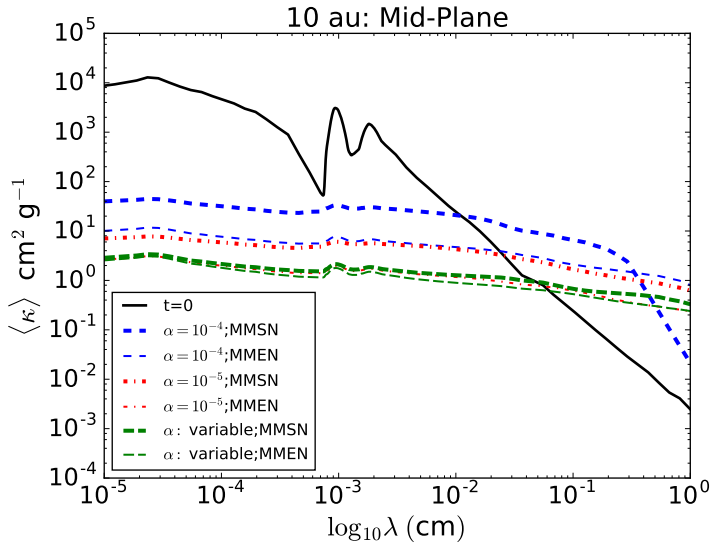

Figure 4.19: Opacities $\langle\kappa(\lambda)\rangle_{\rho_d}$ from the $t = 0$ disk (solid line) and the steady-state size distributions (dashed lines) for the MMSN and MMEN disk models at the midplane of a vertical column at $R = 10$ au.

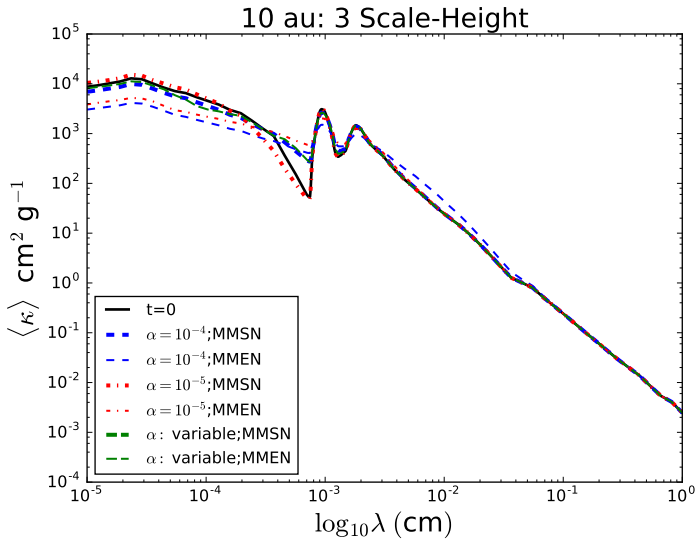

Figure 4.20: Opacities $\langle\kappa(\lambda)\rangle_{\rho_d}$ from the $t = 0$ disk (solid line) and the steady-state size distributions (dashed lines) for the MMSN and MMEN disk models at 3 scale heights above the midplane of a vertical column at 10 au. Grain growth significantly reduces the short-wavelength opacity and increases the long-wavelength opacity at the midplane, while having much weaker effects at $z = 3h_g$. Depending on the position in the disk and strength of the turbulence, the quantity $\langle\kappa\rangle_{\rho_d}$ can differ by more than an order of magnitude.

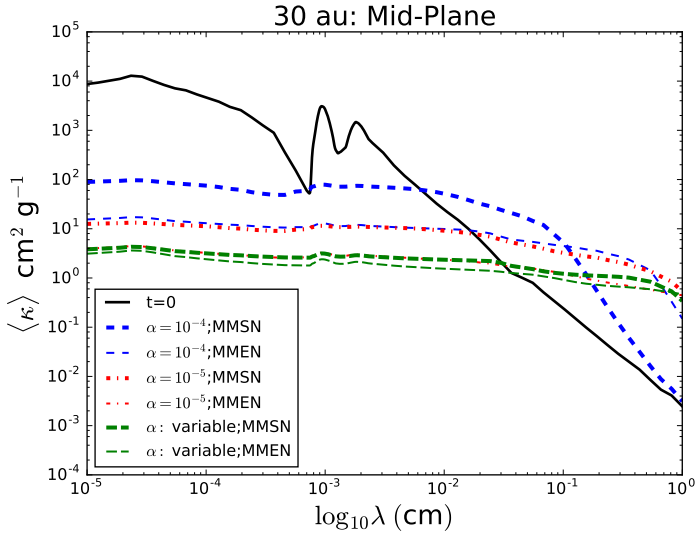

Figure 4.21: Opacities $\langle\kappa(\lambda)\rangle_{\rho_d}$ from the $t = 0$ disk (solid line) and the steady-state size distributions (dashed lines) for the MMSN and MMEN disk models at the midplane of a vertical column as Figure 4.19 but at $R = 30$ au.

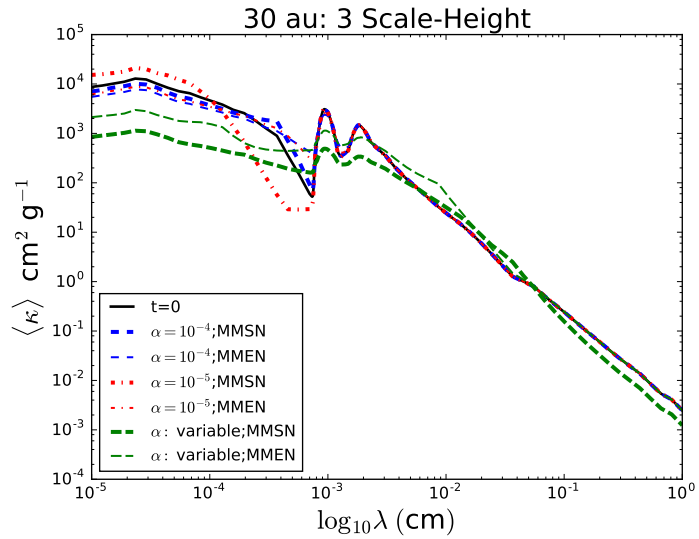

Figure 4.22: Opacities $\langle\kappa(\lambda)\rangle_{\rho_d}$ from the $t = 0$ disk (solid line) and the steady-state size distributions (dashed lines) for the MMSN and MMEN disk models at $z = 3h_g$ of a vertical column as Figure 4.20 but at $R = 30$ au.

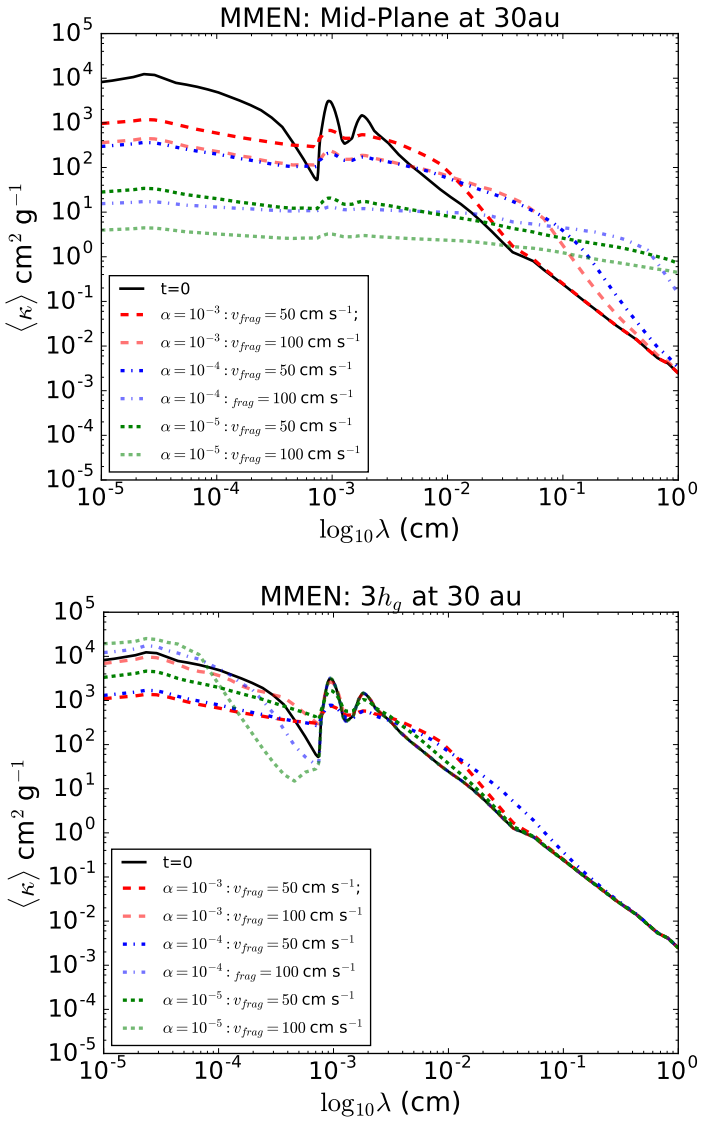

Figure 4.23: Spectral opacities $\langle\kappa(\lambda)\rangle_{\rho_d}$ at mid-plane (left) and 3 scale-heights above (right) for simulations with MMEN disk models with $v_{frag} = 50$ (F1, F2 and F3) and 100 cm s^{-1} (F4, F5 and F6) at a radial distance of 30 au from the central star. For $\lambda < 100\mu$m, lower v_{frag} leads to higher opacity, while higher $v_{\rm frag}$ allows larger particles to stick, decreasing the opacity. The relationship between $v_{\rm frag}$ and opacity is especially strong for low values of α. This trend, however, reverses for $\lambda \sim 100\mu$m and larger, due to the smaller maximum size attained in the lower v_{frag} case (see equation 3.16). At the disk surface (right plot), the behavior is the same, although the differences in opacities are small due to restricted grain growth arising due to lower gas density and weak coupling between gas and dust.

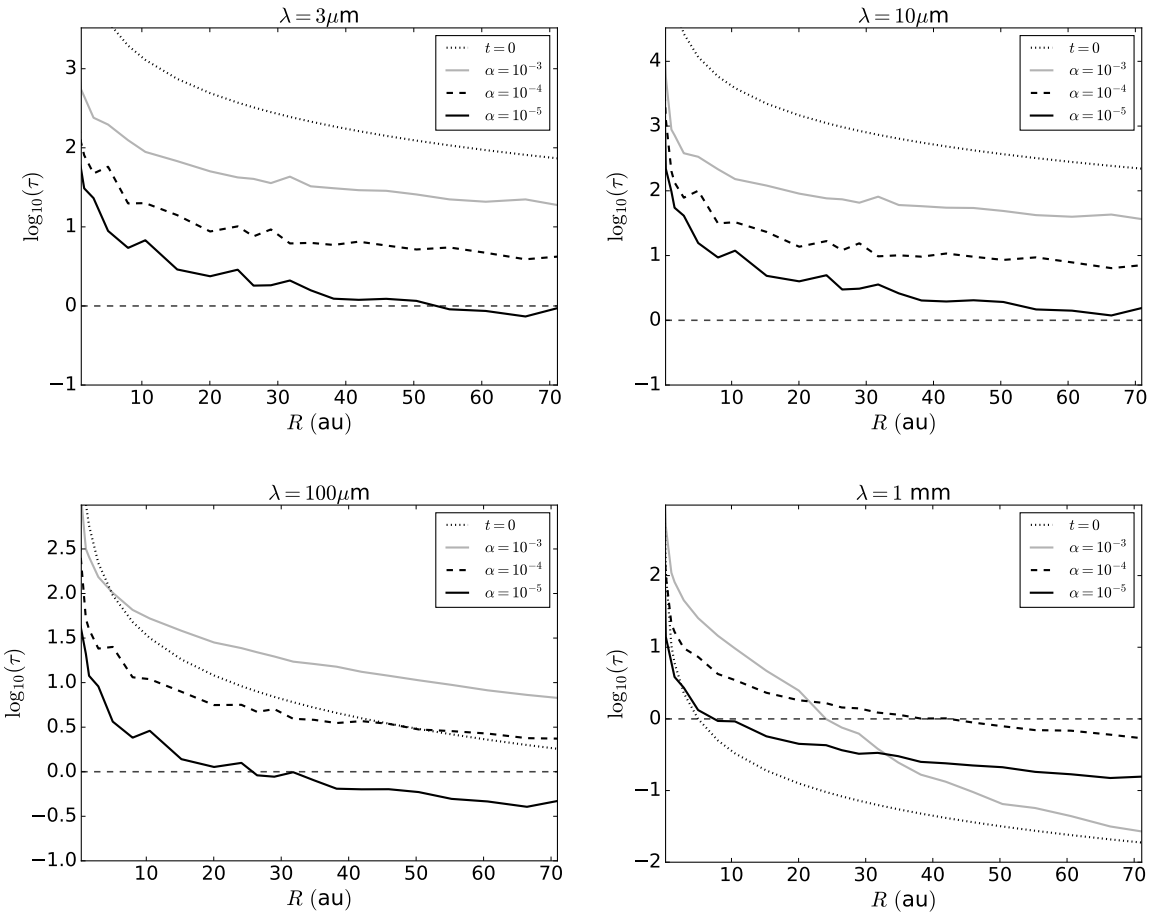

Figure 4.24: Optical depth $\tau(R)$ integrated from the disk surface to the midplane for the MMEN models F4 - F6 with constant α. The dashed horizontal line in each figure shows $\tau = 1$. At $\lambda = 3\mu$m and $\lambda = 10\mu$m the optical depth, which is provided by the smallest grains, drops as grain growth becomes more efficient (decreasing α). At $\lambda = 100\mu$m the disk with the highest optical depth at $R > 30$ AU has $\alpha = 10^{-4}$. Finally, while the disk starts out optically thin at $\lambda = 1$ mm outside 3 AU, its optical depth *increases* once grains begin to grow. For $\alpha = 10^{-4}$, the disk even becomes optically thick out to $R = 40$ AU once the dust size distribution reaches steady state.

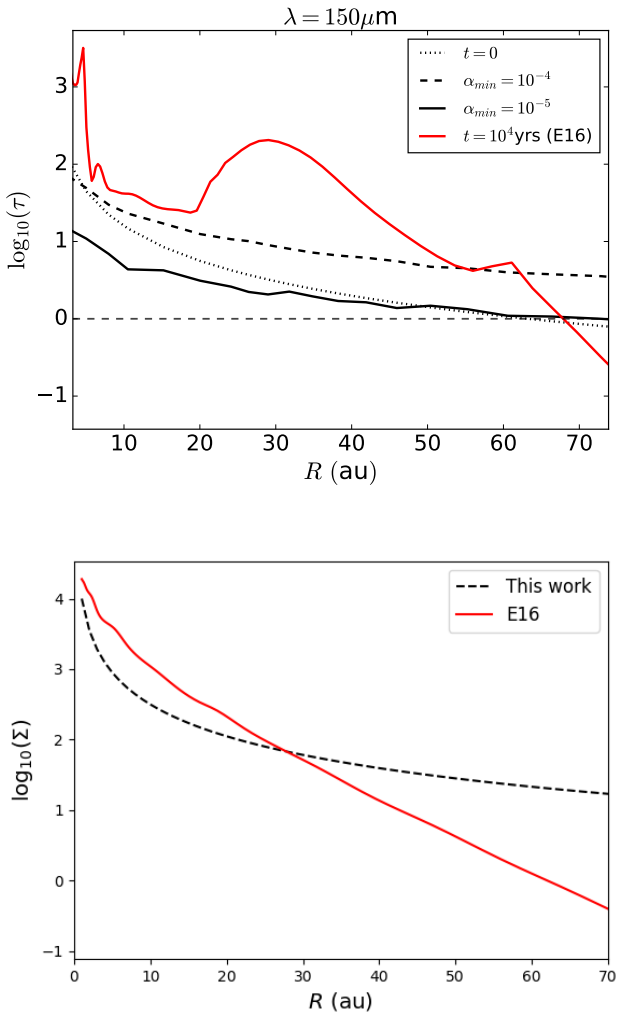

Figure 4.25: **Top:** Steady state optical depth τ at 150μm as a function of radial distance for models F7 (solid black) and F8 (dashed black) with variable α profile with $\alpha_{min} = 10^{-5}$ and 10^{-4}, respectively at the midplane. $\alpha_{min} = 10^{-4}$ at the midplane is more consistent with a turbulence model where hydrodynamic processes contribute to angular momentum transport [Nelson et al., 2013, Stoll and Kley, 2014, Estrada et al., 2016, Turner et al., 2014]. The red solid line is the Rosseland mean optical depth from Estrada et al. [2016], who find peak dust emission at $\lambda \sim 150$μm, with $\alpha = 4 \times 10^{-4}$. Gas advection in the E16 model causes the optical depth bump at ~ 30 au; since we hold the gas surface density fixed in our simulations, we are not able to assess whether grains should pile up anywhere in our model disks. Other differences between our optical depths and those of Estrada et al. (2016) are likely caused by grain composition (silicate vs. ice) and radial drift, which removes most of the grains from $R > 60$ AU. **Bottom:** The surface densities for the MMEN disk model and that from the model of E16.

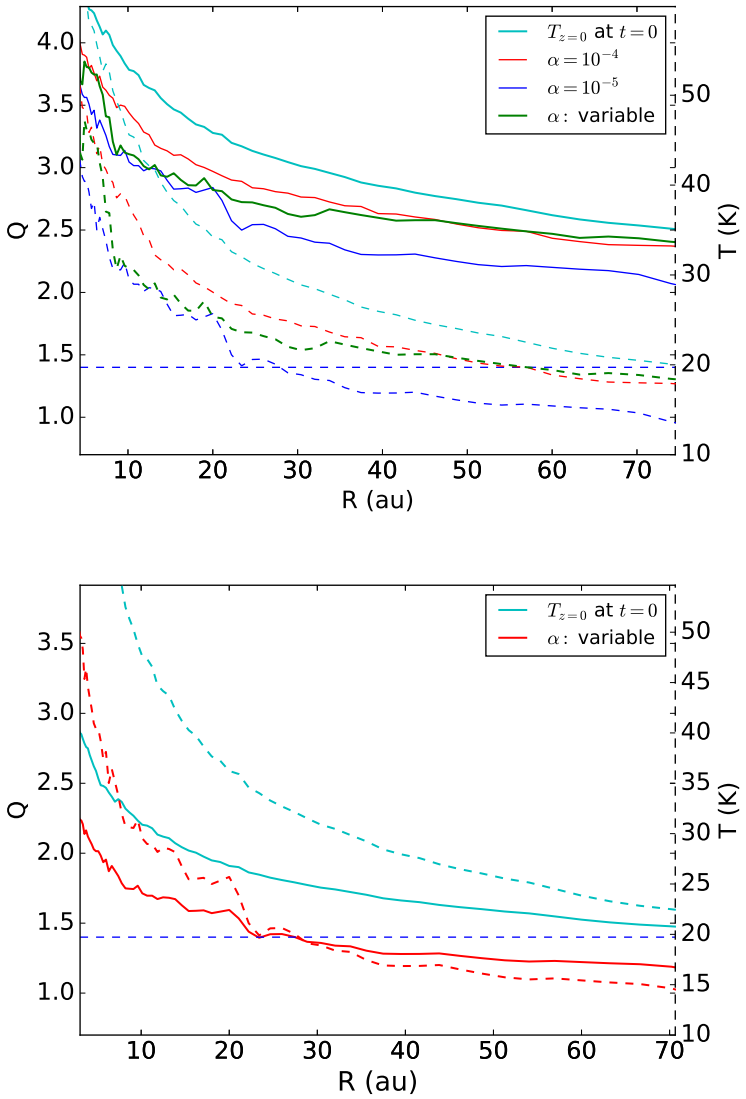

Figure 4.26: Toomre Q parameter and midplane temperature as a function of radius for MMEN (F5 - F7, v_{frag} = 100 cm s^{-1}, top) and H1 (bottom) disk model. Solid lines show $Q(R)$ referenced to the left axis and dashed lines show midplane temperature referenced to the dashed right axis. The dotted horizontal line denotes $Q = 1.4$, a value where the disk might become unstable to non-axisymmetric perturbations (e.g. spiral modes) [Papaloizou and Savonije, 1991, Nelson, 1998, Mayer et al., 2002, Johnson and Gammie, 2003, Pickett et al., 2003]. For both disks $Q(R)$ can drop by $0.3-0.4$ from its initial value, with the biggest drops in Q and T associated with disks with the weakest turbulence. The spiky features in the temperature profile and hence in Q profile for the inner disk regions arise due to Monte Carlo noise in the RADMC calculations.

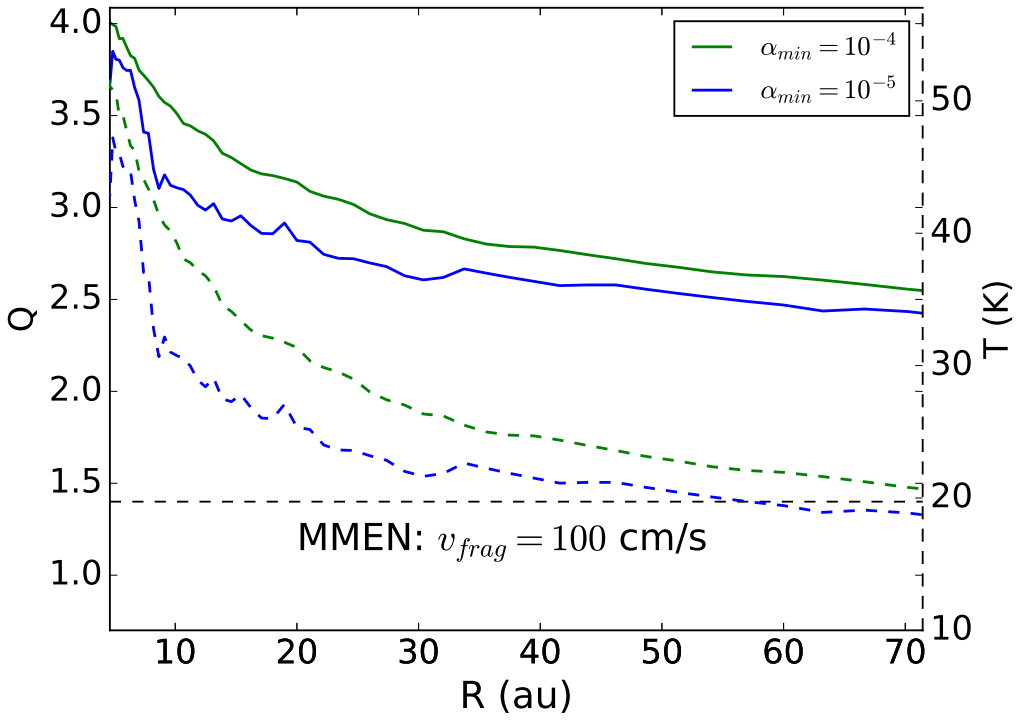

Figure 4.27: A figure similar to figure 4.26 for the models F7 and F8 where $v_{frag} = 100$ cm s^{-1} is used and the α profile is variable with α_{min} at the midplane equal to 10^{-5} (green) and 10^{-4} (blue), respectively. The temperatures are also shown with the dashed curves and with an axis placed on the right-hand-side. The overall temperature difference is not highly sensitive to the minimum value of α, especially in the outer disk. The dashed black horizontal line corresponds to $Q = 1.4$.

Chapter 5

APPLICATIONS OF DUST MODEL II: REDUCTION IN GAP OPENING MASS DUE TO DUST SETTLING

5.1 Introduction

Starting from the collisional growth of sub-micron size dust particles, the process of planet formation proceeds through several phases. The extraordinary diversity of the masses and orbital locations of planets, determined in recent high-resolution ground and space based telescopic observations, has confirmed that post formation evolution of planetary bodies is as crucial as the processes responsible for forming planetesimals and planetary cores. According to the current confirmed exo-planetary population, planet mass ranges from as small as the mass of Mercury all the way upto several Jupiter masses. Similarly, a surprising distribution of semi-major axis is also notable in that giant planets with masses ~ 0.5 M_{Jup} or more are observed in close-in orbits [Armitage, 2007, Kley and Nelson, 2012, Raymond and Cossou, 2014]. The difficulties of forming these close-in planets in-situ is problematic for both of the planet forming scenarios of core-accretion and gravitational fragmentation. This problem led to the idea of planetary migration where planets are formed in wide orbits and move inward by interacting gravitationally with the gas disk [Goldreich and Tremaine, 1979, Lin and Papaloizou, 1993, Kley and Nelson, 2012, Baruteau et al., 2014].

In the initial stages of planet formation the gaseous component of the disk controls the growth and dynamics of the solids. However, in the later stages, the planetesimals and protoplanets impact the gas dynamics and modify the disk's gas surface density structure of the disk. During this time the planetary bodies also suffer a change in their orbits by moving inward or outward, depending on the local physical parameters of the disk. The post formation evolution has two distinct phases. In

the first phase, the orbital migration takes place due to the interaction between the planet and the gas disk. In contrast, the second phase originates from the planet-planet or planet-planetesimal scattering after the gas disk has fully dispersed [Hahn and Malhotra, 1999, Terquem and Papaloizou, 2002, Chatterjee et al., 2008, Jurić and Tremaine, 2008].

When a planet is embedded in the gas disk, the gas experiences torques from the planet and the disk itself. The relative strengths of the two torques exerted on the disk material modifies the local structure of the gas surface density. In this process, the planet receives angular momentum from the inner part of the disk and transfers some angular momentum to the outer disk [Lin and Papaloizou, 1979, Goldreich and Tremaine, 1979, 1980]. By the interaction with the disk through an exchange of angular momentum the planet pushes the inner disk inward and the outer disk outward, which reduces the local surface density in the vicinity of the planet. Turbulent diffusion of the gaseous disk material, on the other hand, tries to fill this low density region. If the planet can disperse the material in a timescale shorter than the timescale in which material is replenished, a gap is created in the disk.

The effect of a planet induced gap in a gaseous disk on the post formation planetary evolution is two-fold. Before the gap is created, the planet in the gas disk is subjected to what is called type I migration, which arises due to the unbalanced torque exerted on the planet by the disk. As the torque exerted by the outer disk is generally stronger than the that by inner disk, the planet loses angular momentum due to the unbalanced torque and spirals inward [Tanaka et al., 2002]. Several works have shown that, for a disk with a smoothly varying surface density, the timescale for type I migration is too fast to reproduce the observed planetary population [Ward, 1997, Nelson et al., 2000, Tanaka et al., 2002, D'Angelo et al., 2003, Hasegawa and Pudritz, 2010]. However, once a gap is created, the planet enters into the type II migration regime, where planet migration happens on the viscous timescale of the disk. The type II migration timescale is longer than that of type I migration in the planet dominated regime for high mass planets.

Secondly, in terms of the formation of planets, a gap can stall the growth of a planet or at least can slow it down. Once a planetary core of several Earth masses is reached, the planet tends to accrete the matter (dust and planetesimals) in its vicinity. This leads to a rapid growth of the planet in the final stages of formation. However, once a gap is induced by the planet itself due to its growing mass, the matter available for the planet to accrete depletes and the growth slows down significantly.

In this chapter we focus on how dust growth and settling can abet the process of gap formation. We have seen in chapter 4 that the overall growth and vertical settling of solid bodies result into a cooling of the disk midplane. This alters the vertical stratification of the gas density in the disk, and hence, the local disk scale height of the gas. Our main objective is to investigate whether the changed vertical structure can alter the criteria for opening a gap. If so, how does it affect the critical mass of the growing protoplanet that can tidally disperse all the matter around it to induce a significant dip in the local surface density.

5.2 The Gap-opening Criteria

As the mass of a growing planetary candidate increases, the strength of the gravitational interaction between the planet and the disk gas increases as well. This interaction acts in the form of a torque with which the disk and the planet exchange angular momentum. A planetary mass object influences the disk in two ways. First, it divides the disk into inner and outer parts and second, it launches spiral arms which are over-dense regions. These spiral arms play a key role in the process of angular momentum exchange. As can be seen in Figure 5.1, the planet induces the spiral arms which are then sheared due to Keplerian rotation of the disk. The inner spiral leads the planet whereas the outer one trails it. The creation of the spiral arms by the planet destroys the symmetry of gas distribution of the disk around the planet. The torque produced by the spiral arms can be easily understood from Figure 5.1. The gravitational attraction between the outer spiral and the planet tends to slow the planet down. In this process, the planet loses angular momentum and moves inward.

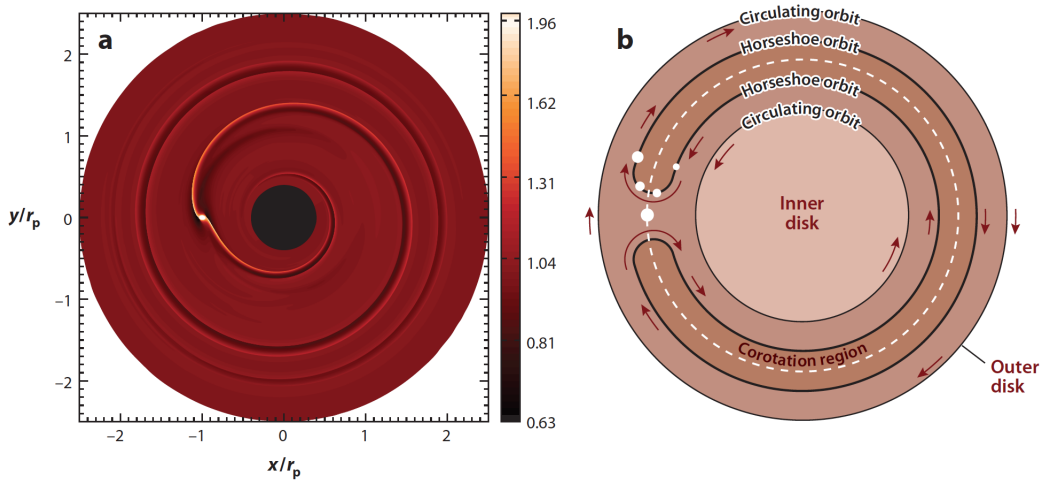

Figure 5.1: **left:** The Figure on the left shows the morphology of spiral arms created by a planet. The inner spiral leads the planet while the outer one trails. The planet in this case is orbiting in a counter-clockwise direction. **Right:** The Figure shows how a planet divides a disk into an inner and outer part separated by a co-rotation zone. The fluid parcel exchanges angular momentum with the planet while crossing through the horseshoe region of the co-rotation orbit. Figure is taken from Kley and Nelson [2012] with the authors' permission.

The interaction with the inner spiral arm, on the other hand, tries to accelerate the planet providing it more angular momentum. The relative strength of the two effects determines the final trajectory of the planet through the disk.

The gravitational potential of the planet at a point in the disk can be expressed as a sum of Fourier components [Goldreich and Tremaine, 1979] and can be written as

$$\psi_p(R,\phi,t) = -\frac{Gm_p}{|\vec{R}_p(t) - \vec{R}} = \sum_{m=0}^{\infty} \psi_m(R)\cos\left[m\left(\phi - \phi_p(t)\right)\right] \tag{5.1}$$

where m_p is the mass of the planet and $\phi_p(t) = \Omega_p t$ is the azimuth angle of the planet. Here, Ω_p is the pattern speed. The $\psi_m(R)$ are the Fourier components of the potential for the m^{th} mode, rotating with the pattern speed Ω_p [Goldreich and Tremaine, 1979, 1980, Meyer-Vernet and Sicardy, 1987, Kley and Nelson, 2012, Baruteau et al., 2014]. The total torque on the planet exerted by the disk can thus be written as

$$\Gamma_{total} = -\int \Sigma\left(\vec{R}\times\vec{F}\right)\,dS = \int \Sigma\left(\vec{R}\times\nabla\psi_p\right)\,dS = \int \Sigma\frac{\partial\psi_p}{\partial\phi}\,dS \tag{5.2}$$

where the integration is carried out over the disk and dS is a surface element. When the planet mass grows beyond a critical point, the strength of the mutual gravitational interaction and the exchange of angular momentum increases. If the angular momentum exchanged by the planet is not sufficiently carried away by the spiral arms due to viscous dissipation or shock waves, and is locally deposited in the disk, angular momentum is lost by the material in the inner disk and gained by the gas in the outer disk. In both cases, the disk material is repelled by the planet and a gap is created.

Whether a planet would open a gap depends on two conditions. First, The thickness of the disk has to be small enough such that the matter can not accrete past the planet. If the thickness of the disk becomes smaller than the Hill radius of the planet, the gas from the outer disk would come within the Hill radius of the planet while being accreted by the central star. As the planet's gravity dominate over the stellar gravity within its Hill radius, the gas would be accreted by the planet in stead of reaching the central star. The diffusive accretion of the gas from the inner disk, however, continues over the viscous timescale and a gap is opened. This condition is quantified by setting the Hill radius of the planet greater than the local disk scale height:

$$R_H = a_p \left(\frac{m_p}{M_\star} \right)^{1/3} \geq h_g. \tag{5.3}$$

Here, R_H is the Planet's Hill radius within which the planet's gravity dominates over the stellar gravity, and a_p is the planet's semi-major axis. This is also sometimes referred to as the thermal condition for opening a gap. For a typical MMSN disk model with isothermal conditions the aspect ratio $h_g(R)/R \sim 0.05$. For $m_p/M_\star \sim 10^{-4}$, the minimum mass for the planet required to open a gap is ~ 0.1 M_{Jup}.

Second, the viscous condition, requires that viscosity in the disk does not close the gap by filling material into it too quickly. This condition can be stated as $\tau_{tidal} < \tau_{visc}$, where τ_{tidal} is the timescale in which material is removed from the gap, and τ_{visc} is the timescale in which the disk fills in the gap viscously. Writing the torque as $\Gamma = dJ/dt$, where J is the angular momentum of the disk gas in the vicinity of the

planet, the above condition can be stated as

$$\left(\frac{dJ}{dt}\right)_{tidal} \geq \left(\frac{dJ}{dt}\right)_{visc}. \tag{5.4}$$

Following Goldreich and Tremaine [1979], Lin and Papaloizou [1979, 1986], the rate of angular momentum transfer from the planet to the disk can be written as

$$\left(\frac{dJ}{dt}\right)_{tidal} = fq^2\Sigma a_p^2\Omega^2\left(\frac{a_p}{b}\right)^3 \tag{5.5}$$

where $f \sim 0.23$ is a constant, a_p is the planet's semi-major axis, $q = m_p/M_\star$ is the ratio of planet to stellar mass and $b = a_p - R$ is the impact parameter for fluid parcel passing the planet's orbit. The rate of transfer of angular momentum by the viscous disk can be written following Lynden-Bell and Pringle [1974] as

$$\left(\frac{dJ}{dt}\right)_{visc} = 3\pi\nu\Sigma a_p^2\Omega_p \tag{5.6}$$

where $\nu = \alpha c_s h_g$ is the disk viscosity. Applying equations 5.5 and 5.6 in equation 5.4, we get

$$q \geqslant \frac{40\nu}{a_p^2\Omega_p}. \tag{5.7}$$

Crida et al. [2006] combined the criteria of equations 5.3 and 5.4 to present a unified gap opening criteria as

$$p = \frac{3}{4}\frac{h_g}{R_H} + \frac{50}{q\mathcal{R}} \leqslant 1 \tag{5.8}$$

where $\mathcal{R} = \Omega_p a_p^2/\nu$ is the Reynolds number. For a typical MMSN disk model with $h_g(R)/R \sim 0.05$, $\alpha = 0.01$ and $q \sim 10^{-3}$, the mass of the planet required to open a gap is ~ 2.5 M_{Jup}. We note that the viscous condition, being more stringent than the thermal condition, determines the opening of the gap.

5.3 Simulation Setup

The global modeling of a protoplanetary disk and planet formation are generally performed in one or two dimensions. Although, full 3-D global simulations are recently being performed using codes, such as FARGO3D [Masset, 2000], our present computational capacity does not allow us to resolve the disk and its micro-physics in full detail. Often, the numerical simulations are performed in two dimensions where the disk models are either vertically or azimuthally averaged. For simulations of dust growth and settling, a vertical slice of the disk is taken into consideration and an azimuthal symmetry is assumed. One of the most important aspect of dust modeling is the generation of synthetic images which are often used as the templates to interpret the observations. Hence, the vertical dust structure is more relevant and important, as our observations are based on the vertical optical depths, specially for the face-on disks.

The post-formation planetary evolutions through planet migrations, on the other hand, mostly take place near the disk midplane. In this case, the non-axisymmetric structures, such as spiral arms, play an important role. So, these simulations are generally performed using disk models which are vertically averaged, and the computational power is fully utilized to resolve the $R - \phi$ plane of the disks. In this chapter, we are going to investigate how the process of dust settling reduces the gap-opening mass of a growing proto-planet, and we are mostly interested in the evolution of the detailed vertical structure of the dust size distributions. Hence, we shall be restricted to the pre-formation phases of planet formation and shall use the same dust model as presented in chapter 3. However, unlike our first applications of the dust model in chapter 4, the simulations and results presented here include radial drift of dust particles.

To conduct our investigations on the reduction in gap opening mass due to dust settling, we have used four different disk models with different masses. The disk surface

density profile is taken as

$$\Sigma(R) = \Sigma_0 \left(\frac{R}{1\ au} \right)^{-3/2}, \tag{5.9}$$

where four different values of Σ_0 have been adopted. The corresponding disk masses are 0.018 $M_\odot$, 0.04 $M_\odot$, 0.07 $M_\odot$ and 0.1 $M_\odot$ where values for Σ_0 are 1700, 4400, 7200 and 9900 g cm^{-2} respectively. We note that the first and the fourth disk models are the well-known MMSN and MMEN disks we have used in our applications in the previous chapter. For each disk, we have use four different values of α: 10^{-2}, 10^{-3}, 10^{-4} and 10^{-5} (See table 5.1 for a detailed list of the simulations with their respective names). In this chapter, we have not used the variable α profile for our simulations.

The inner disk radius R_{in} is taken as 0.06 au and the outer radius is R_{out} = 85 au. Each disk model is extends to 4 scale heights in the vertical direction above the midplane. The total radial range is divided into 48 vertical columns equi-spaced in log space with $R_{i+1}/R_i = 1.167$. Each column is divided into 32 vertical grids. All the simulations are run for 75000 years after which the final snapshots have been taken.

The initial dust size distribution is adopted with the assumption that grain growth starts at the molecular cloud phase and the range of distribution is chosen with minimum particle size $a_{min} = 0.1\mu$m and largest particle size $a_{max} = 10\mu$m. Also, an MRN like power-law with index -3.5 has been used, which makes the initial dust distribution $N(a)\,da \sim a^{-3.5}\,da$. The calculation of the initial number density in each cell is calculated using the formalism of section 4.2.3. The total mass range of dust is divided into 50 equally spaced bins in log space. The collision model implemented includes sticking and fragmentation only, with a fragmenting threshold velocity v_{frag} = 100 cm s^{-1}. The dust particles are assumed to be spherical pure silicate grains. The vertical settling and turbulent stirring algorithm is applied every 1000 years, and the radial drift routine is applied every 5000 years in the course of the simulations.

5.3.1 Viscous Heating

There are essentially two distinct sources of disk heating. The disk can be heated passively by the stellar photons absorbed by the upper layers of the disk. The disk can also be heated actively by the viscous dissipation of the gravitational energy released as a part of the process of accretion. In the previous chapter we included only the stellar photons as the source of disk heating which was modeled by a radiative transfer routine. In this chapter of the dissertation we extend our model to include the viscous heating.

The theory of viscous heating is described in section 2.2.6 in detail. It is possible to include the effect numerically as a part of radiative transfer model by considering photons originating from the disk itself and tracking their path in a Monte Carlo fashion. However, we adopt a more analytical approach to include viscous heating in our work in order to calculate the temperature profile.

To calculate the vertical thermal stratification, we assume that most of the heating due to viscous dissipation occur near the midplane, $z = 0$. The optical depth of the midplane can be approximately stated as $\tau = (1/2)\kappa_R \Sigma(R)$, where κ_R is the Rosseland mean opacity and $\Sigma(R)$ is the total column mass of the disk at a distance R from the central star. We also assume that the column is optically thick with $\tau >> 1$ which is a reasonable approximation as per our findings in chapter 4. Considering that the energy is transported vertically through radiative diffusion, the flux F can be written as

$$F = -\frac{16\sigma T^3}{3\kappa_R \rho}\frac{dT}{dz} \tag{5.10}$$

where $dT/\,dz$ is the vertical temperature gradient and σ is the Stefan-Boltzmann constant. Integrating equation 5.10 gives

$$\int_{T_0}^{T_{visc}(z)} T^3\, dT = -F\frac{3}{16\sigma}\int_0^z \kappa_R \rho(z)\, dz \tag{5.11}$$

which, in the limit $\tau >> 1$ evaluates as

$$\frac{T_0^4}{T_{visc}(z)^4} \approx \frac{3}{4}\tau. \tag{5.12}$$

Using equation 5.12 we can find the temperature associated with viscous heating as a function of height z where T_0 is calculated using equation 2.35 given in section 2.2.6. As the viscous heat is assumed to be fully dissipated at the disk midplane, unlike chapter 4, the opatical depths τ here is calculated towards the surface from the disk midplane. If T_{eff} be the effective disk temperature and T_{irr} is the temperature associated with the passive heating then

$$T_{eff}^4 = T_{visc}^4 + T_{irr}^4. \tag{5.13}$$

Here, we get T_{irr} as the output of the radiative transfer calculation. The final temperature of the disk as a function of R and z is calculated using equation 5.13.

5.3.2 Calculation of New Hydrostatic Equilibrium

The main aspect of this investigation is to calculate the evolving vertical structure of the gas density with the evolving temperature stratification. The equation for vertical hydrostatic equilibrium is

$$\frac{\partial P}{\partial z} = -\rho g_z \tag{5.14}$$

where P is gas pressure and g_z is the vertical component of stellar gravity. With $P = \rho c_s^2$, equation 5.14 becomes

$$\rho \frac{\partial c_s^2}{\partial z} + c_s^2 \frac{\partial \rho}{\partial z} = -\rho g_z. \tag{5.15}$$

This can be further simplified to

$$\frac{\partial \ln \rho}{\partial z} = -S(z), \tag{5.16}$$

where

$$S(z) = -\frac{1}{c_s^2}\left(g_z + \frac{\partial c_s^2}{\partial z}\right). \tag{5.17}$$

Here, $\nabla_z c_s^2 = \partial c_s^2/\partial z$. The sound speed is calculated as $c_s = \sqrt{K_B T_{eff}/\mu m_p}$, where T_{eff} is calculated following the prescription outlined in section 5.3.1. Equation 5.16 is then numerically solved using a second order Runge-Kutta integration routine to calculate the new hydrostatic equilibrium.

5.3.3 Achieving Convergence in Settling & Diffusion

One important aspect of the simulations presented here is to achieve a convergence in the vertical dust distribution. The vertical settling and diffusion of dust particles are implemented following the prescription of section 3.4 in which the Stokes number of the dust particles are calculated using the local gas parameters instead of the midplane gas density. Every time we calculate a new hydrostatic equilibrium in the vertical direction for a particular column, the gas density stratification is altered. This would lead to new values of Stokes number for dust grains changing the strength of coupling between the gas and the dust.

In order to attain a convergence in the vertical dust distribution, the settling and diffusion routine is repeated along with the calculations of hydrostatics equilibrium and radiative transfer. At any particular step and for a particular vertical column, once the new gas density is calculated using the temperature output of the radiative transfer, the settling and diffusion algorithm is run and the temperature is calculated. If the new temperature differ from the previous one by more than a previously set tolerance level, the gas densities are again calculated using the new temperature profile and so on. This process is repeated until a convergence in temperature, dust density and gas density is attained. The tolerance for temperature difference is set a 1 K, which is $\sim 3-5\%$ of the midplane temperature beyond $\sim$ 20 au. In all our simulations, a convergence is obtained within 4 iterations.

5.3.4 A Newer Version of RADMC: RADMC-3D

Unlike the simulations in chapter 4, we have used a newer version of the Monte Carlo radiative transfer code RADMC; RADMC-3D. As described in section 4.4, the code generates a user defined number of photon packets and tracks their movement through scattering and absorption. One inherent drawback of this method is the necessity of tracking each photon absorption or scattering event until the photon escapes the disk through the disk surface. In our disk models, dust settling along with collisional growth increases the optical depth of the midplane, specially in the inner region. Also, our disk models, which are significantly more massive than the MMSN disk are optically thick. While calculating the temperature profile by RADMC-2D, some photons get captured in the optically thick region and suffer a large number of absorption and scattering events before they escape the region. This effect increases the computation time substantially. As a result, out of 10^6 photon packets, a few hundred photons take more than 90% of the computation time.

To avoid this problem, the newer version, RADMC-3D introduced an option of a modified random walk of the photons packets. With this approximation, when a particular packet is trapped in a region with high optical depth, in stead of following all the events suffered by the photons, the corresponding increase in temperature in the particular region is calculated using a semi-analytical approximation. With this added feature, the calculations of passive heating of the disk with 10^7 photons take less than 15 minutes, whereas, RADMC-2D requires more than 3 hours to compute the disk temperature with 10^6 photons. Moreover, RADMC-3D offers a parellel multi-processor version which helps accelerate the process even further.

5.4 Results & Discussion

In this section, we present the results of the simulations performed (Table 5.1) and discuss how dust growth and settling affects the critical mass of a gap-opening planet. We have analyzed our results using four different values for the ratio of the planet to stellar mass q: 10^{-6}, 10^{-5}, 10^{-4} and 10^{-3}. With the stellar mass $M_\star$ =

0.95 $M_\odot$ used in all our simulations, $q = 10^{-3}$ closely corresponds to a Jupiter mass planet, $q = 10^{-4}$ is equivalent to a planet slightly less massive than Saturn and $q = 10^{-5}$ is a planet within the same order of the mass of Neptune. The results presented here are based on the dust distribution obtained at 75000 years.

5.4.1 Variation of h_g with Turbulence Strength α

Figure 5.2 shows the gas scale heights (h_g) as a function of radial distance from the central star, calculated from the new vertical hydrostatic equilibrium. The black dashed line in each sub-figure of Figure 5.2 corresponds to the scale height for an isothermal vertical column. As we have seen in chapter 2, the isothermal assumption for a vertical column provides a Gaussian density stratification, which for an $R^{-3/2}$ variation of surface density, corresponds to an aspect ratio of the disk $h_g(R)/R \sim 0.05$. The scale heights for a settled disk, on the other hand, are smaller compared to the unsettled one. For example, in the disk with $M_{disk} = 0.018$ $M_\odot$ (Figure 5.2 a) the scale height is decreased by more than a factor of 3 for the highest turbulence strength.

The variation of h_g with the turbulence strength is also clearly visible in Figure 5.2. As the value of α decreases, the scale height becomes smaller. h_g for $\alpha = 10^{-5}$ (solid red line) is $3 - 5$ times smaller than that for $\alpha = 10^{-2}$ (solid cyan line). This trend is similar for all the disk models (sub-figures a to d; Figure 5.2) used in our simulations. The aspect ratio of the disk also decreases significantly from the typical isothermal hydrostatic scale heights. The aspect ratio for $\alpha = 10^{-2}$ goes down to 0.02, that for $\alpha = 10^{-4}$ becomes ~ 0.01. $h_g(R)/R$ becomes minimum for $\alpha = 10^{-5}$ which is expected from the settling point of view. For low turbulence strength, the vertical diffusion of dust particles is slow and settling towards the midplane becomes more effective. Moreover, a lower value of α would be beneficial to dust growth and bigger dust grains would settle more rapidly compared to the smaller ones. Due to this combined effect, the overall decrease in midplane temperature is more for lower values of α, a result already confirmed in chapter 4. Hasegawa and Pudritz [2011] reported a 10% reduction in disk scale height due to dust settling. However, their work does not

include the growth and drift of dust grains. Using a more sophisticated model for dust growth, our results from Figure 5.2 shows that the scale heights are reduced by more than 50% in all disk models.

It is important to remark that the scale height is calculated from a hydrostatic equilibrium which is dependent on the vertical temperature gradient, not the temperature itself. Hence, the reduction in scale height is basically controlled by the segregation of the regions near the midplane rather than the total decrease in temperature at the midplane. The more the midplane becomes optically thick at the longer wavelengths, in which the dust grains in the upper layers emit their radiations, the more it contributes to a higher temperature gradient. A lower value of α achieves this in two ways. First, more growth of dust particles ensures that the solid abundance in the upper layers of the disk is reduced, leaving very few small dust grains for absorption of stellar photons. Second, the settling of bigger dust grains, easily achievable with a lower α, confirms that the midplane becomes optically thick. The combined effect of the two processes lead to a higher temperature gradient in the vertical direction for a lower turbulence strength.

5.4.2 The Gap-Opening Condition with q

In Figures 5.3 to 5.6, we have presented our calculation of the gap opening criteria following equation 5.8 [Crida et al., 2006]. The black dashed line in each plot corresponds to $p = 1$ below which a planet will open a gap in the gas disk. Also, in each case the the dashed lines with the same color represent the same condition calculated using an isothermal disk. As can be seen in Figure 5.3, a Jupiter mass planet in an MMSN disk with $M_{disk} = 0.018\ M_\odot$ ($q = 0.001$, sub-figure (d)) will open a gap inside 10 au for α as high as 10^{-2}, which would not be possible without the growth and settling of dust grains (red dashed line). However, beyond 10 au, a lower value of α is required in order for the tidal torque to overcome the viscous effect of the disk. For disks with $M_{disk} = 0.018\ M_\odot$ and above, a gap is possible upto 20 au for the planet with the same mass. It is, however, not possible for a Neptune mass planet ($q = 10^{-5}$)

to open a gap with $\alpha \gtrsim 10^{-4}$, although a gap can be created with $\alpha = 10^{-5}$ (sub-figure (b)). For $q = 10^{-4}$, a gap is not opened for $\alpha = 10^{-3}$ beyond ~ 10 au.

The gap opening radius for the Jupiter mass planet shifts to ~ 20 au for the heavier MMEN disk with $M_{disk} = 0.01\ M_{\odot}$. However, a planet with $q = 10^{-4}$ opens a gap in all disk models for values of α as high as 10^{-3} which is not feasible otherwise. The smallest planet used in our simulations, with $q = 10^{-6}$, produces a small tidal torque relative to the viscous effect and hence can satisfy the gap-opening criteria only for $\alpha = 10^{-5}$ case. We note that, although we expect a magnetic dead zone inside $10 - 15$ au for low turbulence strength, the proposed hydrodynamic turbulence most likely increase the level of turbulence. Hence, $\alpha = 10^{-5}$ is probably not a very realistic value for a protoplanetary disk.

5.4.3 Gap-Opening Criteria Against Disk Mass

In Figure 5.7 we show the effect of the gap-opening condition of equation 5.8 as a function of disk mass for a planet mass similar to that of Saturn, $q = 10^{-4}$. We have used two different values of α; 10^{-2} (Figure 5.7 top) and 10^{-3} (Figure 5.7 bottom) to illustrate the variation. As can be seen, the criterion remains almost independent of the disk mass. For $\alpha = 10^{-2}$ the value of p remains almost same for all four disk models through the entire radial range. The same can be said for $\alpha = 10^{-3}$ case in spite of small differences across the disk masses. This disk mass independence is also noticeable in Figures 5.3 to 5.6 where the gap opening criteria is sensitive to turbulence level but not as much on the disk mass.

A massive disk allows for more growth of dust particles which are subjected to more efficient settling. This effect results into an colder midplane (See chapter 4) compared to a less massive disk. The four sub-figures of Figure 5.2 show that the new gas scale height of the settled disks are not sensitive to disk mass (compare plots of same color in the sub-figures). Hence, it is clear that the tidal part of the gap-opening condition in equation 5.8 is not sensitive to disk mass. The viscous condition, however, depends on the disk viscosity, which in the analytical framework used in this chapter,

is simply $\nu = \alpha c_s h_g$. As the disk temperatures do not change significantly, and the local sound speed $c_s \propto \sqrt{T}$, ν do not change substantially with the disk mass.

5.4.4 Thermal vs Viscous Condition

We end this section by discussing the relative importance of the thermal and viscous gap-opening conditions and how they get affected by the planet masses and turbulence strength. In Figure 5.8 we show the two terms of equation 5.8 separately. The first term, the thermal part, is shown as the black dashed line in each plot. This condition depends on the planets Hill radius and is independent of the value of α. The viscous part, on the other hand, solely depends on α and the corresponding disk viscosity.

As can be seen in Figure 5.8, starting with $q = 10^{-5}$ (sub-figure (a)), the term $a_p(m_p/M_\star)^{1/3}$ increases with the growing planet mass and is maximum for $q = 10^{-3}$. With the increase of the planet mass m_p the strength of the tidal torque becomes higher as the torque is proportional to m_p^2. A heavier planet can remove material from its orbit more easily than a lower mass planet. The viscous torque, however, increases with the value of α and is maximum for $\alpha = 10^{-2}$. Due to the small mass, it is not possible for a Neptune mass planet ($q = 10^{-5}$) to overcome the viscous effect even with $\alpha = 10^{-5}$. A Saturn mass planet can open a gap outside 20 au in a disk with low viscosity (Figure 5.8c). The tidal torque of a Jupiter mass planet with $q = 10^{-3}$, however, can overcome the viscous torque even in a highly turbulent disk.

5.5 Conclusion

In this chapter we have presented the results of 16 global simulations with dust growth and settling using the model developed in chapter 3. We have used four different disk models with varying mass and have adopted four different values of α for each disk. From the results of our simulations our main findings are:

1. The growth and settling and dust grains in a disk alters the hydrostatic equilibrium of a vertical column that reduces the disk scale heights. Depending on

the level of turbulence in the disk, the scale height can be $3 - 8$ times smaller than that of an isothermal disk with Gaussian density stratification. The aspect ratio of the disk can be as low as 0.005, much lower than 0.05, the value adopted widely in literature.

2. Gap opening by a planet becomes relatively easier in a settled disk compared to an unsettled one. A planet with a mass similar to Saturn can open a gap inside $10 - 15$ au of a disk with α as high as 10^{-2}.

3. The gap opening criteria is not sensitive to the disk mass. As the disk mass increases, the angular momentum exchange becomes more efficient increasing the tidal torque. This effect, however, is balanced by the increased accretion rate for a higher mass disk.

It will be truly interesting to run our simulations with the vertically variable α profile and to investigate how that alters the overall disk scale height. Moreover, it is important to understand how a more realistic turbulence profile alters the gap-opening criteria for planets with different masses. As we are currently working on improving our dust model with the inclusion of icy gain compositions and disk winds, which we believe would have big impacts on the turbulence profile, we leave these investigations for the future.

Table 5.1. Simulations Performed

Simulation Name	Σ_0 g cm^{-2}	α	v_{frag} cm s^{-1}	$M_{disk}/M_\star$
A1	1700	10^{-2}	100	0.018
A2	1700	10^{-3}	100	0.018
A3	1700	10^{-4}	100	0.018
A4	1700	10^{-5}	100	0.018
B1	4400	10^{-2}	100	0.04
B2	4400	10^{-3}	100	0.04
B3	4400	10^{-4}	100	0.04
B4	4400	10^{-5}	100	0.04
C1	7200	10^{-2}	100	0.07
C2	7200	10^{-3}	100	0.07
C3	7200	10^{-4}	100	0.07
C4	7200	10^{-5}	100	0.07
D1	9900	10^{-2}	100	0.1
D2	9900	10^{-3}	100	0.1
D3	9900	10^{-4}	100	0.1
D4	9900	10^{-5}	100	0.1

Note. — Simulation set: Four different disk surface density profiles with $\alpha = 10^{-2}$, 10^{-3}, 10^{-4} and 10^{-5}.

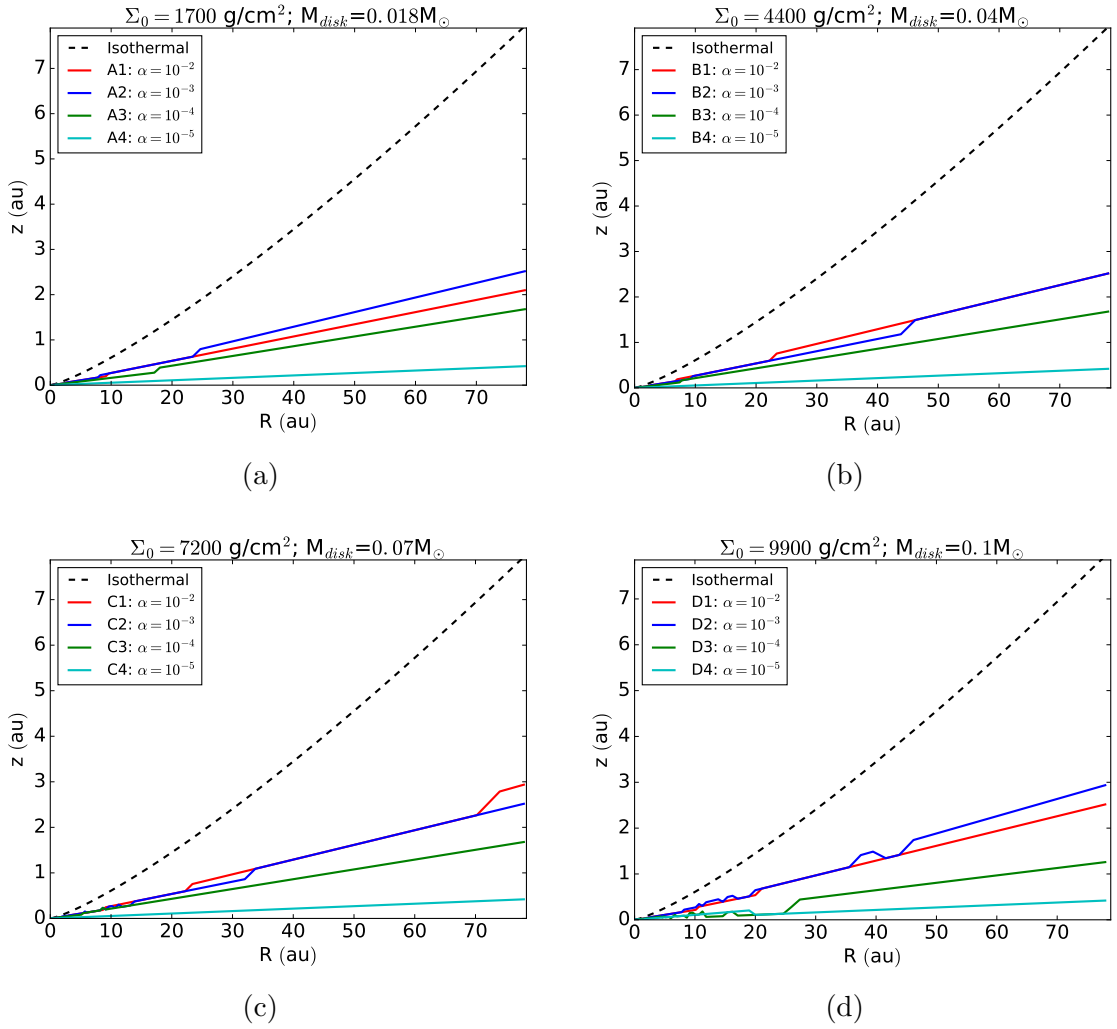

Figure 5.2: The variation of gas scale height as a function of radial distance R. The black dashed line is the scale height from the isothermal disk approximation which generates a Gaussian vertical density stratification. The new scale heights after the altered hydrostatic equilibrium become significantly lower as the turbulence in the disk becomes weaker. The aspect ratio, which for $\alpha = 10^{-2}$ is ~ 0.02, becomes as small as 0.005 for $\alpha = 10^{-5}$.

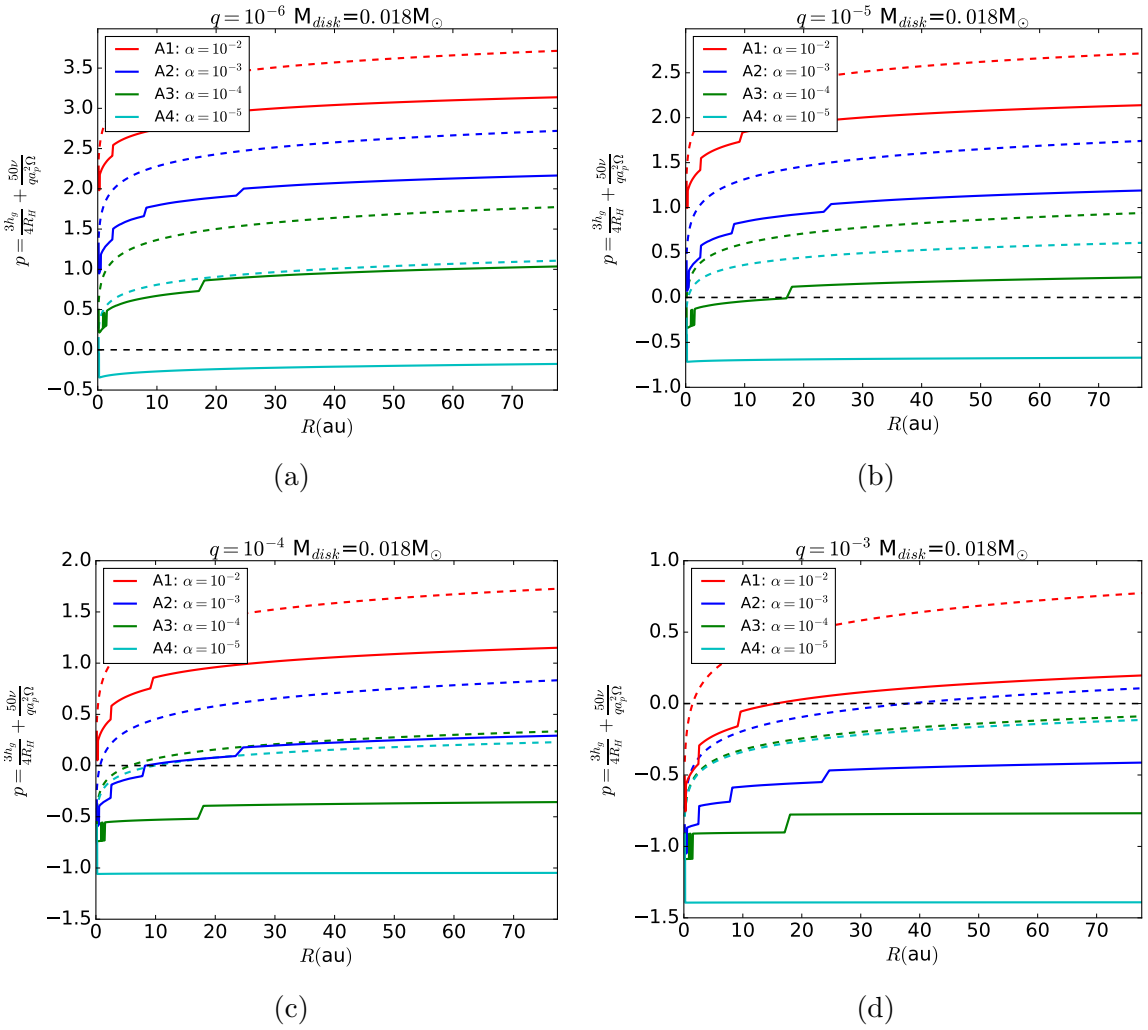

Figure 5.3: The gap-opening condition from equation 5.8 as a function of R and α for disk mass $M_{disk} = 0.018\ M_\odot$. A dashed line with the same color corresponds to p calculated for an isothermal disk.

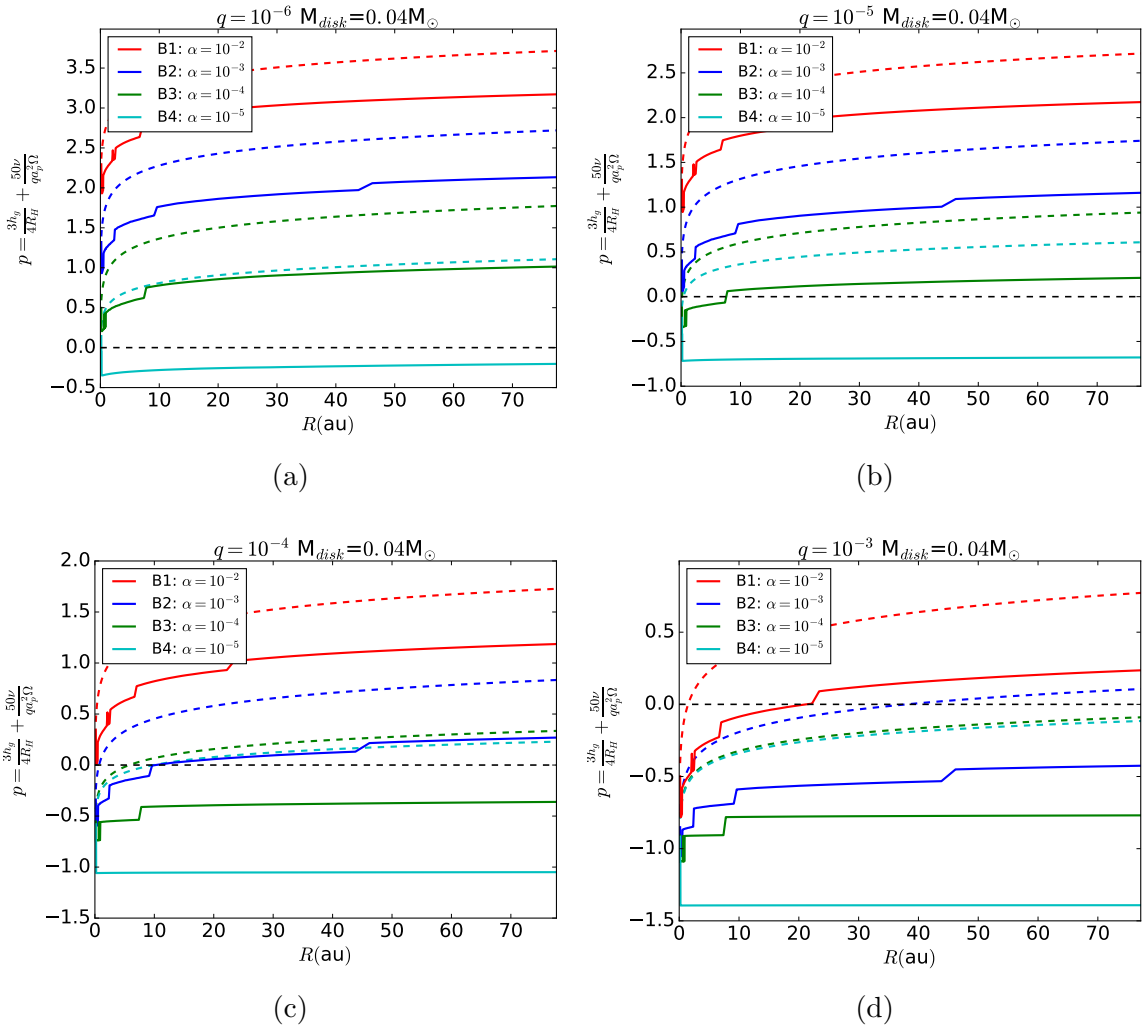

Figure 5.4: The gap-opening condition from equation 5.8 as a function of R and α for disk mass $M_{disk} = 0.04$ $M_\odot$ (Similar to Figure 5.3).

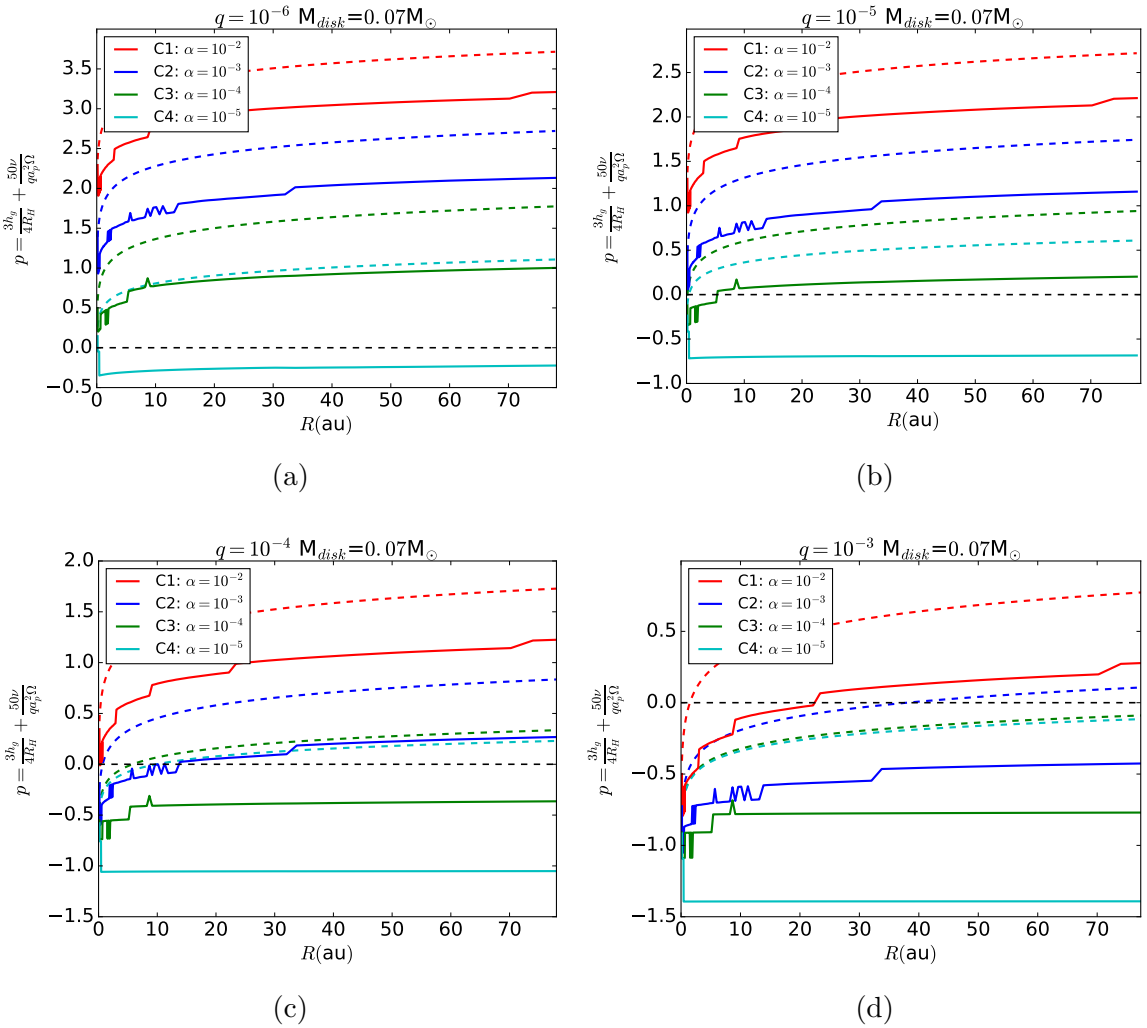

Figure 5.5: The gap-opening condition from equation 5.8 as a function of R and α for disk mass $M_{disk} = 0.07\ M_\odot$ (Similar to Figure 5.3).

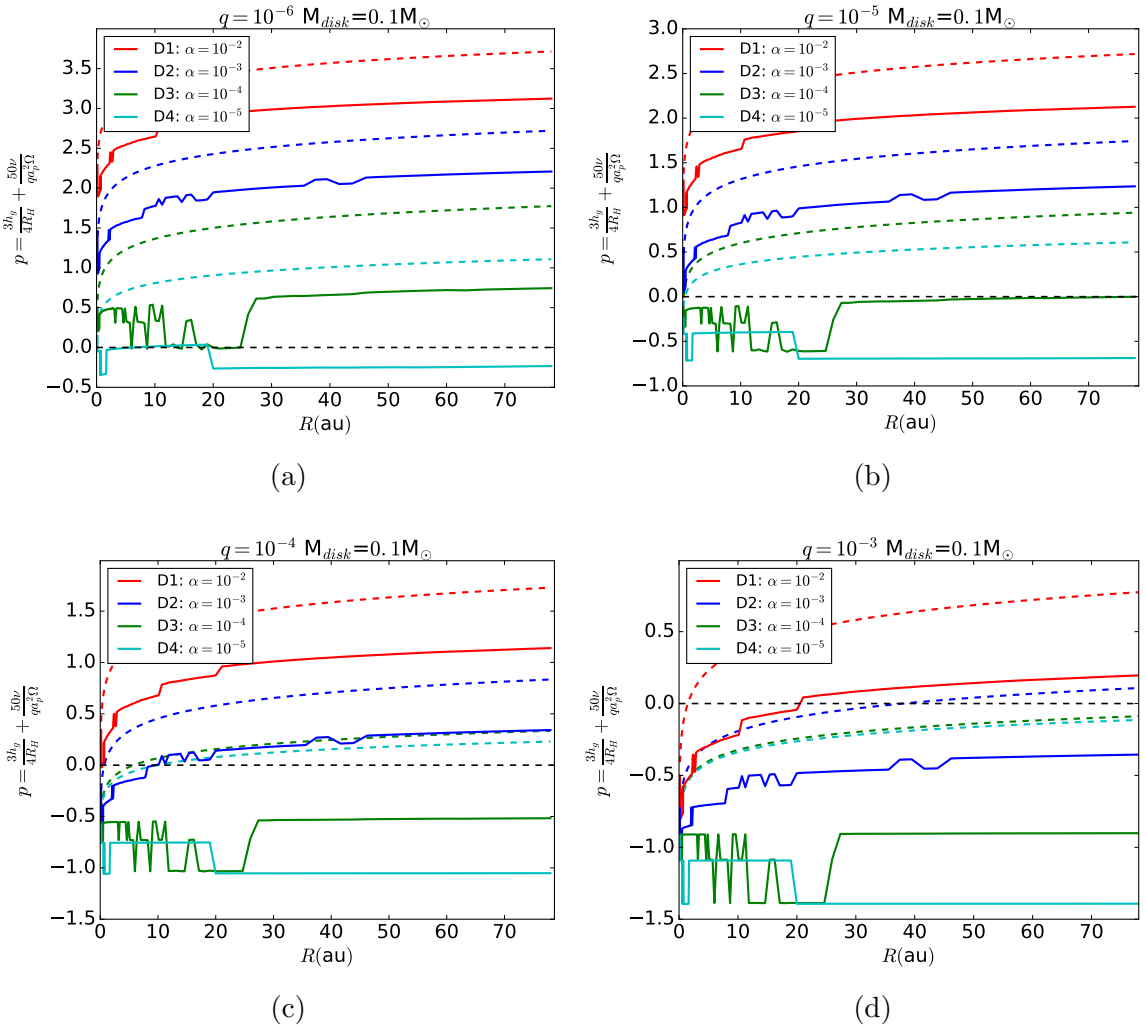

Figure 5.6: The gap-opening condition from equation 5.8 as a function of R and α for disk mass M_{disk} = 0.1 $M_\odot$ (Similar to Figure 5.3). This disk is same as the MMEN disk model used for simulations in chapter 4.

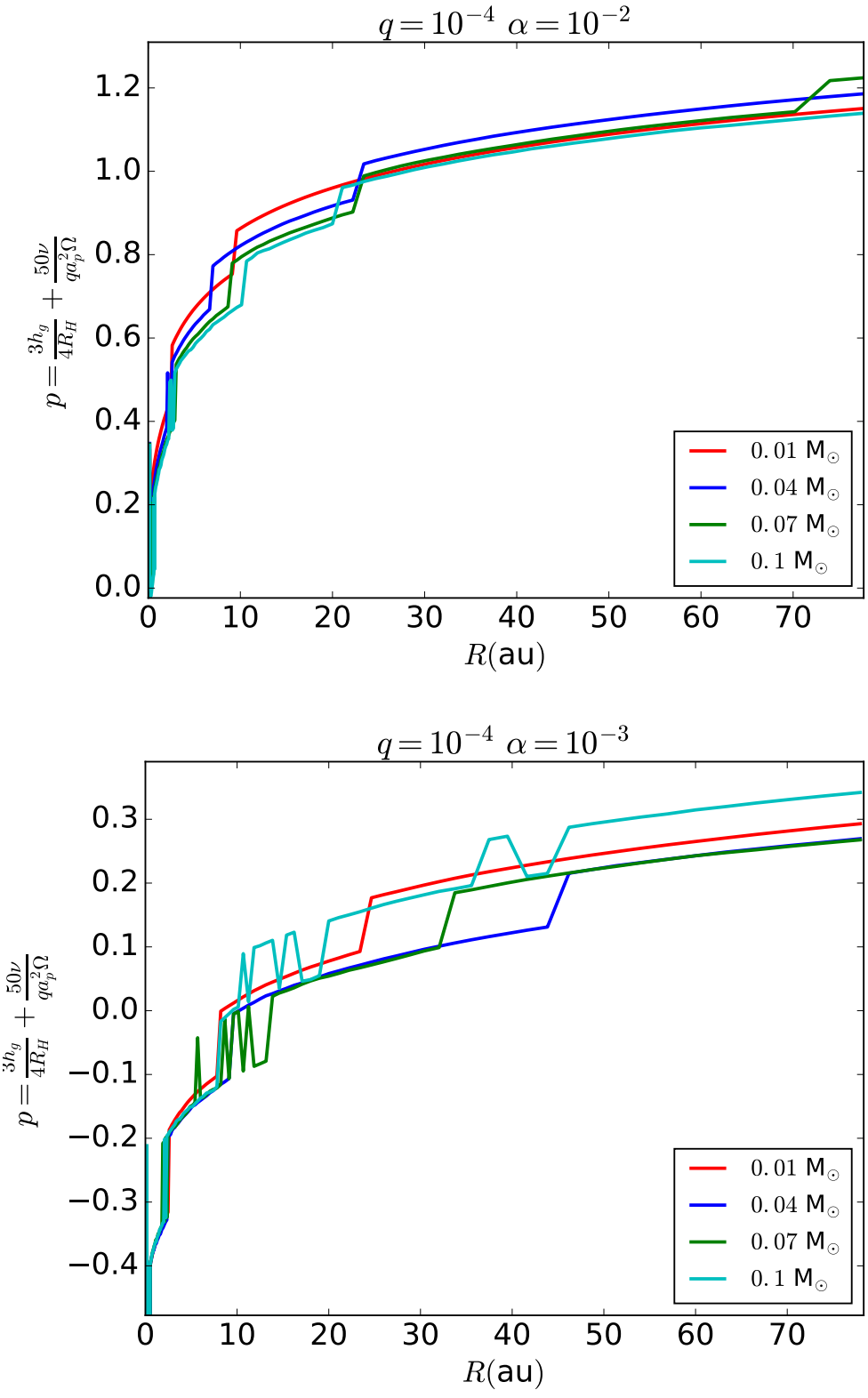

Figure 5.7: The condition p calculated for $q = 10^{-4}$ (a Saturn mass planet) for $\alpha = 10^{-2}$ (top) and 10^{-3} (bottom) for disks with different masses. The gap opening condition is not sensitive to the disk mass and remains fairly steady through the full radial extent.

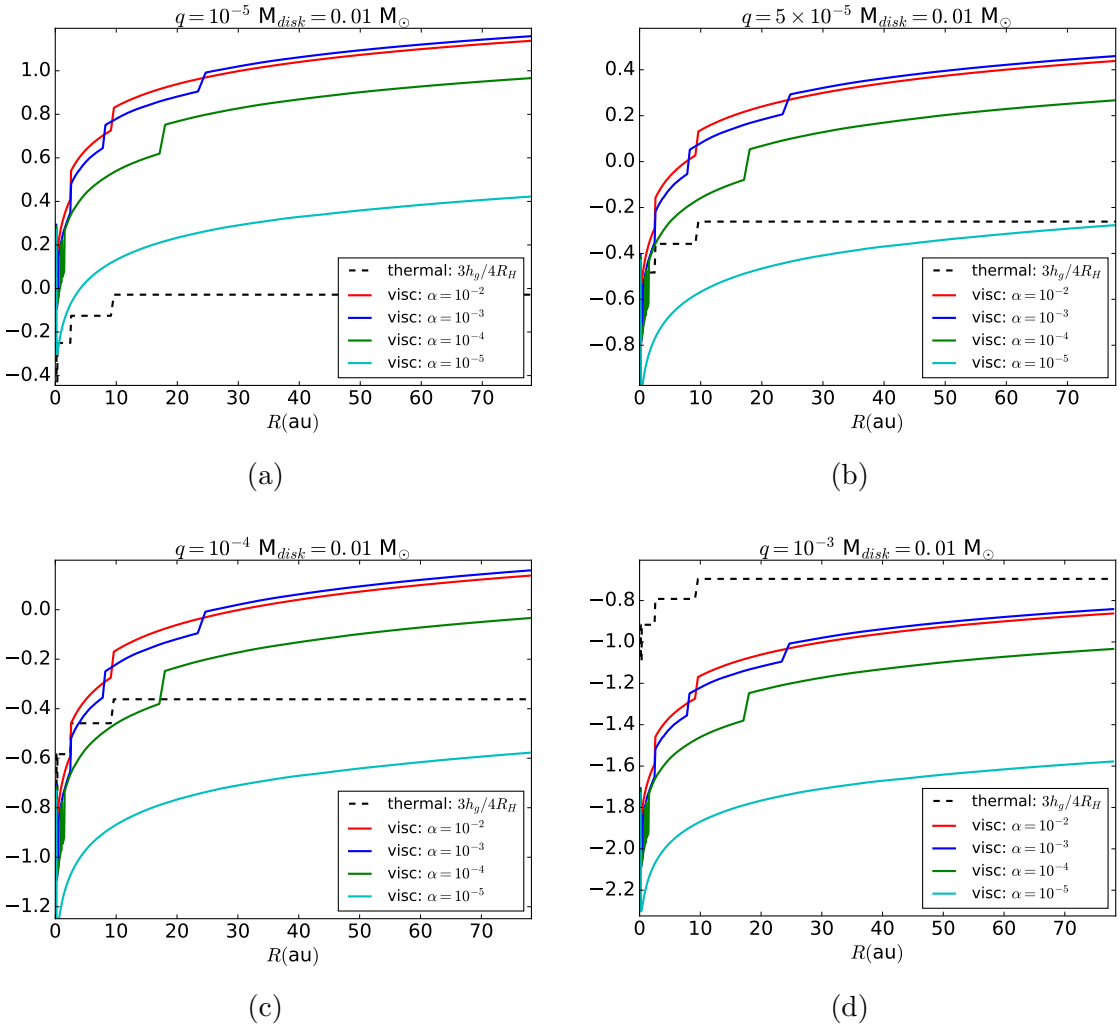

Figure 5.8: A comparison of relative strength of thermal and viscous conditions for gap opening for an MMSN disk model with four different planet masses. As the mass of the planet increases, the tidal torque becomes larger and for $q = 10^{-3}$ the torque becomes significant to compete against the viscous effect for a highly turbulent disk (Sub-figure (d))

Chapter 6

CONCLUSION & FUTURE DIRECTIONS

In this dissertation titled "Planet Formation in a Dusty Disk: Effect of Collisional Dust Growth & Dynamics", we have developed a new weighted Monte Carlo model of collisional dust growth along with a Monte Carlo Lagrangian prescription for settling, and turbulent stirring, combined with wavelength dependent opacity calculations and radiative transfer. The dust growth model includes sticking and fragmentation, and the radiative transfer is performed using the publicly available code RADMC-2D/3D. The monochromatic opacity calculations are performed following the *Utilitarian Opacity Model* by Cuzzi et al. [2014].

To implemented our model, we have developed a massively parallel code in FORTRAN 95/03 with a *python* wrapper to setup the user interface and code compilation. In order to use the computational resource in a more efficient way, we have developed a *flagged parallelization routine* and designed the code in a modular form for a comprehensive user interface. Our model and code is fast and efficient due to the linear nature of the Monte Carlo algorithm, compared to Monte Carlo methods existing in the literature. Our code can finish a single global simulation in $3-5$ days depending on the disk models compared to a few weeks time for existing methods.

As an application to the dust model, we have first presented a total of 11 global simulation with three different disk masses: Minimum Mass Solar Nebula (MMSN), Minimum Mass Extra-solar Nebula (MMEN) and a heavy disk model. In all cases, we have used a $-3/2$ power-law surface density profile and the respective disk masses are $0.018M_{\odot}$, $0.12M_{\odot}$ and $0.18M_{\odot}$. From the results of these simulations we have found that irrespective of the disk model used the collisional dust growth reduces the opacity at the disk midplane at shorter wavelengths by 3-4 orders of magnitude and

the opacities at mm/sub-mm wavelengths increase. The opacities at the disk surface layers, however, decreases throughout, mostly due to inefficient growth of dust particles in these regions and the reduction in dust abundance due to dust settling. This effect is also dependent on the level of turbulence strength. For example, dust in a disk with $\alpha = 10^{-5}$ settle more efficiently compared to a disk with $\alpha = 10^{-3}$ where dust settling is mitigated by the efficient vertical stirring by disk turbulence.

We have also explored the evolving optical depth τ of the disk calculated by integrating the monochromatic opacities from the disk surface to the midplane. Our simulations have found that the optical depth at wavelengths $\lambda \leq 10\mu$m are reduced due to dust growth and settling and that in the mm/sub-mm wavelength regime it increases by at least an order of magnitude or more depending on the disk model. For the MMEN and the heavy disk model τ is always greater than 10 inside of 30 au making it difficult to observationally probe the disk midplane through observations. This will pose a problem in inferring the disk mass from (sub)millimeter observations.

In our set of simulations with the MMEN disk model we have used two different fragmentation threshold velocities for the dust particles; 50 cm s^{-1} and 100 cm s^{-1}. We have found that the final steady state size distributions differ significantly when different values for fragmenting velocities (v_{frag}) are adopted. With increasing values of v_{frag}, the size of the largest particle increases and more mass gets transferred to the higher end of the particle size distribution, leaving less mass for the smaller micron and sub-micron size dust grains. As smaller grains provide the maximum surface area for photon absorption, and hence make the largest contributions to disk opacities, the optical properties of the disk are sensitive to the value of v_{frag} chosen for simulated models. We have found that the opacities at the smaller wavelengths are upto an order of magnitude less for $v_{frag} = 100$ cm s^{-1} compared to simulations using $v_{frag} =$ 50 cm s^{-1} cases. In all our simulations we have assumed only silicate grains for which v_{frag} lies anywhere between $20 - 190$ cm s^{-1} according to the laboratory experiments. For icy grains, however, the fragmentation velocity can reach upto 5 m s^{-1} which would lower the disk opacities even further.

In our simulations, once a pair of particles collide with a relative velocity greater than the fragmenting threshold velocity, the fragments are distributed in a power-law distribution which extends all the way to monomer size particles in the lower size limit. The size of the largest fragment for such events, however, is still a matter of active debate. From several laboratory experiments, it has been found that the largest mass of the fragment should follow a power-law in the collision velocity and it would be smaller for a more catastrophic collision. In some works the mass of the largest fragment is chosen to be the same as the target mass, and the total mass of the target and projectile is distributed through the full range of fragment masses. This is the approach that we have adopted in our model. We, however, have found that the shape of the final steady state size distribution is not sensitive to the adopted fragmentation model. Moreover, differences are even less insignificant when vertical settling and turbulent diffusion is included. Our simulations have pointed out that it is the composition of dust particles rather than the fine details of collision physics that affects the final dust size distribution and spatial abundance of solids.

In addition to the above points, our simulations have revealed that dust growth and settling can cause a small but detectable reduction in the Toomre-Q parameter, a measure of a disk's stability against self-gravity. Due to growth, bigger particles can settle more efficiently towards the disk midplane, leaving only a small fraction of total dust mass in the upper layers of the disk. The absorption of stellar photons then becomes less efficient and the disk midplane becomes cooler. As a result, the value of the Toomre-Q decreases in the midplane. We have found a reduction in Q by $0.3 - 0.4$ from the initial value for both the MMEN and Heavy disk model. Also, this reduction makes the Heavy disk, which was initially marginally stable, unstable by bringing Q below 1.4, the threshold for gravitational instability. However, it is important to note that, the said instability in the disk is a necessary, but not a sufficient condition, for forming giant planets or sub-stellar companions through gravitational fragmentation. A value for Q less than 1.4 can lead to a steady gravo-turbulent state or sustaining spiral structure depending on the complex radiative feedback of the disk.

6.1 Plans for Work in the Immediate Future

Modeling dust growth through collisional sticking and fragmentation ranging over several decades in mass, in a protoplanetary disk ranging several hundreds of au, is a mammoth task. We have invested a significant amount of effort in the past few years to build an efficient theoretical and numerical model as a part of this dissertation. However, there are still a number of directions in which our work can be extended by adding more physics and enhancing the fidelity of our model. As an immediate extension of our dust model we have already started working on two different projects which would help us understand the complex interplay of different processes in the disk even better.

A time varying turbulence profile: So far, in all our simulations with a variable turbulence profile we have kept the value of α calculated at $t = 0$ fixed over the course of our simulations. However, we have seen that the turbulence profile calculated from the ionization-recombination balance using a chemical network depends on the local dust abundance and the dust size distribution. As a result, it is not very physical to assume a temporally static α calculated at $t = 0$ as the steady state dust size distribution is significantly different from the initial distribution.

We are currently running a series of simulations to compute the detailed vertical structure with time varying turbulence profile. We have selected three vertical columns at a distance 1, 3 and 10 au from the central star. The simulations are started with the usual MRN size distribution and the same chemical network of chapter 4 is being used. In this work, we have made a look-up table for Ohmic, ambipolar and Hall diffusivities as a function of dust abundance, gas density, temperature and ionization fraction. In order to gain computational efficiency, the turbulence profile of each vertical column is updated using these look-up tables instead of running the chemical models dynamically. We are also performing a parameter study on the metallicity (dust to gas mass ratio) of the disk and the midplane plasma β, a measure of strength of the magnetic fields. Recent research has revealed that chondrules in the Semarkona meteorites were formed in a protoplanetary nebula with a magnetic field strength of $\sim 50\mu$T. We shall use

magnetic fields of this order. Through this work, we would like to investigate the effect of turbulence on the efficiency of planet formation at the midplane. Also, we would like to see the temporal variation of the height of the magnetic dead-zone. It has also been proposed recently that the upper boundary of the dead zone is basically at the $\tau = 1$ surface. We expect to confirm this proposal through this work. Moreover, the evolution of the gas dispersion velocity at the midplane, which has direct impact on the growth of dust particles, will be on the list of our special interests.

Including collisions of icy dust grains: Our model and code already include a detailed temperature calculation which is performed by a radiative transfer method for passive heating by stellar photons. The viscous heating is included using an optical depth technique in an analytical way as a part of post-processing. Our computation of the thermal profile gives us the temperature of the disk as a function of radial distance (R) and height above the midplane (z). Collisions of non-icy silicate grains differ from that of icy bodies in the fragmenting threshold velocity and power-law index of fragmentation products. So, it is straight forward to implement icy collisions by only changing the value of v_{frag} and the respective power-law index. Our new model will check the temperature of the cell before assigning the job to a particular processor, and depending on the temperature, the values for the particular parameters will be provided. For cell temperature less than 160 K, ice collisions will be implemented. In addition, our plan also includes the modeling of ice melting inside the snow line and the enhancement of gas pressure at those regions. However, the specific physical model for implementation of snow-line is yet to be finalized.

6.2 Long Term plans

The field of planet formation and disk evolution is moving fast. With the increased observing power of both ground and space based telescope, we are at a position to probe these astrophysical objects with greater details. Moreover, the James Webb Space Telescope (JWST), due to be launched in 2021, and the proposed ground based

Next Generation Very Large Array (ngVLA) will enable us with unprecedented resolution. To enhance the scientific outcomes of these observations it is imperative that the theorists come up with state-of-the-art models with high fidelity, achieving which is our long term goal with our current dust model.

Adding gas dynamics: Our model so far contains only dust physics on a static gas background. This can be justified by the fact that we run our simulations for timescales which are shorter compared to the gas diffusion timescale. However, to simulate protoplanetary nebulae for million years timescales, it is important to add the gas dynamics to our model. The initial idea is to model the gas evolution in a 1D format utilizing the theory described in chapter 2. The dust dynamics in the disk is affected by the gas through a drag force. The gas, on the other hand, is affected by the solid particles through their optical and thermodynamic properties. Including these effects will bring our simulations closer to the real picture where the simulation results can be used as a template to test against the observations with reasonable confidence.

Once the gas dynamics is included in the model, natural extensions would be to add mass loss through disk winds and implementing a more advanced chemical model. Disk winds have been proposed as an alternative to turbulence to solve the puzzle of angular momentum transport. As we have already seen through our global simulations, small dust grains are almost always present in the upper layers of the disk. In the presence of a disk wind, dust grains from the disk surface can escape the disk, resulting in a very different dust stratification. This effect will most likely change the optical depths of the disk and hence, its observational appearance.

On the spectroscopic side, the output of the global simulations can be post-processed by a chemical network involving species, such as H, He, C, Ne, S, Mg, Fe, Si and Ar, along with photo-dissociation and photo-ionization by EUV, FUV, X-ray photons and cosmic rays. According to the existing chemical models, the gas is primarily heated by X-rays, grain photoelectric heating by polycyclic aromatic hydrocarbons (PAH), cosmic rays, exothermic chemical reactions, collisional de-excitation of vibrationally excited H_2 by FUV, formation heating by H_2, collisions with warmer dust

grains and photo-ionization of carbon. The gas cools predominantly due to line emission and collisions with cooler dust grains. With the output from the chemical models, the non-LTE spectral line radiative transfer code can give us reliable synthetic spectra.

Bibliography

S. M. Andrews, K. A. Rosenfeld, A. L. Kraus, and D. J. Wilner. The Mass Dependence between Protoplanetary Disks and their Stellar Hosts. ApJ, 771:129, July 2013. doi: 10.1088/0004-637X/771/2/129.

M. Ansdell, J. P. Williams, N. van der Marel, J. M. Carpenter, G. Guidi, M. Hogerheijde, G. S. Mathews, C. F. Manara, A. Miotello, A. Natta, I. Oliveira, M. Tazzari, L. Testi, E. F. van Dishoeck, and S. E. van Terwisga. ALMA Survey of Lupus Protoplanetary Disks. I. Dust and Gas Masses. ApJ, 828:46, September 2016. doi: 10.3847/0004-637X/828/1/46.

P. J. Armitage. Massive Planet Migration: Theoretical Predictions and Comparison with Observations. ApJ, 665:1381–1390, August 2007. doi: 10.1086/519921.

P. J. Armitage. Dynamics of Protoplanetary Disks. ARA&A, 49:195–236, September 2011. doi: 10.1146/annurev-astro-081710-102521.

H. Baehr, H. Klahr, and K. M. Kratter. The Fragmentation Criteria in Local Vertically Stratified Self-gravitating Disk Simulations. ApJ, 848:40, October 2017. doi: 10.3847/1538-4357/aa8a66.

X.-N. Bai. The Role of Tiny Grains on the Accretion Process in Protoplanetary Disks. ApJ, 739:51, September 2011. doi: 10.1088/0004-637X/739/1/51.

X.-N. Bai. Towards a Global Evolutionary Model of Protoplanetary Disks. ApJ, 821:80, April 2016. doi: 10.3847/0004-637X/821/2/80.

X.-N. Bai. Global Simulations of the Inner Regions of Protoplanetary Disks with Comprehensive Disk Microphysics. ApJ, 845:75, August 2017. doi: 10.3847/1538-4357/aa7dda.

S. A. Balbus and J. F. Hawley. A powerful local shear instability in weakly magnetized disks. I - Linear analysis. II - Nonlinear evolution. ApJ, 376:214–233, July 1991. doi: 10.1086/170270.

C. Baruteau, A. Crida, S.-J. Paardekooper, F. Masset, J. Guilet, B. Bitsch, R. Nelson, W. Kley, and J. Papaloizou. Planet-Disk Interactions and Early Evolution of Planetary Systems. *Protostars and Planets VI*, pages 667–689, 2014. doi: 10.2458/azu_uapress_9780816531240-ch029.

E. A. Bergin, L. I. Cleeves, U. Gorti, K. Zhang, G. A. Blake, J. D. Green, S. M. Andrews, N. J. Evans, II, T. Henning, K. Öberg, K. Pontoppidan, C. Qi, C. Salyk, and E. F. van Dishoeck. An old disk still capable of forming a planetary system. Nature, 493:644–646, January 2013. doi: 10.1038/nature11805.

T. Birnstiel, C. P. Dullemond, and F. Brauer. Dust retention in protoplanetary disks. A&A, 503:L5–L8, August 2009. doi: 10.1051/0004-6361/200912452.

T. Birnstiel, C. P. Dullemond, and F. Brauer. Gas- and dust evolution in protoplanetary disks. A&A, 513:A79, April 2010. doi: 10.1051/0004-6361/200913731.

T. Birnstiel, C. W. Ormel, and C. P. Dullemond. Dust size distributions in coagulation/fragmentation equilibrium: numerical solutions and analytical fits. A&A, 525: A11, January 2011. doi: 10.1051/0004-6361/201015228.

J. E. Bjorkman and K. Wood. Radiative Equilibrium and Temperature Correction in Monte Carlo Radiation Transfer. ApJ, 554:615–623, June 2001. doi: 10.1086/321336.

J. Blum and G. Wurm. Experiments on Sticking, Restructuring, and Fragmentation of Preplanetary Dust Aggregates. Icarus, 143:138–146, January 2000. doi: 10.1006/icar.1999.6234.

A. C. Boley, A. C. Mejía, R. H. Durisen, K. Cai, M. K. Pickett, and P. D'Alessio. The Thermal Regulation of Gravitational Instabilities in Protoplanetary Disks. III. Simulations with Radiative Cooling and Realistic Opacities. ApJ, 651:517–534, November 2006. doi: 10.1086/507478.

A. C. Boley, T. Hayfield, L. Mayer, and R. H. Durisen. Clumps in the outer disk by disk instability: Why they are initially gas giants and the legacy of disruption. Icarus, 207:509–516, June 2010. doi: 10.1016/j.icarus.2010.01.015.

A. P. Boss. Giant planet formation by gravitational instability. *Science*, 276:1836–1839, 1997. doi: 10.1126/science.276.5320.1836.

F. Brauer, C. P. Dullemond, and Th. Henning. Coagulation, fragmentation and radial motion of solid particles in protoplanetary disks. A&A, 480:859–877, March 2008. doi: 10.1051/0004-6361:20077759.

K. Cai, R. H. Durisen, S. Michael, A. C. Boley, A. C. Mejía, M. K. Pickett, and P. D'Alessio. The Effects of Metallicity and Grain Size on Gravitational Instabilities in Protoplanetary Disks. ApJ, 636:L149–L152, January 2006. doi: 10.1086/500083.

S. Charnoz, L. Fouchet, J. Aleon, and M. Moreira. Three-dimensional Lagrangian Turbulent Diffusion of Dust Grains in a Protoplanetary Disk: Method and First Applications. ApJ, 737:33, August 2011. doi: 10.1088/0004-637X/737/1/33.

S. Chatterjee, E. B. Ford, S. Matsumura, and F. A. Rasio. Dynamical Outcomes of Planet-Planet Scattering. ApJ, 686:580–602, October 2008. doi: 10.1086/590227.

E. Chiang and G. Laughlin. The minimum-mass extrasolar nebula: in situ formation of close-in super-Earths. MNRAS, 431:3444–3455, June 2013. doi: 10.1093/mnras/stt424.

E. Chiang and R. Murray-Clay. Inside-out evacuation of transitional protoplanetary discs by the magneto-rotational instability. *Nature Physics*, 3:604–608, September 2007. doi: 10.1038/nphys661.

E. I. Chiang and P. Goldreich. Spectral Energy Distributions of T Tauri Stars with Passive Circumstellar Disks. ApJ, 490:368–376, November 1997. doi: 10.1086/304869.

H.-F. Chiang, L. W. Looney, and J. J. Tobin. The Envelope and Embedded Disk around the Class 0 Protostar L1157-mm: Dual-wavelength Interferometric Observations and Modeling. ApJ, 756:168, September 2012. doi: 10.1088/0004-637X/756/2/168.

F. J. Ciesla and J. N. Cuzzi. The evolution of the water distribution in a viscous protoplanetary disk. Icarus, 181:178–204, March 2006. doi: 10.1016/j.icarus.2005.11.009.

P. Cossins, G. Lodato, and C. J. Clarke. Characterizing the gravitational instability in cooling accretion discs. MNRAS, 393:1157–1173, March 2009. doi: 10.1111/j.1365-2966.2008.14275.x.

P. Cossins, G. Lodato, and C. Clarke. The effects of opacity on gravitational stability in protoplanetary discs. MNRAS, 401:2587–2598, February 2010. doi: 10.1111/j.1365-2966.2009.15835.x.

E. G. Cox, R. J. Harris, L. W. Looney, D. M. Segura-Cox, J. Tobin, Z.-Y. Li, Ł. Tychoniec, C. J. Chandler, M. M. Dunham, K. Kratter, C. Melis, L. M. Perez, and S. I. Sadavoy. High-resolution 8 mm and 1 cm Polarization of IRAS 4A from the VLA Nascent Disk and Multiplicity (VANDAM) Survey. ApJ, 814:L28, December 2015. doi: 10.1088/2041-8205/814/2/L28.

A. Crida, A. Morbidelli, and F. Masset. On the width and shape of gaps in protoplanetary disks. Icarus, 181:587–604, April 2006. doi: 10.1016/j.icarus.2005.10.007.

J. N. Cuzzi, P. R. Estrada, and S. S. Davis. Utilitarian Opacity Model for Aggregate Particles in Protoplanetary Nebulae and Exoplanet Atmospheres. ApJS, 210:21, February 2014. doi: 10.1088/0067-0049/210/2/21.

Jeffrey N. Cuzzi, Sanford S. Davis, and Anthony R. Dobrovolskis. Blowing in the wind. II. Creation and redistribution of refractory inclusions in a turbulent protoplanetary nebula. Icarus, 166:385–402, December 2003. doi: 10.1016/j.icarus.2003.08.016.

G. D'Angelo, W. Kley, and T. Henning. Migration and Accretion of Protoplanets in 2D and 3D Global Hydrodynamical Simulations. In D. Deming and S. Seager, editors, *Scientific Frontiers in Research on Extrasolar Planets*, volume 294 of *Astronomical Society of the Pacific Conference Series*, pages 323–326, 2003.

J. Deckers and J. Teiser. Collisions of solid ice in planetesimal formation. MNRAS, 456:4328–4334, March 2016. doi: 10.1093/mnras/stv2952.

J. Dobinson, Z. M. Leinhardt, S. Lines, P. J. Carter, S. E. Dodson-Robinson, and N. A. Teanby. Hiding in the Shadows. II. Collisional Dust as Exoplanet Markers. ApJ, 820:29, March 2016. doi: 10.3847/0004-637X/820/1/29.

J. Drążkowska, F. Windmark, and C. P. Dullemond. Planetesimal formation via sweep-up growth at the inner edge of dead zones. A&A, 556:A37, August 2013. doi: 10.1051/0004-6361/201321566.

J. Drążkowska, F. Windmark, and C. P. Dullemond. Modeling dust growth in protoplanetary disks: The breakthrough case. A&A, 567:A38, July 2014. doi: 10.1051/0004-6361/201423708.

B. Dubrulle, G. Morfill, and M. Sterzik. The dust subdisk in the protoplanetary nebula. Icarus, 114:237–246, April 1995. doi: 10.1006/icar.1995.1058.

C. P. Dullemond and C. Dominik. The effect of dust settling on the appearance of protoplanetary disks. A&A, 421:1075–1086, July 2004. doi: 10.1051/0004-6361:20040284.

C. P. Dullemond, D. Hollenbach, I. Kamp, and P. D'Alessio. Models of the Structure and Evolution of Protoplanetary Disks. *Protostars and Planets V*, pages 555–572, 2007.

M. L. Enoch, N. J. Evans, II, A. I. Sargent, and J. Glenn. Properties of the Youngest Protostars in Perseus, Serpens, and Ophiuchus. ApJ, 692:973–997, February 2009. doi: 10.1088/0004-637X/692/2/973.

P. R. Estrada and J. N. Cuzzi. Solving the Coagulation Equation by the Moments Method. ApJ, 682:515–526, July 2008. doi: 10.1086/589685.

Paul R. Estrada, Jeffrey N. Cuzzi, and Demitri A. Morgan. Global Modeling of Nebulae with Particle Growth, Drift, and Evaporation Fronts. I. Methodology and Typical Results. ApJ, 818:200, February 2016. doi: 10.3847/0004-637X/818/2/200.

S. Fromang and J. Papaloizou. Dust settling in local simulations of turbulent protoplanetary disks. A&A, 452:751–762, June 2006. doi: 10.1051/0004-6361:20054612.

C. F. Gammie. Layered Accretion in T Tauri Disks. ApJ, 457:355, January 1996. doi: 10.1086/176735.

C. F. Gammie. Nonlinear Outcome of Gravitational Instability in Cooling, Gaseous Disks. ApJ, 553:174–183, May 2001. doi: 10.1086/320631.

P. Garaud. Growth and Migration of Solids in Evolving Protostellar Disks. I. Methods and Analytical Tests. ApJ, 671:2091–2114, December 2007. doi: 10.1086/523090.

Daniel T. Gillespie. An exact method for numerically simulating the stochastic coalescence process in a cloud. *Journal of the Atmospheric Sciences*, 32(10):1977–1989, 1975. doi: 10.1175/1520-0469(1975)032⟨1977:AEMFNS⟩2.0.CO;2.

P. Goldreich and S. Tremaine. The excitation of density waves at the Lindblad and corotation resonances by an external potential. ApJ, 233:857–871, November 1979. doi: 10.1086/157448.

P. Goldreich and S. Tremaine. Disk-satellite interactions. ApJ, 241:425–441, October 1980. doi: 10.1086/158356.

K. Gullikson, A. Kraus, and S. Dodson-Robinson. The Close Companion Mass-ratio Distribution of Intermediate-mass Stars. AJ, 152:40, August 2016. doi: 10.3847/0004-6256/152/2/40.

C. Güttler, J. Blum, A. Zsom, C. W. Ormel, and C. P. Dullemond. The outcome of protoplanetary dust growth: pebbles, boulders, or planetesimals?. I. Mapping the zoo of laboratory collision experiments. A&A, 513:A56, April 2010. doi: 10.1051/0004-6361/200912852.

J. M. Hahn and R. Malhotra. Orbital Evolution of Planets Embedded in a Planetesimal Disk. AJ, 117:3041–3053, June 1999. doi: 10.1086/300891.

L. Hartmann, N. Calvet, E. Gullbring, and P. D'Alessio. Accretion and the Evolution of T Tauri Disks. ApJ, 495:385–400, March 1998. doi: 10.1086/305277.

Y. Hasegawa and R. E. Pudritz. Dead Zones as Thermal Barriers to Rapid Planetary Migration in Protoplanetary Disks. ApJ, 710:L167–L171, February 2010. doi: 10.1088/2041-8205/710/2/L167.

Y. Hasegawa and R. E. Pudritz. Dust settling and rapid planetary migration. MNRAS, 413:286–300, May 2011. doi: 10.1111/j.1365-2966.2010.18135.x.

Y. Hasegawa, S. Okuzumi, M. Flock, and N. J. Turner. Magnetically Induced Disk Winds and Transport in the HL Tau Disk. ApJ, 845:31, August 2017. doi: 10.3847/1538-4357/aa7d55.

C. Hayashi. Structure of the Solar Nebula, Growth and Decay of Magnetic Fields and Effects of Magnetic and Turbulent Viscosities on the Nebula. *Progress of Theoretical Physics Supplement*, 70:35–53, 1981. doi: 10.1143/PTPS.70.35.

Anna L. H. Hughes and Philip J. Armitage. Global variation of the dust-to-gas ratio in evolving protoplanetary discs. MNRAS, 423:389–405, June 2012. doi: 10.1111/j.1365-2966.2012.20892.x.

M. Ilgner and R. P. Nelson. On the ionisation fraction in protoplanetary disks. I. Comparing different reaction networks. A&A, 445:205–222, January 2006. doi: 10.1051/0004-6361:20053678.

H. Jang-Condell and D. D. Sasselov. Disk Temperature Variations and Effects on the Snow Line in the Presence of Small Protoplanets. ApJ, 608:497–508, June 2004. doi: 10.1086/392526.

S. Jin, S. Li, A. Isella, H. Li, and J. Ji. Modeling Dust Emission of HL Tau Disk Based on Planet-Disk Interactions. ApJ, 818:76, February 2016. doi: 10.3847/0004-637X/818/1/76.

B. M. Johnson and C. F. Gammie. Nonlinear Outcome of Gravitational Instability in Disks with Realistic Cooling. ApJ, 597:131–141, November 2003. doi: 10.1086/378392.

J. K. Jørgensen, T. L. Bourke, P. C. Myers, J. Di Francesco, E. F. van Dishoeck, C.-F. Lee, N. Ohashi, F. L. Schöier, S. Takakuwa, D. J. Wilner, and Q. Zhang. PROSAC: A Submillimeter Array Survey of Low-Mass Protostars. I. Overview of Program: Envelopes, Disks, Outflows, and Hot Cores. ApJ, 659:479–498, April 2007. doi: 10.1086/512230.

M. Jurić and S. Tremaine. Dynamical Origin of Extrasolar Planet Eccentricity Distribution. ApJ, 686:603–620, October 2008. doi: 10.1086/590047.

M. Kama, M. Min, and C. Dominik. The inner rim structures of protoplanetary discs. A&A, 506:1199–1213, November 2009. doi: 10.1051/0004-6361/200912068.

H. Klahr and A. Hubbard. Convective Overstability in Radially Stratified Accretion Disks under Thermal Relaxation. ApJ, 788:21, June 2014. doi: 10.1088/0004-637X/788/1/21.

W. Kley and R. P. Nelson. Planet-Disk Interaction and Orbital Evolution. ARA&A, 50:211–249, September 2012. doi: 10.1146/annurev-astro-081811-125523.

A. Kolmogorov. The Local Structure of Turbulence in Incompressible Viscous Fluid for Very Large Reynolds' Numbers. *Akademiia Nauk SSSR Doklady*, 30:301–305, 1941.

K. Kratter and G. Lodato. Gravitational Instabilities in Circumstellar Disks. ARA&A, 54:271–311, September 2016. doi: 10.1146/annurev-astro-081915-023307.

S. Krijt and F. J. Ciesla. Dust Diffusion and Settling in the Presence of Collisions: Trapping (sub)micron Grains in the Midplane. ApJ, 822:111, May 2016. doi: 10.3847/0004-637X/822/2/111.

S. Krijt, F. J. Ciesla, and E. A. Bergin. Tracing Water Vapor and Ice During Dust Growth. ApJ, 833:285, December 2016. doi: 10.3847/1538-4357/833/2/285.

W. Kwon, L. W. Looney, and L. G. Mundy. Resolving the Circumstellar Disk of HL Tauri at Millimeter Wavelengths. ApJ, 741:3, November 2011. doi: 10.1088/0004-637X/741/1/3.

R. Landry, S. E. Dodson-Robinson, N. J. Turner, and G. Abram. Protostellar Disk Evolution over Million-year Timescales with a Prescription for Magnetized Turbulence. ApJ, 771:80, July 2013. doi: 10.1088/0004-637X/771/2/80.

D. N. C. Lin and J. Papaloizou. Tidal torques on accretion discs in binary systems with extreme mass ratios. MNRAS, 186:799–812, March 1979. doi: 10.1093/mnras/186.4.799.

D. N. C. Lin and J. Papaloizou. On the tidal interaction between protoplanets and the protoplanetary disk. III - Orbital migration of protoplanets. ApJ, 309:846–857, October 1986. doi: 10.1086/164653.

D. N. C. Lin and J. C. B. Papaloizou. On the tidal interaction between protostellar disks and companions. In E. H. Levy and J. I. Lunine, editors, *Protostars and Planets III*, pages 749–835, 1993.

M.-K. Lin and K. M. Kratter. On the Gravitational Stability of Gravito-turbulent Accretion Disks. ApJ, 824:91, June 2016. doi: 10.3847/0004-637X/824/2/91.

J. J. Lissauer and G. R. Stewart. Planetary accretion in circumstellar disks. In J. A. Phillips, S. E. Thorsett, and S. R. Kulkarni, editors, *Planets Around Pulsars*, volume 36 of *Astronomical Society of the Pacific Conference Series*, pages 217–233, January 1993.

J. J. Lissauer, O. Hubickyj, G. D'Angelo, and P. Bodenheimer. Models of Jupiter's growth incorporating thermal and hydrodynamic constraints. Icarus, 199:338–350, February 2009. doi: 10.1016/j.icarus.2008.10.004.

R. V. E. Lovelace, H. Li, S. A. Colgate, and A. F. Nelson. Rossby Wave Instability of Keplerian Accretion Disks. ApJ, 513:805–810, March 1999. doi: 10.1086/306900.

D. Lynden-Bell and J. E. Pringle. The evolution of viscous discs and the origin of the nebular variables. MNRAS, 168:603–637, September 1974. doi: 10.1093/mnras/168.3.603.

W. Lyra. Convective Overstability in Accretion Disks: Three-dimensional Linear Analysis and Nonlinear Saturation. ApJ, 789:77, July 2014. doi: 10.1088/0004-637X/789/1/77.

P. S. Marcus, S. Pei, C.-H. Jiang, J. A. Barranco, P. Hassanzadeh, and D. Lecoanet. Zombie Vortex Instability. I. A Purely Hydrodynamic Instability to Resurrect the Dead Zones of Protoplanetary Disks. ApJ, 808:87, July 2015. doi: 10.1088/0004-637X/808/1/87.

F. Masset. FARGO: A fast eulerian transport algorithm for differentially rotating disks. A&AS, 141:165–173, January 2000. doi: 10.1051/aas:2000116.

J. S. Mathis, W. Rumpl, and K. H. Nordsieck. The size distribution of interstellar grains. ApJ, 217:425–433, October 1977. doi: 10.1086/155591.

L. Mayer, B. Moore, T. Quinn, F. Governato, and J. Stadel. Tidal debris of dwarf spheroidals as a probe of structure formation models. MNRAS, 336:119–130, October 2002. doi: 10.1046/j.1365-8711.2002.05721.x.

M. Mayor and D. Queloz. A Jupiter-mass companion to a solar-type star. Nature, 378:355–359, November 1995. doi: 10.1038/378355a0.

M. K. McClure, E. A. Bergin, L. I. Cleeves, E. F. van Dishoeck, G. A. Blake, N. J. Evans, II, J. D. Green, T. Henning, K. I. Öberg, K. M. Pontoppidan, and C. Salyk. Mass Measurements in Protoplanetary Disks from Hydrogen Deuteride. ApJ, 831:167, November 2016. doi: 10.3847/0004-637X/831/2/167.

F. Meru and M. R. Bate. Exploring the conditions required to form giant planets via gravitational instability in massive protoplanetary discs. MNRAS, 406:2279–2288, August 2010. doi: 10.1111/j.1365-2966.2010.16867.x.

N. Meyer-Vernet and B. Sicardy. On the physics of resonant disk-satellite interaction. Icarus, 69:157–175, January 1987. doi: 10.1016/0019-1035(87)90011-X.

M. Min, C. P. Dullemond, M. Kama, and C. Dominik. The thermal structure and the location of the snow line in the protosolar nebula: Axisymmetric models with full 3-D radiative transfer. Icarus, 212:416–426, March 2011. doi: 10.1016/j.icarus.2010.12.002.

A. Miotello, L. Testi, G. Lodato, L. Ricci, G. Rosotti, K. Brooks, A. Maury, and A. Natta. Grain growth in the envelopes and disks of Class I protostars. A&A, 567:A32, July 2014. doi: 10.1051/0004-6361/201322945.

A. Miotello, E. F. van Dishoeck, J. P. Williams, M. Ansdell, G. Guidi, M. Hogerheijde, C. F. Manara, M. Tazzari, L. Testi, N. van der Marel, and S. van Terwisga. Lupus disks with faint CO isotopologues: low gas/dust or high carbon depletion? A&A, 599:A113, March 2017. doi: 10.1051/0004-6361/201629556.

A. Morbidelli, J. I. Lunine, D. P. O'Brien, S. N. Raymond, and K. J. Walsh. Building Terrestrial Planets. *Annual Review of Earth and Planetary Sciences*, 40:251–275, May 2012. doi: 10.1146/annurev-earth-042711-105319.

G. D. Mulders and C. Dominik. Probing the turbulent mixing strength in protoplanetary disks across the stellar mass range: no significant variations. A&A, 539:A9, March 2012. doi: 10.1051/0004-6361/201118127.

Y. Nakagawa, K. Nakazawa, and C. Hayashi. Growth and sedimentation of dust grains in the primordial solar nebula. Icarus, 45:517–528, March 1981. doi: 10.1016/0019-1035(81)90018-X.

R. P. Nelson. Collapse and fragmentation of rotating, prolate clouds. MNRAS, 298: 657–676, August 1998. doi: 10.1046/j.1365-8711.1998.01533.x.

R. P. Nelson, J. C. B. Papaloizou, F. Masset, and W. Kley. The migration and growth of protoplanets in protostellar discs. MNRAS, 318:18–36, October 2000. doi: 10.1046/j.1365-8711.2000.03605.x.

R. P. Nelson, O. Gressel, and O. M. Umurhan. Linear and non-linear evolution of the vertical shear instability in accretion discs. MNRAS, 435:2610–2632, November 2013. doi: 10.1093/mnras/stt1475.

K. Ohtsuki, Y. Nakagawa, and K. Nakazawa. Artificial acceleration in accumulation due to coarse mass-coordinate divisions in numerical simulation. Icarus, 83:205–215, January 1990. doi: 10.1016/0019-1035(90)90015-2.

S. Okuzumi and S. Hirose. Planetesimal Formation in Magnetorotationally Dead Zones: Critical Dependence on the Net Vertical Magnetic Flux. ApJ, 753:L8, July 2012. doi: 10.1088/2041-8205/753/1/L8.

C. W. Ormel and J. N. Cuzzi. Closed-form expressions for particle relative velocities induced by turbulence. A&A, 466:413–420, May 2007. doi: 10.1051/0004-6361:20066899.

C. W. Ormel and M. Spaans. Monte Carlo Simulation of Particle Interactions at High Dynamic Range: Advancing beyond the Googol. ApJ, 684:1291–1309, September 2008. doi: 10.1086/590052.

C. W. Ormel, M. Spaans, and A. G. G. M. Tielens. Dust coagulation in protoplanetary disks: porosity matters. A&A, 461:215–232, January 2007. doi: 10.1051/0004-6361:20065949.

J. C. Papaloizou and G. J. Savonije. Instabilities in self-gravitating gaseous discs. MNRAS, 248:353–369, February 1991. doi: 10.1093/mnras/248.3.353.

I. Pascucci, L. Testi, G. J. Herczeg, F. Long, C. F. Manara, N. Hendler, G. D. Mulders, S. Krijt, F. Ciesla, T. Henning, S. Mohanty, E. Drabek-Maunder, D. Apai, L. Szűcs, G. Sacco, and J. Olofsson. A Steeper than Linear Disk Mass-Stellar Mass Scaling Relation. ApJ, 831:125, November 2016. doi: 10.3847/0004-637X/831/2/125.

L. M. Pérez, J. M. Carpenter, C. J. Chandler, A. Isella, S. M. Andrews, L. Ricci, N. Calvet, S. A. Corder, A. T. Deller, C. P. Dullemond, J. S. Greaves, R. J. Harris, T. Henning, W. Kwon, J. Lazio, H. Linz, L. G. Mundy, A. I. Sargent, S. Storm, L. Testi, and D. J. Wilner. Constraints on the Radial Variation of Grain Growth in the AS 209 Circumstellar Disk. ApJ, 760:L17, November 2012. doi: 10.1088/2041-8205/760/1/L17.

L. M. Pérez, C. J. Chandler, A. Isella, J. M. Carpenter, S. M. Andrews, N. Calvet, S. A. Corder, A. T. Deller, C. P. Dullemond, J. S. Greaves, R. J. Harris, T. Henning, W. Kwon, J. Lazio, H. Linz, L. G. Mundy, L. Ricci, A. I. Sargent, S. Storm, M. Tazzari, L. Testi, and D. J. Wilner. Grain Growth in the Circumstellar Disks of the Young Stars CY Tau and DoAr 25. ApJ, 813:41, November 2015. doi: 10.1088/0004-637X/813/1/41.

L. M. Pérez, J. M. Carpenter, S. M. Andrews, L. Ricci, A. Isella, H. Linz, A. I. Sargent, D. J. Wilner, T. Henning, A. T. Deller, C. J. Chandler, C. P. Dullemond, J. Lazio, K. M. Menten, S. A. Corder, S. Storm, L. Testi, M. Tazzari, W. Kwon, N. Calvet, J. S. Greaves, R. J. Harris, and L. G. Mundy. Spiral density waves in a young protoplanetary disk. *Science*, 353:1519–1521, September 2016. doi: 10.1126/science.aaf8296.

B. K. Pickett, A. C. Mejía, R. H. Durisen, P. M. Cassen, D. K. Berry, and R. P. Link. The Thermal Regulation of Gravitational Instabilities in Protoplanetary Disks. ApJ, 590:1060–1080, June 2003. doi: 10.1086/375147.

M. Podolak, L. Mayer, and T. Quinn. Evolution of Coated Grains in Spiral Shocks of Self-gravitating Protoplanetary Disks. ApJ, 734:56, June 2011. doi: 10.1088/0004-637X/734/1/56.

J. B. Pollack, O. Hubickyj, P. Bodenheimer, J. J. Lissauer, M. Podolak, and Y. Greenzweig. Formation of the Giant Planets by Concurrent Accretion of Solids and Gas. Icarus, 124:62–85, November 1996. doi: 10.1006/icar.1996.0190.

J. E. Pringle. Accretion discs in astrophysics. ARA&A, 19:137–162, 1981. doi: 10.1146/annurev.aa.19.090181.001033.

S. N. Raymond and C. Cossou. No universal minimum-mass extrasolar nebula: evidence against in situ accretion of systems of hot super-Earths. MNRAS, 440:L11–L15, May 2014. doi: 10.1093/mnrasl/slu011.

L. Ricci, L. Testi, A. Natta, R. Neri, S. Cabrit, and G. J. Herczeg. Dust properties of protoplanetary disks in the Taurus-Auriga star forming region from millimeter wavelengths. A&A, 512:A15, March 2010. doi: 10.1051/0004-6361/200913403.

T. Sano and S. M. Miyama. Magnetorotational Instability in Protoplanetary Disks. I. On the Global Stability of Weakly Ionized Disks with Ohmic Dissipation. ApJ, 515:776–786, April 1999. doi: 10.1086/307063.

R. Schräpler and T. Henning. Dust Diffusion, Sedimentation, and Gravitational Instabilities in Protoplanetary Disks. ApJ, 614:960–978, October 2004. doi: 10.1086/423831.

N. I. Shakura and R. A. Sunyaev. Black holes in binary systems. Observational appearance. A&A, 24:337–355, 1973.

J.-M. Shi and E. Chiang. Gravito-turbulent Disks in Three Dimensions: Turbulent Velocities versus Depth. ApJ, 789:34, July 2014. doi: 10.1088/0004-637X/789/1/34.

Y. Shimaki and M. Arakawa. Low-velocity collisions between centimeter-sized snowballs: Porosity dependence of coefficient of restitution for ice aggregates analogues in the Solar System. Icarus, 221:310–319, September 2012. doi: 10.1016/j.icarus.2012.08.005.

J. B. Simon, X.-N. Bai, K. M. Flaherty, and A. M. Hughes. Origin of Weak Turbulence in the Outer Regions of Protoplanetary Disks. ApJ, 865:10, September 2018. doi: 10.3847/1538-4357/aad86d.

D. Stamatellos and A. P. Whitworth. Can giant planets form by gravitational fragmentation of discs?. A&A, 480:879–887, March 2008. doi: 10.1051/0004-6361:20078628.

D. Stamatellos and A. P. Whitworth. The role of thermodynamics in disc fragmentation. MNRAS, 400:1563–1573, December 2009. doi: 10.1111/j.1365-2966.2009.15564.x.

J. Steinacker, L. Pagani, A. Bacmann, and S. Guieu. Direct evidence of dust growth in L183 from mid-infrared light scattering. A&A, 511:A9, February 2010. doi: 10.1051/0004-6361/200912835.

J. Steinacker, M. Andersen, W.-F. Thi, R. Paladini, M. Juvela, A. Bacmann, V.-M. Pelkonen, L. Pagani, C. Lefèvre, T. Henning, and A. Noriega-Crespo. Grain size limits derived from 3.6 μm and 4.5 μm coreshine. A&A, 582:A70, October 2015. doi: 10.1051/0004-6361/201425434.

M. H. R. Stoll and W. Kley. Vertical shear instability in accretion disc models with radiation transport. A&A, 572:A77, December 2014. doi: 10.1051/0004-6361/201424114.

G. Suttner and H. W. Yorke. Early Dust Evolution in Protostellar Accretion Disks. ApJ, 551:461–477, April 2001. doi: 10.1086/320061.

T. Takeuchi and D. N. C. Lin. Radial Flow of Dust Particles in Accretion Disks. ApJ, 581:1344–1355, December 2002. doi: 10.1086/344437.

H. Tanaka, T. Takeuchi, and W. R. Ward. Three-Dimensional Interaction between a Planet and an Isothermal Gaseous Disk. I. Corotation and Lindblad Torques and Planet Migration. ApJ, 565:1257–1274, February 2002. doi: 10.1086/324713.

M. Tazzari, L. Testi, B. Ercolano, A. Natta, A. Isella, C. J. Chandler, L. M. Pérez, S. Andrews, D. J. Wilner, L. Ricci, T. Henning, H. Linz, W. Kwon, S. A. Corder, C. P. Dullemond, J. M. Carpenter, A. I. Sargent, L. Mundy, S. Storm, N. Calvet, J. A. Greaves, J. Lazio, and A. T. Deller. Multiwavelength analysis for interferometric (sub-)mm observations of protoplanetary disks. Radial constraints on the dust properties and the disk structure. A&A, 588:A53, April 2016. doi: 10.1051/0004-6361/201527423.

C. Terquem and J. C. B. Papaloizou. Dynamical relaxation and the orbits of low-mass extrasolar planets. MNRAS, 332:L39–L43, May 2002. doi: 10.1046/j.1365-8711.2002.05493.x.

J. J. Tobin, K. M. Kratter, M. V. Persson, L. W. Looney, M. M. Dunham, D. Segura-Cox, Z.-Y. Li, C. J. Chandler, S. I. Sadavoy, R. J. Harris, C. Melis, and L. M. Pérez. A triple protostar system formed via fragmentation of a gravitationally unstable disk. Nature, 538:483–486, October 2016. doi: 10.1038/nature20094.

A. Toomre. On the gravitational stability of a disk of stars. ApJ, 139:1217–1238, May 1964. doi: 10.1086/147861.

Y. Tsukamoto, S. Okuzumi, and A. Kataoka. Apparent Disk-mass Reduction and Planetisimal Formation in Gravitationally Unstable Disks in Class 0/I Young Stellar Objects. ApJ, 838:151, April 2017. doi: 10.3847/1538-4357/aa6081.

N. J. Turner and T. Sano. Dead Zone Accretion Flows in Protostellar Disks. ApJ, 679:L131, June 2008. doi: 10.1086/589540.

N. J. Turner, T. Sano, and N. Dziourkevitch. Turbulent Mixing and the Dead Zone in Protostellar Disks. ApJ, 659:729–737, April 2007. doi: 10.1086/512007.

N. J. Turner, S. Fromang, C. Gammie, H. Klahr, G. Lesur, M. Wardle, and X.-N. Bai. Transport and Accretion in Planet-Forming Disks. *Protostars and Planets VI*, pages 411–432, 2014. doi: 10.2458/azu_uapress_9780816531240-ch018.

W. R. Ward. Protoplanet Migration by Nebula Tides. Icarus, 126:261–281, April 1997. doi: 10.1006/icar.1996.5647.

M. Wardle. Magnetic fields in protoplanetary disks. Ap&SS, 311:35–45, October 2007. doi: 10.1007/s10509-007-9575-8.

S. J. Weidenschilling. Evolution of grains in a turbulent solar nebula. Icarus, 60:553–567, December 1984. doi: 10.1016/0019-1035(84)90164-7.

F. Windmark, T. Birnstiel, C. Güttler, J. Blum, C. P. Dullemond, and T. Henning. Planetesimal formation by sweep-up: how the bouncing barrier can be beneficial to growth. A&A, 540:A73, April 2012a. doi: 10.1051/0004-6361/201118475.

F. Windmark, T. Birnstiel, C. W. Ormel, and C. P. Dullemond. Breaking through: the effects of a velocity distribution on barriers to dust growth (Corrigendum). A&A, 548:C1, December 2012b. doi: 10.1051/0004-6361/201220004e.

Le Yang and Fred J. Ciesla. The effects of disk building on the distributions of refractory materials in the solar nebula. *Meteoritics and Planetary Science*, 47:99–119, January 2012. doi: 10.1111/j.1945-5100.2011.01315.x.

M. Yasui, R. Hayama, and M. Arakawa. Impact strength of small icy bodies that experienced multiple collisions. Icarus, 233:293–305, May 2014. doi: 10.1016/j.icarus.2014.02.008.

M. Yu, K. Willacy, S. E. Dodson-Robinson, N. J. Turner, and N. J. Evans, II. Probing Planet Forming Zones with Rare CO Isotopologues. ApJ, 822:53, May 2016. doi: 10.3847/0004-637X/822/1/53.

M. Yu, N. J. Evans, II, S. E. Dodson-Robinson, K. Willacy, and N. J. Turner. Disk Masses around Solar-mass Stars are Underestimated by CO Observations. ApJ, 841: 39, May 2017. doi: 10.3847/1538-4357/aa6e4c.

A. Zsom and C. P. Dullemond. A representative particle approach to coagulation and fragmentation of dust aggregates and fluid droplets. A&A, 489:931–941, October 2008. doi: 10.1051/0004-6361:200809921.

Appendix A

1D DIFFUSION EQUATION FROM NAVIER-STOKES

In this appendix, we present the full derivation of equations 2.7 and 2.8 starting from the classic Navier Stokes equation. We have already seen the modified form of mass and angular momentum conservation equation for a viscous accretion disk. Starting from equations 2.21 and 2.31, we now eliminate $\bar{v_r}$. From equation 2.31, $\bar{v_r}$ can be written as

$$\bar{v_r} = \frac{1}{r\Sigma}\left(\frac{dr}{dh}\right)\frac{\partial}{\partial r}\left(\bar{\nu}\Sigma r^3\frac{d\Omega}{dr}\right) \tag{A.1}$$

Now, using the mass conservation equation, equation 2.21, substituting $\bar{v_r}$, we get

$$\frac{\partial\Sigma}{\partial t} + \frac{1}{r}\frac{\partial}{\partial r}\left[r\Sigma\frac{1}{r\Sigma}\left(\frac{dr}{dh}\right)\frac{\partial}{\partial r}\left(\bar{\nu}\Sigma r^3\frac{d\Omega}{dr}\right)\right] = 0. \tag{A.2}$$

$$\implies \frac{\partial\Sigma}{\partial t} + \frac{1}{r}\frac{\partial}{\partial r}\left[\left(\frac{dr}{dh}\right)\frac{\partial}{\partial r}\left(\bar{\nu}\Sigma r^3\frac{d\Omega}{dr}\right)\right] = 0. \tag{A.3}$$

Now, the specific angular momentum h can be written as

$$h = r\Omega = \sqrt{GM_\star r} \tag{A.4}$$

$$\implies \frac{dh}{dr} = \frac{1}{2}\sqrt{\frac{GM_\star}{r}} \tag{A.5}$$

Also, $d\Omega/\,dr = -(3/2)\sqrt{GM_\star/r^5}$. Using these in equation A.3, we get

$$\frac{\partial\Sigma}{\partial t} = \frac{3}{r}\frac{\partial}{\partial r}\left[r^{1/2}\frac{\partial}{\partial r}\left(\bar{\nu}\Sigma r^{1/2}\right)\right] \tag{A.6}$$

which is the desired diffusion equation for a viscous accretion disk.

Appendix B

DERIVATION OF RADIAL DRIFT VELOCITY

To derive the radial drift velocity of dust particles due to gas drag, we can start from equation 2.40. Equation 2.40 can be re-written as

$$v_{\phi,g} = v_K \left(1 - \eta\right)^{1/2} \tag{B.1}$$

where

$$\eta = n\frac{c_s^2}{v_K^2}. \tag{B.2}$$

Here we use v_r and v_ϕ as the radial and azimuthal velocity of dust particles and $v_{r,g}$ and $v_{\phi,g}$ as the same for gas molecules. Including the drag force on dust from the gas, the radial and azimuthal equations of motion for dust grains can be written as

$$\frac{dv_r}{dt} = \frac{v_\phi^2}{R} - \Omega^2 R - \frac{1}{t_f}\left(v_r - v_{r,g}\right) \tag{B.3}$$

and

$$\frac{d}{dt}\left(Rv_\phi\right) = -\frac{R}{t_f}\left(v_\phi - v_{\phi,g}\right). \tag{B.4}$$

In equations B.3 and B.4, the last terms are a drag term or a mechanical relaxation term which basically states that the gas velocity components are relaxed to gas velocities in a friction time scale t_f (See section 2.3.1). Now, the LHS of equation B.4 can be stated as

$$\frac{d}{dt}\left(Rv_\phi\right) = \frac{d}{dR}\left(Rv_\phi\right)\frac{dR}{dt} = \frac{1}{2}v_R v_K \tag{B.5}$$

where we have used $dR/\,dt = v_R$. Substituting this in equation B.4, we get

$$v_\phi - v_{\phi,g} \approx -\frac{v_R v_K t_f}{2R}. \tag{B.6}$$

The radial equation can be re-written as

$$\frac{dv_R}{dt} = -\frac{\eta v_k^2}{R} + \frac{2v_k}{R}\left(v_\phi - v_{\phi,g}\right) - \frac{1}{t_f}\left(v_r - v_{r,g}\right) \tag{B.7}$$

where we have substituted Ω from equation B.2 in equation B.3 as below:

$$v_{\phi,g}^2 = v_k^2 - \eta v_k^2 \tag{B.8}$$

$$\implies v_k^2 = v_{\phi,g}^2 + \eta v_k^2 \tag{B.9}$$

Substituting v_K^2 in equation B.3 and using $v_\phi \approx v_{\phi,g} \approx v_k$, we can arrive at equation B.7. Eliminating $v_\phi - v_{\phi,g}$ from equation B.6 and B.7, we get

$$v_r = v_K \frac{-\eta}{\frac{v_k t_f}{R} + \frac{R}{v_K t_f}}. \tag{B.10}$$

Using $St = t_f \Omega$, equation B.10 becomes,

$$v_r = -\frac{\eta v_K}{St + \frac{1}{St}} \tag{B.11}$$

Appendix C

GROWTH AND SETTLING TIMESCALES

In the existing dust models which are vertically global, a vertically averaged steady state is assumed. This might be a good approximation for the inner radii, but can fail in regions where the growth timescale is comparable to the settling timescale. Below, we make estimates of the two timescales.

The growth timescale for dust particles (t_g) can be cast as

$$t_g \sim \left| \frac{d \ln m}{dt} \right|^{-1} = \frac{m}{\dot{m}} \tag{C.1}$$

with

$$\dot{m} = \frac{dm}{dt} \sim \frac{\Delta m}{\Delta t} \sim \frac{m}{1/n\sigma v}. \tag{C.2}$$

Hence, the growth timescale can be written as:

$$t_g \sim \frac{m}{\rho_d \sigma v} = \frac{4}{3\eta} \frac{a\rho_m}{\sqrt{\alpha}\rho_g c_s}, \tag{C.3}$$

where η is the abundance ratio and $v \sim \sqrt{\alpha} c_s$ is the collision velocity in the intermediate turbulent regime.

The settling time scale, on the other hand, can be written as:

$$t_s = \left| \frac{d \ln z}{dt} \right|^{-1} \sim \frac{z}{v_z} \tag{C.4}$$

Using equation 2.53,

$$t_s \sim \frac{c_s}{a} \frac{\rho_g}{\rho_m} \Omega^{-2} \tag{C.5}$$

Comparing the two timescales, we have:

$$\frac{t_g}{t_s} \sim \frac{4}{3\eta}\frac{a^2\rho_m^2}{\sqrt{\alpha}\rho_g^2 h_g^2}$$
$$\sim \frac{4}{3\eta}\frac{a^2\rho_m^2}{\sqrt{\alpha}h_g^2\rho_0^2}e^{z^2/h_g^2} \tag{C.6}$$

Equation C.6 clearly shows that as we move towards the disk surface the gas density, and hence, dust number density decreases making it longer for dust particles to grow. The vertical component of gravity on the other hand is roughly propostional to height z, in a first order approximation, leading to a faster settling. Setting equation C.6 ~ 1 ($t_g = t_s$),

$$\frac{z}{h_g} \sim \left[\ln\left(\frac{3\eta}{8\pi}\frac{\sqrt{\alpha}\Sigma_g^2}{a^2\rho_m^2}\right)\right]^{1/2} \tag{C.7}$$

where we have used $\rho_0 = \Sigma_g/\sqrt{2\pi}h_g$. A simple estimate for an MMSN disk at 1 au with $\alpha = 10^{-4}$, $a = 1$ mm and $\rho_m = 1$ g cm^{-3} gives $z/h_g \sim 3$. Therefore, for disk models extending upto $4-5$ scale-heights in the vertical direction, the steady state will be influenced by the settling of dust particles. In the outer region of the disk, this effect is more stringent at a lower distance from the mid-plane

Appendix D

GENERATING RANDOM NUMBER FROM MAXWELL-BOLTZMANN DISTRIBUTION

A substantial part of our computation time is spent in drawing random numbers from different distributions, such as normal or Maxwell-Boltzmann. In our code, we use a single random number generator which can generates random numbers from a uniform distribution between 0 and 1. To generate random numbers from a normal distribution, we use the Box-Muller Transform. If r_1 and r_2 are two random numbers generated from the uniform distribution, then

$$n_1 = \sqrt{-2 \ln r_1} \cos(2\pi r_2), \tag{D.1}$$

$$n_2 = \sqrt{-2 \ln r_2} \sin(2\pi r_1) \tag{D.2}$$

will be two independent random numbers from standard normal distribution. In this case, if r_1 and r_2 are the two arrays of size N, n_1 and n_2 will produce two arrays of independent random numbers of size N.

Generating the random number from Maxwell-Boltzmann distribution can be done by either an acceptance-rejection method of by using a cumulative distribution function.However, we exploit the fact that when a Gaussian integral of type

$$F_{Gaussian} \sim exp\left(-\frac{v^2}{2\sigma^2}\right) \tag{D.3}$$

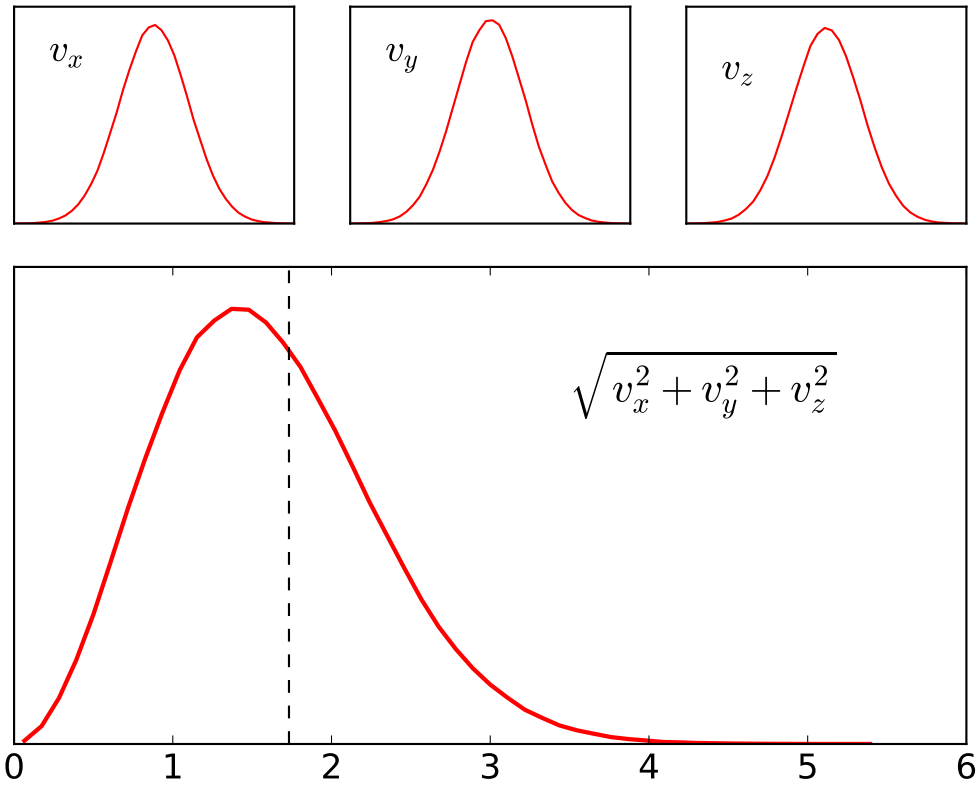

Figure D.1: A depiction of the process of random number generation from the Maxwell-Boltzmann (MB) distribution. The top panels show the three sets of random numbers from a normal distribution with mean $\mu = 0$ and standard deviation $\sigma = 1$. These are identified as the three components of the particle velocities. The lower panel shows the MB distribution generated. The black dashed vertical line corresponds to the rms value of the MB distribution which is $\sqrt{3}$ in this case.

is integrated over the surface of the sphere, we get a Maxwell-Boltzmann of the form

$$F_{MB} \sim v^2 exp\left(-\frac{v^2}{2\sigma^2}\right). \tag{D.4}$$

Physically, the individual velocity components of a particle follow a normal distribution, whereas, the scalar velocity of the particles in a box follows the Maxwell-Boltzmann distribution. So, to generate random numbers from MB distribution, we first generate three independent random number from standard normal distribution and take the square root of the sum of their squares. In figure D.1 we have shown this process where the three plots in the top panel are three sets of random numbers with mean $\mu = 0$ and standard deviation $\sigma = 1$. The plot in the lower panel shows the MB distribution generated with an rms value of $\sqrt{3}$ (the dashed vertical black line).

Appendix E

VARIABLE TURBULENCE PROFILE

The calculation of an α profile that varies vertically according to the dust distribution and dust abundance is motivated from the method adopted by [Landry et al., 2013] which is based on model 4 of Ilgner and Nelson [2006]. As the main source of turbulence in our disk is magnetorotational instability (MRI), we first describe the MRI activity criteria, followed by the model for ionization-recombination chemistry which is used to calculate the electron and ion abundances that control the level of coupling between the gas and the magnetic fields.

The MHD induction equation, with all the non-ideal terms can be written as

$$\frac{\partial B}{\partial t} = \nabla \times (\boldsymbol{v} \times \boldsymbol{B}) - \nabla \times \left[\eta_O \nabla \times \boldsymbol{B} + \eta_H \left(\nabla \times \boldsymbol{B}\right) \times \hat{\boldsymbol{B}} + \eta_A \left(\nabla \times \boldsymbol{B}\right)_\perp\right]. \quad \text{(E.1)}$$

Here, $\boldsymbol{v}$ is the gas velocity and $\boldsymbol{B}$ is the magnetic field, with $\hat{B}$ the unit vector pointing in the direction of the magnetic field. η_O, η_H and η_A are the Ohmic, Hall and Ambipolar diffusivities respectively. The non-ideal terms, in the square bracket, arise from collisional effects of ions with the neutrals, which are mostly molecular hydrogen and dust grains in our case.

The dominance of the Ohmic term can be determined from the Elsasser number, defined as

$$\Lambda = \frac{v_{Az}^2}{\eta_O \Omega} \quad \text{(E.2)}$$

where, v_{Az} is the z-component of the Alfvén speed. When Λ reaches unity, the Ohmic term in equation E.1 dominates. According to Sano and Miyama [1999], the most

unstable MRI mode in this case can be given as

$$\lambda_{local} \approx \max\{\lambda_{ideal}, \lambda_{res}\} \tag{E.3}$$

where

$$\lambda_{ideal} = 2\pi \frac{v_{Az}}{\Omega} \tag{E.4}$$

and

$$\lambda_{res} = 2\pi \frac{\eta_O}{v_{Az}}. \tag{E.5}$$

So, physically, Λ is the ratio of the largest unstable wavelength to the diffusive length scale. Turner and Sano [2008] showed that the magnetic pressure of the toroidal component of the magnetic fields in MRI turbulence is 10 to 30 times greater than that of the vertical component. Hence, the vertical component of Alfvén speed can be written as

$$v_{Az}^2 = \frac{1}{10} v_A^2 \tag{E.6}$$

with $V_A = B/\sqrt{4\pi\rho}$. Thus, $\Lambda \gtrsim 1$ criteria ensures that the most unstable wavelength can grow in a timescale shorter that the time in which charged particles can diffuse across the magnetic fields.

Ambipolar diffusion, the second non-ideal contribution in the square bracket in equation E.1, arises from the relative motion between charges and neutral species. In a typical protoplanetary disk, the ion density is negligible and the electron recombination time is small compared to the local orbital time $1/\Omega$ [Bai, 2011]. In such conditions, in stead of the continuity equation, the ion density is determined by the ionization-recombination equilibrium, characterized by the parameter Am [Chiang and Murray-Clay, 2007]. Am can be written as:

$$Am = \frac{\gamma \rho_i}{\Omega} \tag{E.7}$$

where, ρ_i is the ion density and γ is the ion-neutral drag coefficient, given by

$$\gamma = \frac{\langle \sigma_{ni} w_{ni} \rangle}{m_n + m_i}. \tag{E.8}$$

Here, σ_{ni} is effective cross section for ion-neutral collisions and w_{ni} is the relative velocity and $\langle \cdot\cdot \rangle$ is the temporal average.

Magnetic field strength is generally parametrized by the parameter β, a ratio of thermal pressure to magnetic pressure, and can be written as:

$$\beta = \frac{8\pi P}{|\boldsymbol{B}|^2} \tag{E.9}$$

where, P is the thermal pressure. Bai [2011] have shown that the MRI turbulence is sustained in the disk only for small value of the magnetic fields which sets a lower limit for β as a function of Am as:

$$\beta_{min}(Am) = \left[\left(\frac{50}{Am^{1.2}} \right)^2 + \left(\frac{8}{Am^{0.3}} + 1 \right)^2 \right]^{1/2}. \tag{E.10}$$

Ambipolar diffusion becomes more important as the maximum field strength increases, irrespective of field geometry. Hence, for $Am << 1$, MRI can be sustained for a sufficiently weak field. This particular non-ideal effect is a specially important at the upper atmospheres of the disk where the gas density is low and ionizations by cosmic rays and X-rays are effective.

To calculate the turbulence profile, the next step is to calculate the three non-ideal diffusivities. For a given ionized species j, the ratio of Lorentz force to the drag force can be written as:

$$\beta_i = \frac{Z_j e B}{m_j c \gamma_j \rho} \tag{E.11}$$

where, for the species j, $Z_j e$ is the charge, m_j is the mass and c is the speed of light in vacuum. Following Wardle [2007], for each diffusion regime, the conductivities can

then be calculated by summing over all charged species;

$$\sigma_O = \frac{ec}{B}\sum_j n_j Z_j \beta_j \tag{E.12}$$

$$\sigma_H = \frac{ec}{B}\sum_j \frac{n_j Z_j}{1+\beta_j^2} \tag{E.13}$$

$$\sigma_P = \frac{ec}{B}\sum_j \frac{n_j Z_j \beta_j}{1+\beta_j^2} \tag{E.14}$$

where, n_j is the number density for species j. Finally, the diffusivities can be written as,

$$\eta_O = \frac{c^2}{4\pi\sigma_O} \tag{E.15}$$

$$\eta_H = \frac{c^2}{4\pi\sigma_\perp}\frac{\sigma_H}{\sigma_\perp} \tag{E.16}$$

$$\eta_A = \frac{c^2}{4\pi\sigma_\perp}\frac{\sigma_P}{\sigma_\perp} - \eta_O \tag{E.17}$$

where, $\sigma_\perp = \sqrt{\sigma_H^2 + \sigma_P^2}$.

For computing the equilibrium abundance of species n_j, a simple chemical reaction network, based on model4 of Ilgner and Nelson [2006], has been used. The chemical network consists of the following equations:

$$\mathrm{H_2} + \mathbf{X} \rightarrow \mathrm{H_2^+} + e^- \tag{E.18}$$

$$\mathrm{H_2^+} + \mathrm{H_2} \rightarrow \mathrm{H_3^+} + \mathrm{H} \tag{E.19}$$

$$\mathrm{H_3^+} + \mathrm{CO} \rightarrow \mathrm{HCO} + \mathrm{H_2} \tag{E.20}$$

$$2\mathrm{H} + \mathrm{g} \rightarrow \mathrm{H_2} + \mathrm{g} \tag{E.21}$$

$$\mathrm{HCO^+} + e^- \rightarrow \mathrm{CO} + \mathrm{H} \tag{E.22}$$

$$\mathrm{HCO^+} + \mathrm{Mg} \rightarrow \mathrm{Mg^+} + \mathrm{CO} + \mathrm{H} \tag{E.23}$$

$$\mathrm{Mg^+} + e^- \rightarrow \mathrm{Mg} \tag{E.24}$$

In this chemical model, HCO^+ is the representative molecular ion, Mg^+ is the representative metal ion and g is the grain. X is the ionizing energetic particle, generally cosmic rays or X-rays. Also, in this network, every species is created in at least one reaction and destroyed in at least another reaction giving rise to an overall chemical balance. Thus, the reaction producing ions or electrons reduces to

$$2H_2 + 2X + 2CO \rightarrow H_2 + 2HCO^+ + 2e^- \tag{E.25}$$

Thus the underlying process can be stated as: each energetic particle (X) striking a hydrogen molecule, produces one electron and one ion. To construct our look-up table, equations E.18 to E.24 are approximated as

$$H_2 + X \rightarrow HCO^+ + e^- \tag{E.26}$$

$$HCO^+ + e^- \rightarrow H_2. \tag{E.27}$$

Since HCO abundance is orders of magnitude less than that of molecular hydrogen in a typical protoplanetary condition, forming ions leaves the H_2 abundance unchanged. Similarly, due to less abundance, CO destruction and regeneration is not modeled in this method. with these conditions, equation E.23 becomes

$$HCO^+ + Mg \rightarrow Mg^+ + H_2. \tag{E.28}$$

The chemical network thus boils down to equations E.24, E.26, E.27 and E.28 in tandem with the grain surface reaction described by Ilgner and Nelson [2006].

Appendix F

UTILITARIAN OPACITY MODEL: CUZZI ET AL. 2014

Calculating opacity of dust composition for interstellar medium or solar nebula is a long standing complex problem due to complicated structure and material properties of dust aggregates. Exoplanet birth environments are no exceptions because of observational constraints and parametric uncertainties. Several commendable efforts have been made to estimate opacity using different theories like particles in dipole approximation (ref), spherical solid grains with Mie scattering (ref) and fractals in discrete dipole approximation (ref) to name a few. Detailed calculations with all aforesaid prescriptions are computationally expensive. Cuzzi et al. [2014], on the other hand, proposes an opacity model as a combination of effective medium theory with small-particle closed-form expression with a simplified transition to the geometric optics regime.

The intensity of radiation can be quantified as:

$$I = I_0 e^{-\kappa_e \rho l} \tag{F.1}$$

where I_0 is initial incident radiation, κ_e is total opacity, ρ is volume mass density of gas and dust mixture and l is the optical path length. Extinction of a radiation beam is a function of two distinct additive mechanisms; scattering and absorption. The extinction efficiency, Q_e is thus written as a sum of absorption efficiency Q_a and scattering efficiency Q_s.

$$Q_e = Q_a + Q_s \tag{F.2}$$

Calculations of efficiencies for a particular λ is dependent on the relative size and wavelength of incident radiation. Grains absorb and emit radiation most effectively at a

wavelength comparable to their size. To capture this scenario, the opacity prescription is parametrized in terms of $x = 2\pi a/\lambda$, the geometric factor of grains with average radius a. Regions where $x << 1$ is known as the *Rayleigh regime* and the opposite case is called the *geometric optics* regime. With this setup, the opacities are calculated as:

$$\kappa_{e,\lambda} = \frac{1}{\rho_g} \int \pi r^2 n(r) Q_e(r, \lambda)\, dr \tag{F.3}$$

where, $\kappa_{e,\lambda}$ is the total extinction opacity as a function of Q_e, the extinction efficiency. At this point the model is only left with the calculation of Q_e by calculating Q_a and Q_s separately with a careful smooth transition from the Rayleigh to geometric optics regimes. In the limit of $x << 1$, Q_a and Q_s, in terms of real (n_r) and imaginary (n_i) refractive indices can be written as:

$$Q_a = \frac{24 x n_r n_i}{(n_r^2 + 2)^2} \tag{F.4}$$

$$Q_s = \frac{8x^4}{3} \frac{(n_r^2 - 1)^2}{(n_r^2 + 2)^2} \tag{F.5}$$

The expression of Q_a as in equation F.4 is applicable for the whole grain size spectrum. For scattering efficiency, Q_s, however, this is not the case and a separate expression is used for the Mie transition region as below,

$$Q_s = \frac{1}{2}(2x)^2 (n_r - 1)^2 \left(1 + \left(\frac{n_i}{n_r - 1}\right)^2\right) \tag{F.6}$$

the transition value being $x_0 = 1.3$. In addition, Cuzzi et al. [2014] takes into account the effect of the scattering phase factor g defined as below:

$$g = \langle \cos\theta \rangle = \frac{\int P(\Theta) \cos\Theta \sin\Theta\, d\Theta}{\int P(\Theta) \sin\Theta\, d\Theta} \tag{F.7}$$

For isotropic scattering, $g = 0$, which is a good approximation for particles in *Rayleigh*

regime. For larger particles, g can approach unity with a substantial amount of forward scattering.

One key simplifying feature of the C14 model is that the values of Q_e and Q_s asymptotically reach a value of 2 for lossless particles ($Q_a = 0$). However, if absorption is present, Q_s trends downward and approaches unity. This directly allows them to make the following modelling:

$$Q'_e = Q_e - gQ_s = Q_a + Q_s(1-g) \tag{F.8}$$

Also, instead of performing a full Mie calculation, C14 present a simplified choice for the value of g (equations 15 & 16 of C14);

$$for \;\; n_i < 1 : g = 0.7(x/3)^2 \;\; if \;\; x < 3, \; and \; g \approx 0.7 \;\; if \;\; x > 3 \tag{F.9}$$

$$for \;\; n_i > 1 : g \approx -0.2 \;\; if \;\; x < 3, \;\; and \;\; g \approx 0.5 \;\; if \;\; x > 3 \tag{F.10}$$

The final piece of model setting a value for growing values of Q_a and Q_s to a constant in geometric optics regime:

$$Q_a < 1 \quad and \quad Q_s(1-g) < 1 \tag{F.11}$$

With all formalisms noted above, the model finally calculates the monochromatic opacity for grains for mixed composition as:

$$\begin{aligned} \kappa_{e,\lambda} &= \frac{1}{\rho_g} \sum_j \beta_j \int n(r) \pi r^2 Q'_{e,j}(r,\lambda)\, dr \\ &= \frac{1}{\rho_g} \int n(r) \pi r^2 \left(\sum \beta_j Q'_{e,\lambda}(r,\lambda) \right) dr \end{aligned} \tag{F.12}$$

where β_j is the fractional number of particles of species j. In our work we find

monochromatic opacity normalized by dust density in stead of gas density to be consistent with RADMC.

The final piece of the opacity model takes care of porosity of dust aggregates. It is interesting to note that the above model circumvents the detailed Mie calculation in the transition region of relative particle size. Opacity calculated using effective medium theory usually takes an average over the size distribution. Considering porosity transfers the averaging from the wavelength domain to the dust size domain and produces a consistent result.

Appendix G

PERMISSION LETTERS

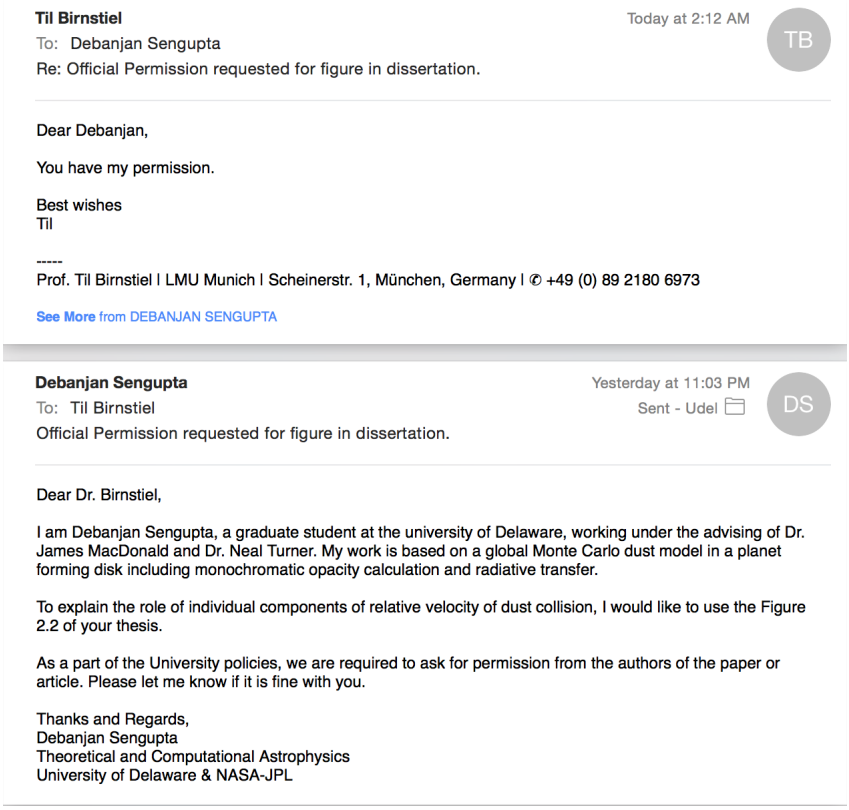

Til Birnstiel Today at 2:12 AM

To: Debanjan Sengupta

Re: Official Permission requested for figure in dissertation.

TB

Dear Debanjan,

You have my permission.

Best wishes
Til

Prof. Til Birnstiel | LMU Munich | Scheinerstr. 1, München, Germany | ✆ +49 (0) 89 2180 6973

See More from DEBANJAN SENGUPTA

Debanjan Sengupta Yesterday at 11:03 PM

To: Til Birnstiel Sent - Udel

Official Permission requested for figure in dissertation.

DS

Dear Dr. Birnstiel,

I am Debanjan Sengupta, a graduate student at the university of Delaware, working under the advising of Dr. James MacDonald and Dr. Neal Turner. My work is based on a global Monte Carlo dust model in a planet forming disk including monochromatic opacity calculation and radiative transfer.

To explain the role of individual components of relative velocity of dust collision, I would like to use the Figure 2.2 of your thesis.

As a part of the University policies, we are required to ask for permission from the authors of the paper or article. Please let me know if it is fine with you.

Thanks and Regards,
Debanjan Sengupta
Theoretical and Computational Astrophysics
University of Delaware & NASA-JPL

Figure G.1: The letter of permission from Dr. Tilman Birnstiel for Figure 2.1.

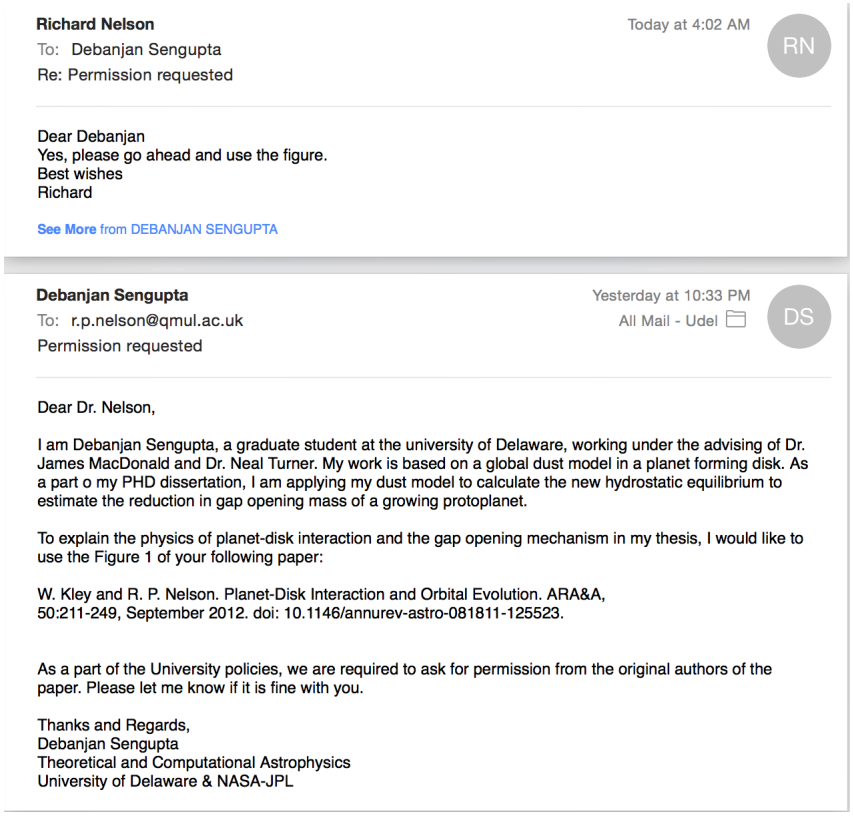

Richard Nelson Today at 4:02 AM

To: Debanjan Sengupta

Re: Permission requested

RN

Dear Debanjan
Yes, please go ahead and use the figure.
Best wishes
Richard

See More from DEBANJAN SENGUPTA

Debanjan Sengupta Yesterday at 10:33 PM

To: r.p.nelson@qmul.ac.uk

All Mail - Udel

Permission requested

DS

Dear Dr. Nelson,

I am Debanjan Sengupta, a graduate student at the university of Delaware, working under the advising of Dr. James MacDonald and Dr. Neal Turner. My work is based on a global dust model in a planet forming disk. As a part o my PHD dissertation, I am applying my dust model to calculate the new hydrostatic equilibrium to estimate the reduction in gap opening mass of a growing protoplanet.

To explain the physics of planet-disk interaction and the gap opening mechanism in my thesis, I would like to use the Figure 1 of your following paper:

W. Kley and R. P. Nelson. Planet-Disk Interaction and Orbital Evolution. ARA&A, 50:211-249, September 2012. doi: 10.1146/annurev-astro-081811-125523.

As a part of the University policies, we are required to ask for permission from the original authors of the paper. Please let me know if it is fine with you.

Thanks and Regards,
Debanjan Sengupta
Theoretical and Computational Astrophysics
University of Delaware & NASA-JPL

Figure G.2: The letter of permission from Dr. Richard Nelson for Figure 5.1.